8-2019

Optical direct detection of thermal vibrations of ultralow stiffness micro-nano structures.

Sri Sukanta Chowdhury
University of Louisville

OPTICAL DIRECT DETECTION OF THERMAL VIBRATIONS

OF ULTRALOW STIFFNESS MICRO-NANO STRUCTURES

By

Sri Sukanta Chowdhury

University of Louisville

A Dissertation

Submitted to the Faculty of the

J. B. Speed School of Engineering of the University of Louisville

In Partial fulfilment of the Requirement for the Degree of

Doctor of Philosophy in Electrical Engineering

Department of Electrical and Computer Engineering

University of Louisville

Louisville, KY 40292

August 2019

OPTICAL DIRECT DETECTION OF THERMAL VIBRATIONS

OF ULTRALOW STIFFNESS MICRO-NANO STRUCTURES

By

Sri Sukanta Chowdhury

A Dissertation Approved on

July 23, 2019

By the following Dissertation Committee

Robert W. Cohn, Ph.D. (Dissertation Advisor)

Aly A. Farag, Ph.D.

Tamer Inanc, Ph.D.

Gamini Sumanasekera, Ph.D.

DEDICATION

To my younger brother, Sree Prasanta Chowdhury, for his endless patience, love, and support.

ACKNOWLEDGEMENTS

ABSTRACT

OPTICAL DIRECT DETECTION OF THERMAL VIBRATIONS
OF ULTRALOW STIFFNESS MICRO-NANO STRUCTURES

Sri Sukanta Chowdhury

July 23, 2019

A direct detection optical vibrometer is constructed around an 850 nm laser and a quadrant photodetector (QPD). The limit of detection is 0.2 fW which corresponds to a minimum amplitude of 0.1 Å.

The vibrometer is used to measure the thermal vibration spectra of low stiffness micromechanical structures have nanometer features. One structure measured is a cantilevered 30 μm diameter glass fiber. Vibration amplitudes as low as 1.1 Å are measured. The thermal vibration spectra show fundamental resonances at 80-250 Hz and a signal to noise ratio (SNR) of 23-55 dB. Young's modulus of glass in the cantilevers, estimated from the spectra, agree to within 3 % of the manufacturer's value, which is somewhat more accurate than force-elongation measurements made of 50-100 mm long fibers which differ by 5 %.

Mass changes due to adhering small drops of liquids to the tip of the fiber cantilevers shifts the resonant frequency with a sensitivity of 120 ng. The mass detection limit would decrease by 2-3 orders by increasing the length of the time series data.

The intended purpose of the vibrometer development is the measurement of the thermal vibration of polymer bead-on-string (BOS) fibers with enough sensitivity to detect time-varying changes in the spectra that relate to molecular-level and temperature dependent changes, such as evaporation, solidification, crystallization and strain-dependent chain reorganizations of the polymer material. Time dependent variations in the BOS spectra are observed in vibrometer measurements that, if attributable to material properties, would represent 2.5-5.2 % change in elastic modulus, 20-40 % loss in water mass due to evaporation, with the minimum detectable change in these properties being 0.06 % for the measured spectra. The vibrometer provides an important tool for the real-time study of changing properties of BOS fibers, as well as other low stiffness microstructures, especially those composed of polymers and other soft mater.

TABLE OF CONTENTS

LIST OF FIGURES

xiv

LIST OF TABLES

CHAPTER 1
INTRODUCTION

Nanomechanics, a branch of nanoscience, is the study elastic, thermal and kinetic properties of physical systems at nanometer scale resolution. It can be used to measure and understand the various bulk and molecular scale properties. Every physical object mechanically vibrates at varying frequencies. The vibration amplitude might be below a limit of detection, but structures of low enough stiffness can produce detectable vibrations without no other excitation than naturally occurring white thermal noise. The vibrations are considered to be an example of Brownian motion, but a generalized description of the excitation is "thermal fluctuations" or in the case of mechanical motion, thermal vibrations. The vibration spectra of an object depends on its shape, how it is mechanically supported and its mechanical material properties (e.g. elastic modulus and loss tangent). Any changes in an object's material properties due to changes in temperature, pressure, chemistry, internal stress or molecular reorganizations, e,g, phase transformations, are reflected as changes in the vibration spectrum.

The goal of this research is to develop and demonstrate a system that is sensitive enough both to measure viscoelastic properties of nanostructures, and to detect changes in these properties over time. Of particular interest is developing a system that is sensitive enough to detect the changes as liquid polymers self-assemble into high aspect ratio

structures. The structures are referred to as bead-on-a-string (BOS) fibers which consist of a polymer material that is organized (as the result of a type of capillary-force directed self-assembly) as small diameter fibers decorated with large diameter spheres. Dimensions of the BOS structures fabricated for this study are around 50-300 nm diameter by 1 mm long for the fiber with 1-10 beads of 5-25 micron diameter. The very high aspect ratio (Sec. 2.2) of the fiber (1667-20,000) corresponds to very low bending stiffness (0.438 nN/m - 4.73 μN/m), and the large diameter of the beads, simplifies visualization and sensing of vibration of the structure.

1.1　Motivation

The viscoelastic properties of polymers are highly dependent on temperature[1], as shown in Fig. 1.1. The modulus changes by many orders of magnitude with temperature over the four regimes indicated on Fig. 1.1.
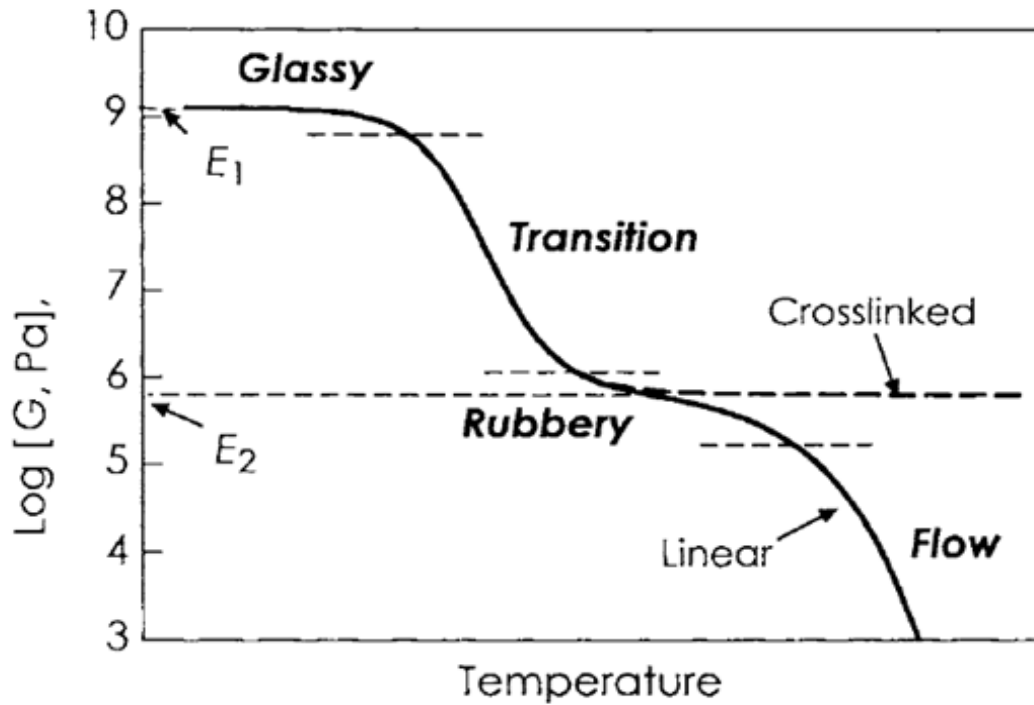
Figure 1.1. Modulus-temperature curve of polymers. Image from [1]

Below the glass transition temperature (at the knee between glassy and transition regimes—located at the intersection with the upper dashed line in Fig. 1.1), thermal fluctuation energy is much lower than the potential energy barrier required to displace a portion of any polymer chain, which corresponds to the high elastic modulus of the glassy regime. At higher temperatures where the thermal energy is comparable to the potential barrier energy, the chain segments can move and displace, corresponding to resilient leather-like characteristics of a polymer in the transition regime. The rubbery plateau is drawn for linear polymer chains. The polymer can partially recover from stretching (i.e. visco-elasticity, where it exhibits some viscous flow and some elastic recovery/memory). At higher temperatures the polymer flows as a viscous liquid. If the polymer is crosslinked (the dashed line as level E_2), the polymer never flows and the polymer (ideally) completely

3

recovers after being stretched (full elastic recovery). The rubber plateau ideally extends to infinite temperature (though in reality, the upper limit is set by the decomposition temperatures of the polymer and crosslinks). Note that the curve in Fig. 1.1 is drawn specifically for amorphous polymers. But many polymers can be partially crystallized (the degree of crystallinity depends on cooling rate and addition of impurities), and these crystallites can act as physical crosslinks that convert a polymer into an elastomer, that is identical to a rubber made by chemical crosslinking. For polymers that are not crosslinked the rubbery plateau corresponds to "temporary crosslinks" or "entanglements" between polymer chains. The entanglements provide the elastic memory for temperatures lower than the rubbery flow region. In the rubbery flow region, the time of entanglement is short enough that viscous flow dominates over elastic recovery, that is the viscoelastic material is more viscous than elastic, while in the rubbery plateau region, the material is more elastic than viscous. Longer chains (corresponding to high molecular weight polymer) take longer to disentangle than shorter chains which extend the rubbery plateau and rubbery flow region to higher temperatures. Therefore, the mechanical properties of a polymer vary to a large degree on crosslink density, percent crystallinity and molecular weight.

Both the temperature and chemical reactions that produce changes in polymers and the crosslinking, can dramatically change the material properties leading to significant changes in the vibration spectra of BOS structures. In this study we want to develop an instrument that is capable of sensing these changes. Even more dramatic changes in material properties occur as the BOS structures self-assemble from a solution that is initially mostly water and a few percent polymer. Initial BOS structure becomes evident

4

around one second, and may be difficult to track, but during later stages additional information about that material changes as the BOS fiber dries and fully solidifies would be interesting to measure and study with the proposed vibrometer.

1.2 Hypothesis, objectives, significance

The hypothesis of this study is that a "direct detection" (see Sec. 2.6.1) optical vibrometer can measure changes in vibration spectral amplitude, resonance frequency and damping of BOS structures with enough sensitivity, resolution and accuracy to be able to track vibration changes due to changes in the material properties of the polymer comprising the BOS.

The study objectives are:

1. Develop a direct detection optical vibrometer capable of measuring BOS vibration amplitudes from 1 to 50 nm.

2. Evaluate the sensitivity of the vibrometer using rather ideal microobjects, specifically cantilevered glass microfibers of similar stiffness and cross-sectional size as the bead on BOS fibers.

3. Demonstrate that the vibrometer sensitivity is sufficient to measure changes in the vibrational spectra of the BOS due to changes in material properties, e.g. temperature and drying induced changes.

The significance of the study (if successful) is the development of measurement instrumentation and techniques that can probe temperature and environmentally dependent properties of materials comprising nanomechanical structures. The results could be directly applied to better understand and control of the BOS self-assembly process, as well as understanding of how to control fabrication of other polymer structures. An additional

use of the vibrometer is in sensing changes to the vibration properties of nanomechanical structures due to external effects, such as mass loading by adsorbed chemicals. That is to say, the vibrometer used with an appropriate nanomechanical structure, has potential uses as a sensor.

CHAPTER 2
VIBRATION AND MEASUREMENTS OF NANOMECHANICAL STRUCTURES

2.1 Introduction

This chapter presents theories of vibration relevant to high aspect ratio, low-stiffness structures, e.g. the glass microfibers and BOS fibers of Chapters 5 and 6. The vibration spectra resulting from Brownian motion are of particular interest, and discussion is included on distinguishing this noise process from inherent photodetection noise. This chapter includes a review of the types and performance of various position sensors.
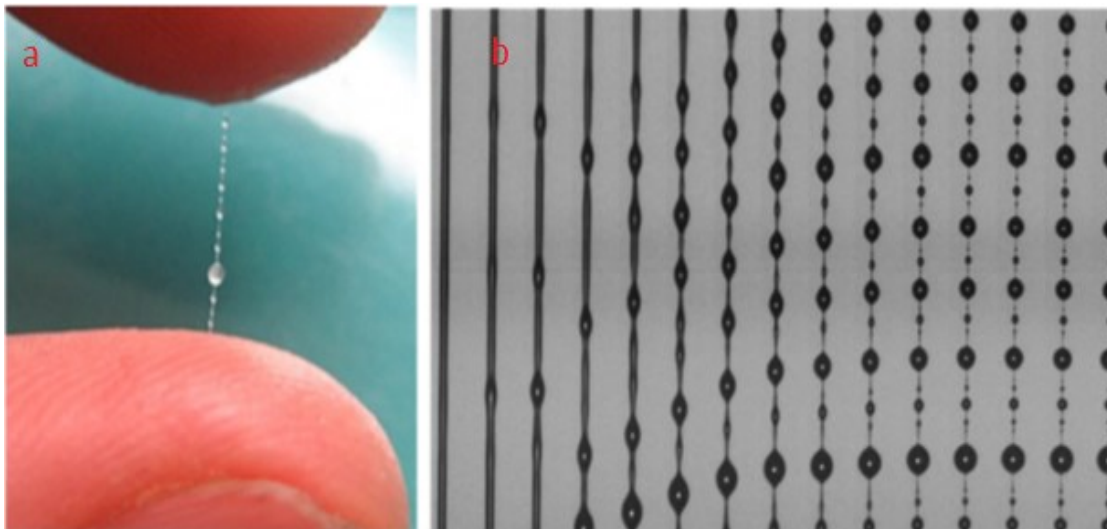
Figure 2.1. Self-assembly of BOS structures. (a) from saliva and (b) a PEO-water-glycerol solution. The sequential time-lapse image in (b) are at 25 fps. Beads of three sizes from, with each smaller set of beads forming at increasingly later times. Images from [2]

2.2 Introduction to BOS fiber

Beads on a string (BOS) fibers automatically form (i.e. self-assemble) in response to rapid stretching of a viscoelastic liquid into a thread. The structure consists of near spherical shaped beads along an otherwise very thin fiber (i.e. string). These beads can all be of the same size, or they can have multiple distinct sizes, with each set of smaller beads forming successively later times. (See Fig. 2.1 which has 3 or 4 bead sizes). The most complete model of the conditions that produce BOS structures is in Bhat *et al*.[2] which provides a phase map of the different structures formed in terms of several dimensionless parameters that describe the relative sizes of capillary, viscous, elastic and inertial forces. If the viscosity is too high, the hourglass shaped liquid bridge will not thin and transform into a fiber. If the viscosity is too low the fiber will continue to rapidly thin and ultimately break. At low viscosities polymer chain entanglement can arrest fiber breakup, resulting in a thin, near uniform diameter fiber. Or if the liquid thread is rapidly stretched longitudinally, the polymer chains can be initially stretched and entangled. Then, the chains try to relax resulting in thinning fibers in some regions and thickening into beads in other regions. Eventually the fiber thinning is arrested. Then at later stages, the polymer chains in the fiber segments can relax further, resulting in smaller beads and fibers. This repeated process is referred to as "iterated stretching." Fibers can still thin to breakup, corresponding to a transition from the rubbery plateau to the rubbery flow region of Fig. 1.1. However, because the polymers used in this study are suspended in a volatile solvent (water), the polymer fiber can dry and solidify before breaking.

2.3 Lumped element model of vibrations of structures

Distributed structures (including the BOS and the cylindrical fibers in Chs. 5.6) exhibit numerous modes of vibration that resonate at several natural frequencies. The

lowest frequency f_0 is the fundamental, and the higher frequencies are referred to as harmonics where $f_2 > f_1 > f_0$, etc. with f_1 referred to as the first harmonic. Around each resonance frequency the vibration of distributed structures is usually well modeled (for non-degenerate modes) as a second order lumped element system (Fig. 2.2) consisting of a mass (that stores kinetic or inertial energy), a spring (that stores potential energy) and a damper (that dissipates energy.) [3]
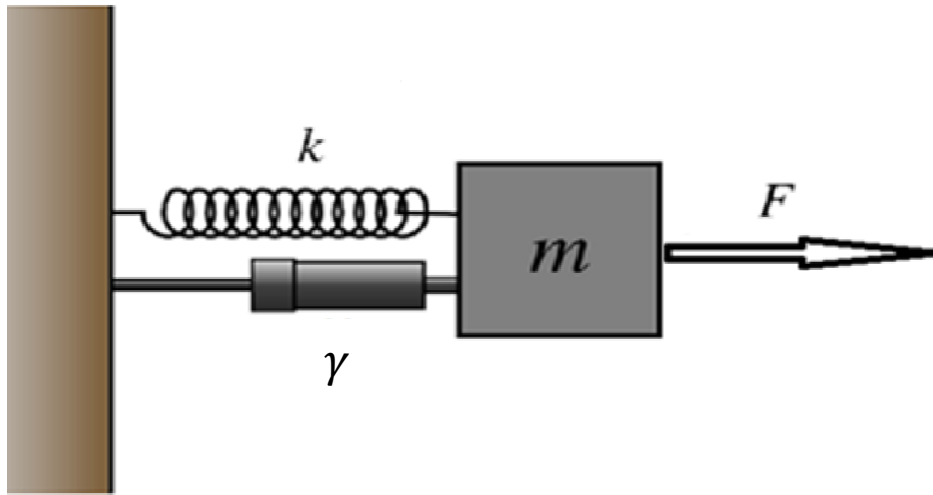
Figure 2.2 Lumped element model of a BOS fiber

The extension x of a spring to a force F is

$$F = kx \tag{2.1}$$

where k is the spring constant. The acceleration $a = \frac{d^2x}{dt^2}$ of a mass m to a force F is

$$F = ma \tag{2.2}$$

where acceleration a is the second derivative of x. The velocity $v = \frac{dx}{dt}$ of a damper to a force F is

$$F = \gamma v \tag{2.3}$$

where γ is the damping coefficient.

The combined response of the mass-spring-damper system in Fig. 2.2 to the applied force is the sum of the force (eqs. 2.1 -2.3) responses of the mechanical element gives

$$m\frac{d^2x}{dt^2} + \gamma\frac{dx}{dt} + kx = F \qquad (2.4)$$

which is a second order linear differential in x.

When the driving force F is an impulse, the solution of eq. 2.4 takes two different forms depending on if it is underdamped or overdamped. For the low damping or underdamped case, where $\gamma^2 < 4mk$, the displacement is

$$x(t) = \frac{F}{k}\left[1 - \frac{\sin(\omega t + \phi)}{\sin\phi}\exp\left(-\frac{t}{\tau}\right)\right] \qquad (2.5)$$

where

$$\tau = \frac{2m}{\gamma} \qquad (2.5a)$$

$$\omega^2 = \omega_0^2 - \frac{1}{\tau^2} \qquad (2.5b)$$

and

$$\omega_0^2 = \frac{k}{m} \qquad (2.5c)$$

where τ is the decay rate, ω_0 is the natural frequency, and ω is the frequency of oscillation. The displacement amplitude is sinusoidal with an exponentially decaying envelope that decays more rapidly with increased damping coefficient γ (see eq. 2.5a). For high damping where $\gamma^2 > 4mk$ the solution of eq. 2.4 is

$$x(t) = \frac{F}{k}\left[1 - \frac{\tau_1}{\tau_1 - \tau_2}\exp\left(-\frac{t}{\tau_1}\right) + \frac{\tau_2}{\tau_1 - \tau_2}\exp(-\frac{t}{\tau_2})\right] \qquad (2.6)$$

where

$$\tau_1 = \frac{\gamma + \sqrt{\gamma^2 - 4mk}}{2k} \qquad (2.6a)$$

10

and

$$\tau_2 = \frac{\gamma - \sqrt{\gamma^2 - 4mk}}{2k} \tag{2.6b}$$

This overdamped solution exhibits no sinusoidal ringing. Instead it is a constant plus the sum of two exponentials. One exponential decays with the long relaxation time τ_1 of the spring and damper, and a fast time constant τ_2, that corresponds to the acceleration of the mass to a velocity $\sim F/\gamma$.

Equation 2.5c gives the fundamental natural frequency but resonance can occur at other natural frequencies as well. Beam bending is well represented by a forth order partial differential equation (sec.2.4) which has several resonances which (if non-degenerate) can be represented around the resonant peak by the spectrum of lumped element model (eq. 2.4). The solution of the partial differential equation for a cantilevered beam with a uniform density cross section (Fig. 2.3) gives resonance frequencies of
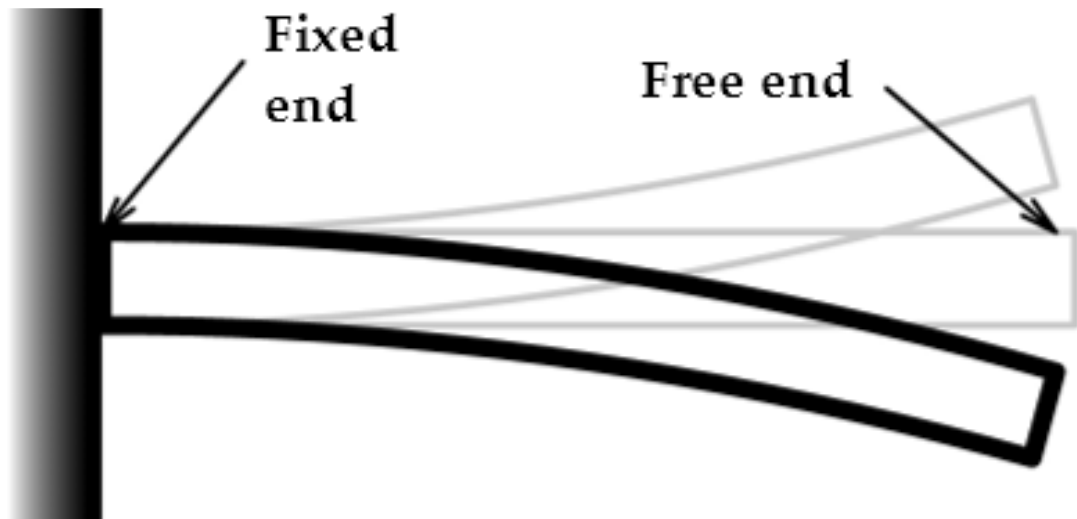
Figure 2.3. A fixed-free cantilever beam

$$\omega_n = 2\pi f_n = A_n \sqrt{\frac{EI}{mL^3}} \qquad (2.7)$$

where, E is the modulus of elasticity of the material, ω_n is angular natural frequency of nth mode, I is the moment of inertia, m is the mass and L the length of the beam. The values of A_n and hence the resonance frequencies are not harmonically related as shown in Table 2. [3].

Table 2.1

Modal frequency scale factors A_n (for $f_{n-1} = A_n f_0$) for various beam support conditions[4]

Boundary Condition	Mode 1 (f_0)	Mode 2 (f_1)	Mode 3(f_2)
Fixed-Free	3.52	22.0	61.7
Hinged-Hinged	9.87	39.5	88.9
Fixed-Fixed	22.4	61.7	121.0
Free-Free	22.4	61.7	121.0
Fixed-Hinged	15.4	50.0	104.0
Hinged-Free	15.4	50.0	104.0

Cantilevers (i.e. single end supported structures), can be modeled as a fixed-free system whereas, a BOS that is supported at both ends, is more appropriately modeled as a fixed-fixed system. The fixed boundary condition is defined as a condition where there is neither vertical nor horizontal movement of the structure at the support, while for the free condition, the end of the structure is not supported. The hinged-hinged boundary condition is considered as an intermediate support between fixed and free conditions. The hinged condition permits movement of the structure in both horizontal and vertical directions but the degree of the movement is smaller than for the free condition.

If the harmonics of a structure are well separated and non-overlapping, it is reasonable to model each resonance as a second order system. The spectrum of a second order system driven by white thermal energy, of RMS amplitude $\bar{x}$ is

$$S_x(f) = \frac{\bar{x}^2/(\pi Q f_0)}{\left(1-\left(\frac{f}{f_0}\right)^2\right)^2+\left(\frac{f}{Q f_0}\right)^2} \tag{2.8}$$

where

$$f_0 = \frac{1}{2\pi} \sqrt{k/m} \tag{2.9}$$

is the resonance frequency of the vibration. At resonance the spectral amplitude is maximum. The sharpness of the resonance is typically characterized by the "quality factor" $Q = 2\pi m f_0/\gamma$, which is also defined as

$$Q = \frac{f_0}{\Delta f} \tag{2.10}$$

where Δf is the bandwidth between the half-power points (Figs. B1-B3 of Appendix B).

2.4 Relating the lumped element model to distributed mechanical structures

Under the assumptions of small deflection and no mass loading, the equation of the motion of a homogenous beam with density ρ_s, length l, width b and thickness d can be written as[5]

$$\frac{EI}{l^4}\frac{\partial^4 y(\eta,t)}{\partial \eta^4} + c_1\frac{\partial y(\eta,t)}{\partial t} + (\rho_s A + c_2)\frac{\partial^2 y(\eta,t)}{\partial t^2} = 0 \tag{2.11}$$

where $\eta=x/l$ is the normalized length parameter (where x is position along the length of the beam), and $c_1=\beta_1/l$ is the dissipative drag parameter per unit length, $c_2=\beta_2/l$ is the inertial drag parameter per unit length and $A=bd$ is of cross sectional area. Drag force is the dissipative force of a vibrating beam from the fluid surrounding the medium. Drag force is

13

the dissipative force of a vibrating beam from the fluids surrounding the medium (such as air or water). For a beam velocity of $u = u_0 exp^{-j\omega t}$ the drag force can be expressed as[6]

$$P = \beta_1 v - \frac{\beta_2 u}{\omega}$$ (2.12)

Where, β_1 and β_2 are two real constants. The first part of this drag force is proportional to the velocity of the vibrating beam and called the dissipative drag force. This part is responsible for the energy dissipation of the beam. The second part depends on the acceleration of the beam and hence called the inertial drag force. The resonance frequencies for the beam are

$$\omega_{dn} = \left[\frac{ElA_n^4}{(\rho_s A + c_2)l^4} - \frac{1}{4}\left(\frac{c_1}{(\rho_s A + c_2)}\right)^2 \right]^{1/2}$$ (2.13)

Here, A_n is a constant that depends on the mode of vibration. It also varies with the width and the length of the vibrating beam.

For vibration in gas, dissipation represented by c_1 is very small and this term can be dropped. Moreover, if $\rho_s A$ is much larger than c_2, equation 2.12 simplifies to

$$\omega_{dn} = \omega_n \left(1 - \frac{1}{2}\frac{c_2}{\rho_s A} \right)$$ (2.14)

where, $\omega_n = 2\pi f_n$ is the undamped resonance frequency of the beam (eq. 2.7).

Q is derived from the stored energy (U_i) and the dissipative energy (U_d) of the beam as [3]

$$Q = \frac{2\pi * (stored\ vibration\ energy)}{dissipated\ energy\ per\ cycle} = \frac{2\pi U_i}{U_d}$$ (2.15)

The solution can be written in the form

$$y(\eta, t) = \omega(\eta)Y(t) = \omega(\eta)exp^{j\omega t}$$ (2.16)

Providing a separation of variables

and

$$U_i = (U_{kinetic})_{max}$$

$$= \int_0^1 \frac{1}{2} l \, (\rho_s A + c_2) \left| \left(\frac{\partial y(\eta, t)}{\partial t} \right)^2 \right|_{max} d\eta$$

$$= \frac{1}{2} l(\rho_s A + c_2) \omega^2 \int_0^1 \omega^2(\eta) d\eta \tag{2.17}$$

Energy dissipated per cycle, is the product of dissipative part of the drag force P and velocity u

$$U_d = \int_0^T Pu \, dt = \int_0^1 \int_0^T lc_1 \left(\frac{\partial y(\eta, t)}{\partial t} \right)^2 dt \, d\eta \tag{2.18}$$

Using these results in eq (2.15) gives

$$Q = \frac{2\pi \frac{1}{2} l(\rho_s A + c_2) \omega^2 \int_0^1 \omega^2(\eta) d\eta}{lc_1 \omega^2 \int_0^1 \omega^2(\eta) \int_0^T \cos^2 \omega t \, dt \, d\eta} \tag{2.19}$$

with the condition $c_2 \ll \rho_s A$, equation (2.19) simplifies to

$$Q = \frac{\rho_s A \omega}{c_1} \tag{2.20}$$

where $\omega = \omega_{dn}$ of eq.2.14.

2.4.1 Dependence of Q on air pressure

Q usually decreases with increasing air pressure. In equation 2.13, two factors c_1, and c_2 strongly depend on surrounding pressure. Pressure dependence can be classified into three regimes, intrinsic, molecular and viscous. [7]

Since damping due to various factors in all three contributions are proportional to velocity, then all the factors cause damping can be added together to calculate the net damping. If

F_a, F_b, F_c... are the individual damping forces at any of the three pressure regimes, then equation of net damping in that specific regime is

$$F = F_a + F_b + F_c \ldots$$

$$= (\beta_{a1} + j\beta_{a2})u + (\beta_{b1} + j\beta_{b2})u + \cdots$$

$$= ((\beta_1 + j\beta_2)u) \tag{2.21}$$

Now, in the calculation of the net quality factor, we are only interested in the dissipative parts of the drag forces. And the net quality factor Q for these combination of damping contributions can be calculated by using eqs. 2.15, 2.18 and 2.21 as

$$\frac{1}{Q} = \frac{1}{Q_1} + \frac{1}{Q_2} + \frac{1}{Q_3} \ldots = \sum_i \frac{1}{Q_i} \tag{2.22}$$

2.1.1.1 The intrinsic regime

The intrinsic regime corresponds to pressures between 10^{-2}-1 Pa. When the air pressure is extremely low there will be collisions between the vibrating structure and the molecules of the fluid; hence, damping would be extremely small compared to the intrinsic damping (c_I) of the vibrating object. The damping factor c_I and the quality factor do not depend on the air pressure or beam geometry. At this region, the damped resonance frequency ω_{dn} becomes equal to the undamped natural frequency ω_n (See eq. 2.14).

2.1.1.2 The molecular regime

When the air pressure is between 1-100 Pa, then the system is in the molecular region. In this region individual nonreactive air molecules collide with the vibrating beam and contribute to damping. The drag force in this region can be calculated using the kinetic

theory of gases. For a vibrating rectangular beam, the damping parameter c_1 is directly proportional to the air pressure P and the beam width b such that

$$c_1 = k_m b P \tag{2.23}$$

where the proportionality constant is

$$k_m = \left(\frac{32M}{9\pi RT}\right)^{1/2} \tag{2.24}$$

where M is molecular mass of the gas molecules, R is the ideal gas constant, and T is the absolute temperature in Kelvin.

In this region the inertial parameter c_2 is also zero. Using Eqs.2.14, 2.20 and 2.23, Q combines to give

$$Q = \frac{A_n^2}{k_m P}\left(\frac{d}{l}\right)^2\left(\frac{\rho_s E}{12}\right)^{1/2} \tag{2.25}$$

2.1.1.3   The viscous region

The experiments in this study are in this regime which obtains to pressures greater than 100 Pa. In this region damping is mostly due to the viscous drag of air. The drag force can be calculated by means of fluid mechanics. Since the velocity of a vibrating beam in air is always less than the velocity of the sound in air, the air can be modeled as incompressible medium.

If μ is the dynamic viscosity of air with a density of ρ_0, then the continuity equation for the velocity field $u(x,y,z,t)$ of air (Using the Navier-Stokes equation[6]) is

$$\frac{\partial u}{\partial t} + (u.\nabla)\mathrm{u} = -\frac{1}{\rho_0}\nabla P + \frac{\mu}{\rho_0}\Delta u, \tag{2.26}$$

17

$$\nabla.u = 0 \tag{2.27}$$

Equations (2.26) and (2.27) are helpful to solve the velocity of ideal structures; however, getting the velocity gradient analytically around a vibrating beam is extremely difficult. There are simpler methods like the one developed by Kokubun et al.[8-11]. They modeled a vibrating tuning fork as a string of small spheres. If these spheres are at infinite distance (to avoid Coulomb's and gravitational forces) from each other and vibrate independently, the resulting drag force of all the individual spheres is the net drag force on the vibrating tuning fork. H. Lamb also proposed a simplification[12] in which he approximated the drag force on a moving disk as the drag force on a sphere to model the vibration of cantilever. The solution of eqs. 2.26, 2.27 for Reynolds number Re<200 for a sphere gives a drag force of eq. 2.9 with[6]

$$c_1 = 6\pi\mu R \left(1 + \frac{R}{\delta}\right) \tag{2.28}$$

$$\frac{c_2}{\omega} = \frac{2}{3}\pi R^3 \rho_0 \left(1 + \frac{9}{2}\frac{\delta}{R}\right) \tag{2.29}$$

where

$$\delta = \left(\frac{2\mu}{\rho_0 \omega}\right)^{1/2} \tag{2.30}$$

is the width of the air boundary layer perpendicular to the direction of the motion of the vibrating object, where the air is turbulent, and it approximates the maximum space in the air where the air molecules collide with the object. δ depends inversely on the density of the air (which is proportional to air pressure) and the frequency of vibration.

Equation (2.28) has two parts; the first part is the Stokes drag coefficient law for a sphere in a viscous medium and the second part is the result of harmonic motion of the sphere[13] which depends both on the resonance frequency of the sphere as well as the density of the medium.

Assuming the damped resonance frequency ω_{dn} is equal to the undamped one ω_n (ignoring the inertial drag parameter c_2 in eq. 2.14), Q can be calculated by substituting the value of c_1 (eq. 2.28) and ω (eq. 2.14) into eq.2.20 (ignoring eq.2.29 to eliminate c_2)

$$Q = \frac{k_n^2 \sqrt{\rho_s EIA}}{6\pi\mu R \left(1 + \frac{R}{\delta}\right) l} \tag{2.31}$$

The corresponding resonance frequency shift due to the damping can be calculated by combining equations (2.14), (2.24) and (2.29)

$$\frac{f_{01} - f_{02}}{f_{01}} = \frac{\pi R^3}{3l\rho_s A} \frac{1}{R_0 T} \left(MP + \frac{9}{2} \frac{\sqrt{\frac{MP\mu R_0 T}{\pi f}}}{R} \right) \tag{2.32}$$

This model assumes that pressures the velocity of the air close to the vibrating beam moves at the same velocity as the beam. Later Kokubun et al.[10] revised his theory to incorporate Millikan's slip theory[14]. The later theory explains the pressure dependence of the quality factor when the system is moved between the three pressure regimes.

Table2.2
Summary of effect of air pressure on quality factor of vibration

Region	Mechanism	Effect on Q
Intrinsic (10^{-2}-1 Pa)	Extremely low pressure so that air damping is negligible compared to the	Dissipative drag parameter c_l and corresponding Q are independent of the beam geometry.

	intrinsic damping of the vibrating beam.	
Molecular or Knudsen (1-100 Pa)	At medium pressure (value depends of the geometry of the vibrating structures) damping is caused by independent collisions of nonreacting air molecules at the vibrating surface of the beam.	Dissipative drag parameter c_l increases proportionally with air pressure and beam width. The value of Q decreases with increasing air pressure
Viscous (>100 Pa)	Up to atmospheric pressure or above (also depends on the geometry of the structures). Excess amount of air acts as an incompressible viscous fluid	1. For $R/\delta << 1$ (see eq. 2.28) Q is independent of air pressure, because delta drops out. 2. For $R/\delta >> 1$ Q decreases with pressure

Both the glass fibers in chapter 5 and BOS fibers in chapter 6 are modeled as vibrating beams that include the geometric and material parameters of these micro/nanostructures. It has been shown that the fundamental resonance at f_0 is related to the lumped element model. Equations 2.8, 2.9 and 2.31 are used to model power spectral density, resonance frequencies and quality factors of the measured vibration signal.

2.5 Detection Noise Sources
While the objective of this study is to measure the thermal noise driven vibrations of micro-nano structures, there are other noises present in the vibration detection instrumentation that must be taken in to account, and preferably reduced to levels below that of the thermal vibrations.

2.5.1 Shot noise

Variation in currents due to a random arrival of photoelectrons is called shot noise. Laser sources and photodetectors, both exhibit shot noise. Shot noise is modeled as the stationary random process

$$X(t) = \sum_{k=-\alpha}^{\alpha} b(t - \tau_k) \qquad (2.33)$$

Where τ_k, is arrival time of an electron and k ranges from negative infinity to positive infinity. The average number of electrons (or shots) V arriving in the time interval t_0 is

$$E(V) = \lambda t_0 \qquad (2.34)$$

where λ is called the rate constant. V follows a Poisson distribution

$$P(V = k) = \frac{(\lambda t_0)^k}{k!} e^{-\lambda t_0} \qquad k=0,1,2,3... \qquad (2.35)$$

where P is the probability of k electrons arriving in the time interval t_o. One sided power spectral density of the shot noise is directly proportional to the average power of the light source. For a laser operating at a frequency of v with an average power of $\bar{P}$ has a power spectral density of

$$S(f) = 2hv\bar{P} \qquad (2.35a)$$

2.5.2 1/f noise

The physical origin of 1/f noise (also known as flicker or pink noise) is not well understood[15]. It is a low frequency noise where power is inversely proportional to the frequency. At very low frequencies 1/f noise dominates over white (Brownian) noise (see Fig. 2.4). The First Sensor QPD used in this study (Fig. 2.12) is followed by an op-amp (ADA4622-2)
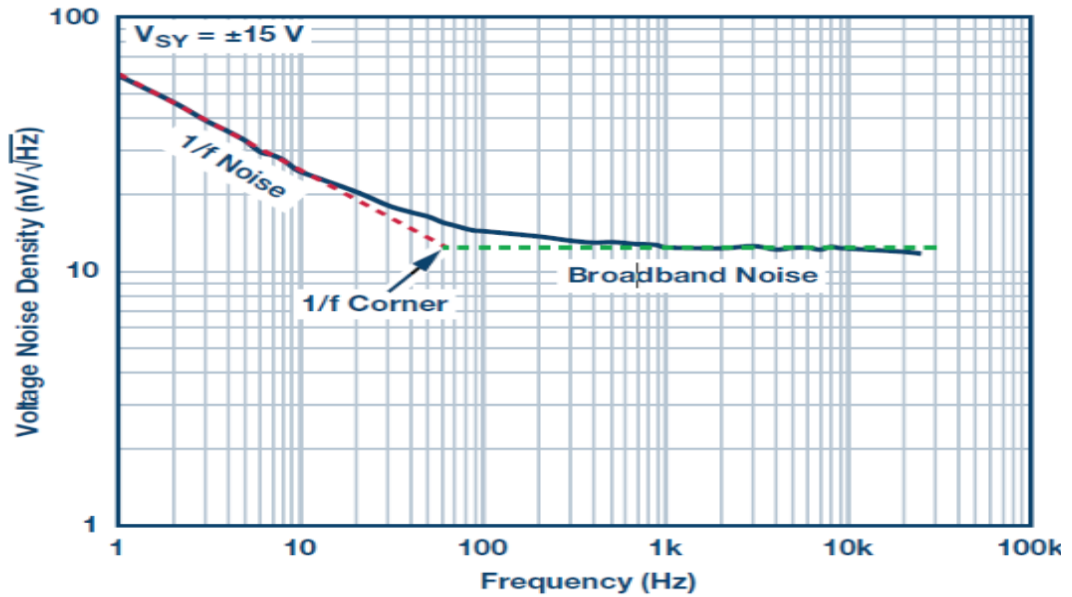
Figure 2.4. Voltage noise spectral density of an op-amp ADA4622-2 op-amp. Image from [16]

This op-amp[16] (Fig. 2.13) has a typical noise power spectrum (Fig. 2.4) that is dominated by 1/f noise below ~100 Hz (Fig. 2.4). 1/f noise can be described as

$$P_{rms} = en_{1Hz} \left(\sqrt{ln\left(\frac{f_h}{f_1}\right)} \right) \tag{2.36}$$

Where P$_{rms}$ is the total 1/f noise power, en_{1Hz} is the noise density at 1 Hz, f_h is the *1/f* noise corner frequency, and f_1 is 1/aperture time (total measurement time).

2.5.3 Thermal/White noise in electronic detectors

Electrons in a conductor are also subject to thermal white noise. This type of noise is known as thermal or Johnson noise. The mean square value of thermal noise voltage V_{tn} in a conductor of resistance R, within a bandwidth of $B=1/\tau$, where τ is the response time of the measuring device, and absolute temperature T is

$$E[V_{tn}^2] = 4k_b RTB \qquad (2.37)$$

Where k_b is Boltzmann's constant. This noise can be modeled as a Thevenin equivalent circuit with a voltage source of mean square value $E[V_{tn}^2]$ and a series noiseless resistor R, or as a Norton equivalent circuit with a current source of mean square value

$$E[I_n^2] = \frac{1}{R^2} E[V_{tn}^2] \qquad (2.38)$$

and a noiseless resistor in parallel, as shown in Fig. 2.5.
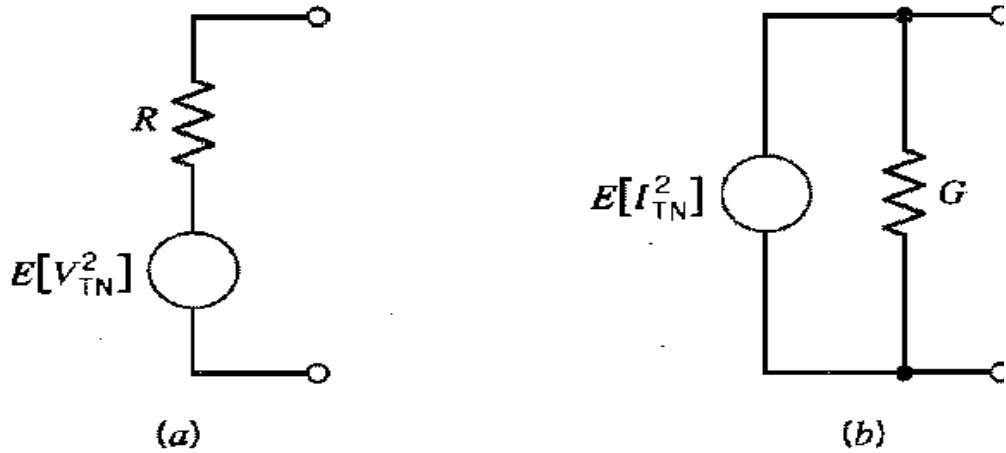
Figure 2.5. Equivalent circuits for thermal noise modeling
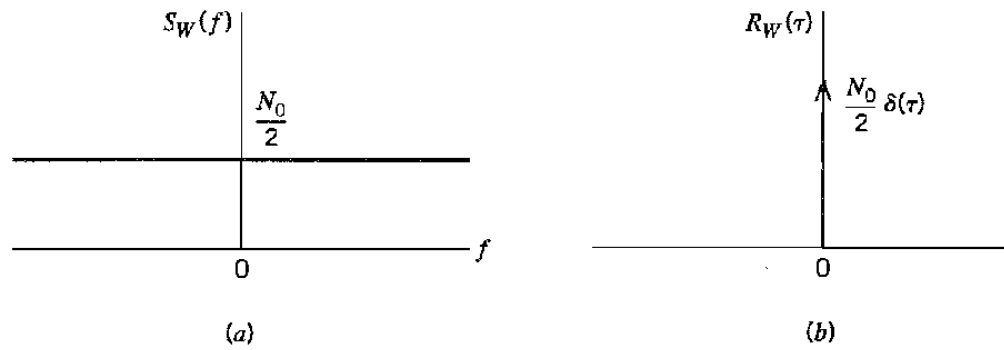
Figure 2.6. a) Spectrum and b) autocorrelation function of white noise

White noise is a random signal having a spectrum of uniform power spectral density $S_w(f) = \frac{N_0}{2}$ as shown in Fig. 2.6a.

N_0 can be expressed in terms of the equivalent noise temperature T_e is as

$$N_0 = k_b T_e \tag{2.39}$$

Where, T_e is called the equivalent noise temperature that expresses the temperature required to generate a certain level of noise power[17] by an electronic device.

2.5.4 Band-limited White noise

Band limited white noise results when a white Gaussian noise $n(t)$ with zero mean with power spectral density of $N_0/2$ is passed through a unity gain band pass filter as shown in Fig. 2.7 with a bandwidth of $2B$ at central frequency f_0.

The autocorrelation function of band limited white noise is the inverse Fourier transform of the power spectral density.

$$R_N(\tau) = \int_{-f_c-B}^{-f_c+B} \frac{N_0}{2} \exp(j2\pi f\tau)\, df + \int_{f_c-B}^{f_c+B} \frac{N_0}{2} \exp(j2\pi f\tau)\, df$$

$$= N_0 B sinc(2B\tau)[\exp(-j2\,\pi f_c\tau) + \exp(2\,\pi f_c\tau)]$$

$$= 2N_0 B sinc(2B\tau)\cos(2\,\pi f_c\tau) \tag{2.40}$$

where

$$sinc(x) = \begin{cases} 1 & for\ x = 0 \\ \dfrac{sinx}{x} & otherwise, \end{cases}$$
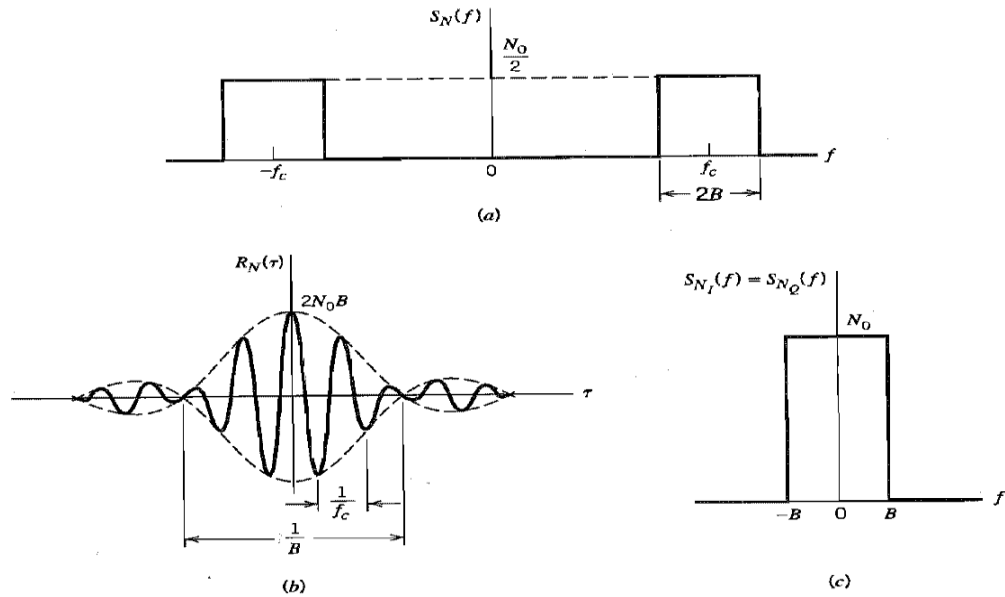
Figure 2.7. Band limited white noise and its a) two-sided power spectrum b) auto-correlation function of impulse response c) one sided power spectrum (demodulated spectrum of the envelop of (b))

25

2.6 Detection of nanomechanical vibration

Displacement measurements of thermal vibrations of micro and nanoobjects have been used to measure the stiffness of laser optical traps[18, 19] and atomic force cantilevers (AFM)[20, 21], in particle tracking[22], in optical manipulation of viruses and bacteria[23], in determining elastic properties of materials[24], and in quantifiable detection of small amounts of adsorbed mass on micro-nano-mechanical structures[25].

Ultra-small position detection is used in many scientific measurements to determine other properties of a sample. For instance, accuracy of stiffness calibration of AFM cantilevers depends on the accuracy of the detected position of the cantilever tip[20, 26-30]. Position detection is also fundamental in optical trapping for the measurement of the trap stiffness [31-37], experimenting with molecular motors[38-46], measuring the mechanical properties of polymers[47-50], and the study of colloid particles[51-54]. The various optical detection methods in Fig. 2.8 are reviewed below
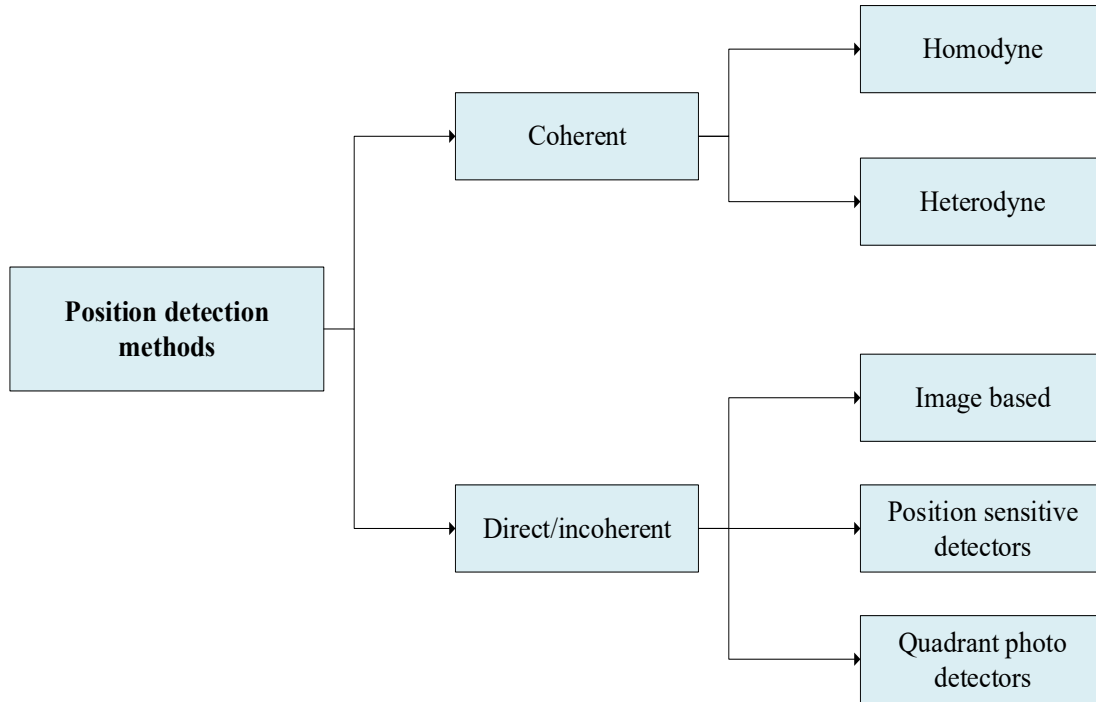
Figure 2.8. Optics based position detection methods

The vibration of objects can modulate light which can be photo-detected. There are two general classes of optical detection: incoherent and coherent. In incoherent or direct detection, the time-average intensity of the light is directly detected. In coherent detection light from the object is interfered with a reference beam and the difference or beat signal is sensed on the face of the detector (e.g. a photodiode or photomultiplier tube) [55-57]. If the object and reference beams are at the same wavelength or frequency, the method is referred to as homodyne detection[58-61]. If the beams are at two different frequencies, the method is referred to as heterodyne detection[57, 62-64]. These methods, while theoretically the most sensitive, also require additional circuitry to stabilize the light frequencies and path-length changes. Incoherent, or direct detection, while not as sensitive as coherent detection, does not require stabilization. When the displacements are relatively large and the frequencies being measured are relatively small, video imaging methods can

27

be used as incoherent detectors of vibration[65, 66]. Non imaging techniques uses position sensitive detectors (PSD)[67] and quadrant photodetectors (QPD)[68].

2.6.1 Incoherent detection

Incoherent detection unlike optical coherent detection, ignores the phase information of the light. Incoherent detection devices include CMOS cameras, position sensitive detectors (PSD) and quadrant photo detectors (QPD). Incoherent detection using each type of detector is presented here.

2.6.1.1 Image based position detection

A camera records a sequence of images of the object. Then the centroid of object is calculated and monitored over time [69-73]. Standard camera frame rates (typically 50-120 Hz) are somewhat slower than the vibration frequencies of interest in this study. Specialized cameras can run much faster, but also increase the amount of data processed and computation time required. For example, for a 40 kHz camera (with a picture of 800×600 pixels), and a 2004 version of CPU microprocessor with a clock speed of 3.4GHz, the video-based detection is limited to 500Hz. Today with a core I7 processor (using parallel processing) with similar clock speed up to 3.5 KHz vibration is detectable.

2.6.1.2 Position sensitive detector (PSD) based detection

Position sensitive detectors (PSDs) are optoelectronic sensors that utilize surface resistance of a photo diode to measure the change in position of a light spot. There are two categories of PSDs: lateral effect PSDs and segmented PSDs. PSDs are manufactured both as one-dimensional and two-dimensional detectors. One-dimensional PSDs are used to

measure both linear and rotational displacements. Figs. 2.9 and 2.10 illustrate the displacement measuring principle for a 1-D PSD[74].
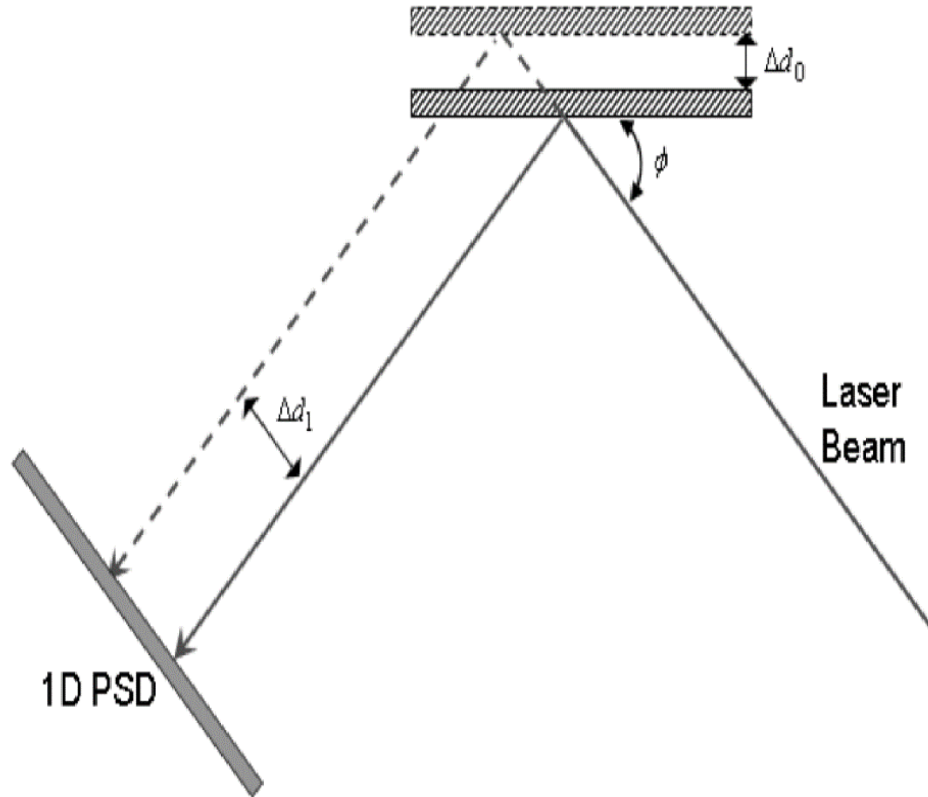
Figure 2.9. Linear displacement measurement using a 1-D PSD. Image from [74]

In linear displacement measurement, a light source such as a laser beam, is projected toward the target object. The position of the reflected beam is then sensed with the PSD. A displacement of the target in Fig. 2.9 by Δd_0, displaces the laser beam by Δd_1. The displacement of the target is

$$\Delta d_o = \frac{\Delta d_1}{2\cos\emptyset} \tag{2.42}$$

where $\emptyset$ is the angle of reflection.
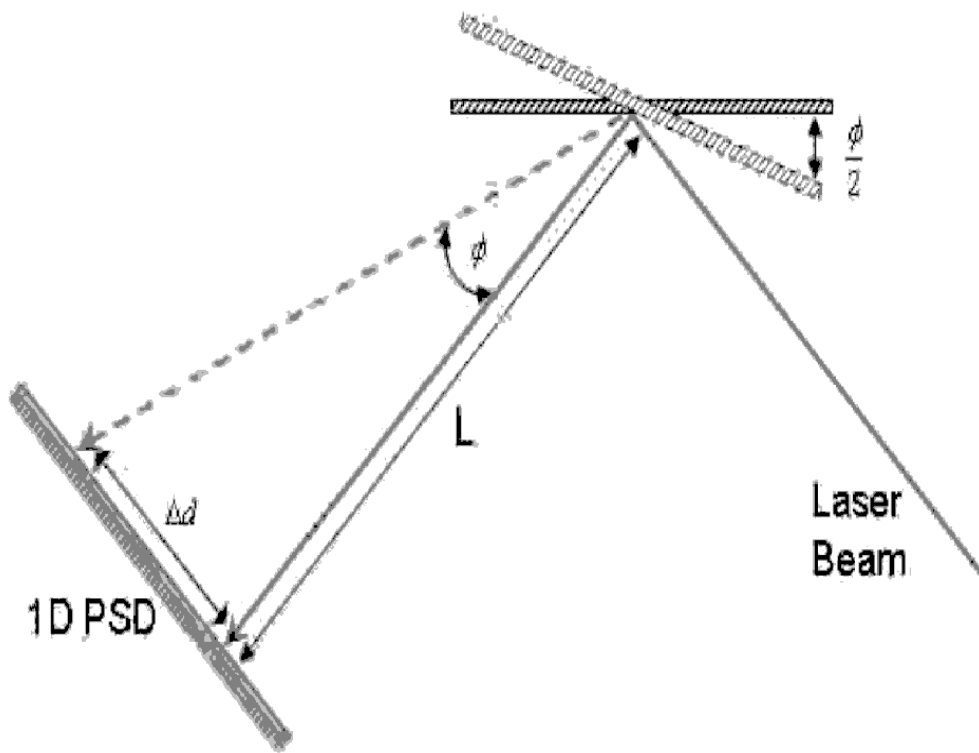
Figure 2.10. Displacement on a PSD due to rotation of the object. Image from [74]

If the target is rotated by angle $\emptyset/2$ (Fig. 2.10), the laser beam is displaced by Δd at a distance of L between the object and the PSD. The angle can be calculated from Δd as

$$\frac{\emptyset}{2} = \tan^{-1}\left(\frac{2\Delta d}{L}\right) \tag{2.43}$$

Fig. 2.11 is a schematic cross section of a lateral effect 1-D PSD. Devices are available both as p-n junction photodiodes or Schottky diodes with two anodes and a common cathode.
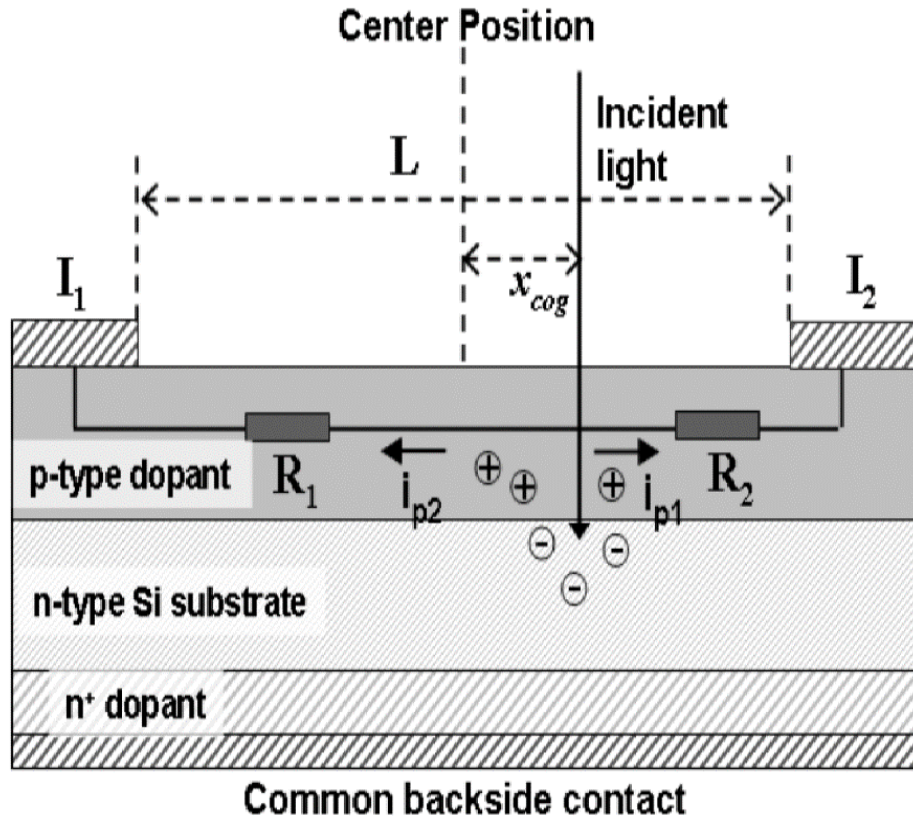
Figure 2.11. Cross section of a lateral effect PSD. Image from [74]

Light incident on the active area of the PSD generates electron hole pair that flow through the bulk resistances R1 and R2 as currents I_1 and I_2. The currents are inversely proportional to the lengths between the position of the incident light and the anodes. Besides the small errors in eq.2.42 the currents are converted to position

$$x_{cog} = \frac{L}{2} \cdot \frac{(I_2 - I_1)}{I_2 + I_1}$$ (2.44)

The position ranges from – L/2 to +L/2.

2.6.1.3 QPD based position detection

Quadrant photodiode detectors (QPD) are composed of four closely spaced photodiodes (Fig. 2.12), that outputs centroid of the incident optical beam. Low noise is achieved by the integration of a low noise preamp with each photodiode. As a result, QPDs have demonstrated sub-nanometer position detection of AFM cantilever position [20, 26, 75], bead position and stiffness determination of optical traps[76-78]. QPDs also have been used to detect position in light detection and ranging (LIDAR), robotics[79], inter-satellite communication[80], and laser space communication[81].
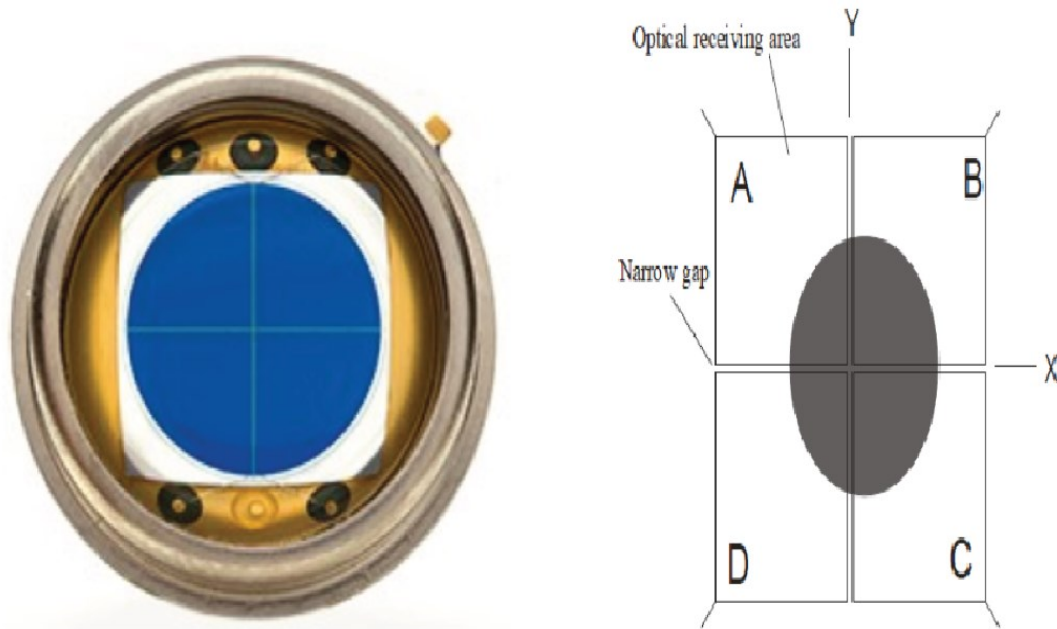
Figure 2.12. A (a) packaged First Sensor QPD and (b) schematic of a QPD. Image b) from [82]

QPDs used in this study include an electronic component (Fig. 2.12a) and as a complete module (Thorlabs, not shown) that directly interfaces to a computer. The device has higher sensitivity and lower noise than the complete module.
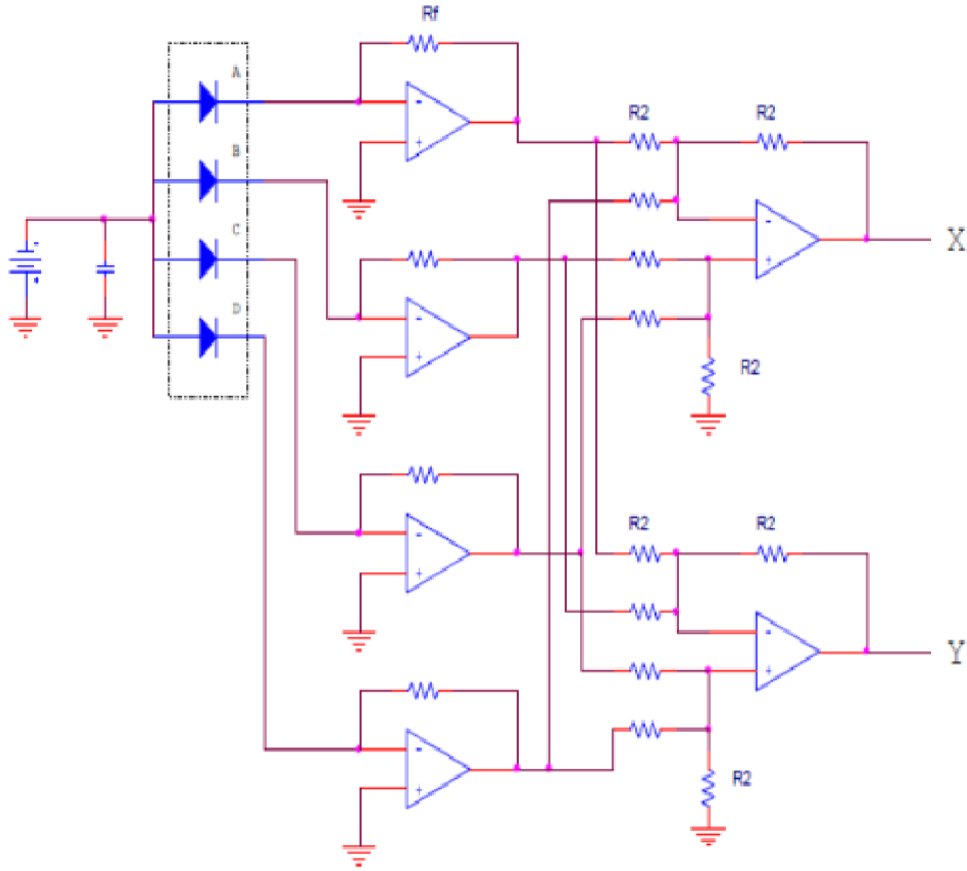
Figure 2.13. Driver circuitry for a QPD readout. Schematic from [82]

Fig. 2.13 is a schematic of a QPD drive circuit[82]. Each diode represents one segment A-D of the QPD in Fig. 2.12b. Each diode is followed by a low noise transimpedance op amp. The amplifier outputs are combined to produce the x and y outputs

$$X_{position} = S_x \frac{(V_A + V_D) - (V_B + V_C)}{(V_A + V_B + V_C + V_D)} \tag{2.45}$$

$$Y_{position} = S_y \frac{(V_A + V_B) - (V_D + V_C)}{(V_A + V_B + V_C + V_D)} \tag{2.46}$$

Where V_x correspond to the photovoltages generated by each of the four diodes. The proportionalities S_x and S_y, also known as the sensitivity factors (Sec.4.8), depend on

the laser spot shape, power and distribution of intensities on the QPD surface. The conditions for maximizing position detection sensitivity are: The laser spot should be large enough to cover most of the sensor area. A laser spot wider than the sensor active area loses sensitivity due both to lowering of the detected spot energy, and also to the incident portion of the spot profile being more uniform in intensity. However, de-magnifying the spot smaller than necessary, also de-magnifies its displacement and similarly reduces sensitivity. Detailed analysis of the conditions chosen to optimize position detection of the micro/nanostructures measured in this study are presented in Sec. 3.4-3.6.

2.6.1.3.1 Signal to noise ratio of QPD detection

The signal to noise ratio is modeled by considering the ratio of signal level (of single QPD diode) to the background noise. For simplification (of circuit in Fig. 2.13), it is assumed that $R_F=R_2=R_L$. For this condition, power spectral densities the voltage noises $\langle v_{Xn}^2 \rangle$ and $\langle v_{Yn}^2 \rangle$ at the output of the transimpedance amplifier can be simplified to[83]

$$\langle v_{Xn}^2 \rangle \approx \langle v_{Yn}^2 \rangle \approx R^2 \langle i_n^2 \rangle + \frac{55}{16} \langle e_n^2 \rangle + \frac{1}{8} R_L^2 eI + 9kTR_L \qquad (2.47)$$

Where $\langle i_n^2 \rangle$ and $\langle v_n^2 \rangle$ are the squared average noise levels of op-amp input current and voltage noises respectively. e is the electron charge, I is the net bias current, R_L is the load resistance of the measurement system (NI A/D card, optical power meter, oscilloscope etc.) and T is the temperature. The SNR at each QPD output terminal is

$$SNR_X = \frac{R_L^2 i_x^2}{\langle v_{Xn}^2 \rangle} = \frac{1}{16} \frac{[(i_A + i_D) - (i_B + i_C)]^2}{\left(\langle i_n^2 \rangle + \frac{55}{16R_L^2} \langle e_n^2 \rangle + \frac{1}{8} eI + \frac{9kT}{R_L} \right) \Delta f} \qquad (2.48)$$

$$SNR_Y = \frac{R_L^2 i_y^2}{\langle v_{Yn}^2 \rangle} = \frac{1}{16} \frac{[(i_A + i_B) - (i_C + i_D)]^2}{\left(\langle i_n^2 \rangle + \frac{55}{16R_L^2} \langle e_n^2 \rangle + \frac{1}{8} eI + \frac{9kT}{R_L} \right) \Delta f} \tag{2.49}$$

where, Δf is the bandwidth of the measurement system. The factor 16 in the denominators

of eqs.2.48 and 2.49 comes from the relation $I_x = \frac{1}{4}[(i_A + i_D) - (i_B + i_C)]$[84]. The signal

to noise ratio is proportional to the power, while the displacement measured is proportional

to current. Therefore, the displacement sensitivity increases by increasing the power of the

optical source. The maximum SNR achieved in this study is reported in chapter 4.

2.6.1.4 Noise equivalent power (NEP) of an optical detector

Sensitivity of photodiodes is expressed in terms of minimum detectable optical

power or noise equivalent power (NEP). NEP is the detected optical power that produces

a detected electrical signal of equal power to the noise power of the detector. NEP of a

detector is limited by shot and thermal noises.

The time-average current generated by a photodiode (i.e. the frequency of the laser

oscillation is averaged out by the detector) when exposed to an amplitude modulated

optical signal is

$$i(t) = Re\left[\frac{Pe\eta}{h\upsilon}\left(1 + \frac{m^2}{2}\right) + \frac{Pe\eta}{h\upsilon} 2m\left(\frac{1 - e^{-i\omega_m \tau_d}}{i\omega_m \tau_d}\right) e^{i\omega_m t} \right] \tag{2.50}$$

Where P is the amount of input power when $m=0$, η is the quantum efficiency of the

detector, m is the modulation index, and υ is the frequency of the incident light, e is the

charge of an electron, h is plank's constant ω_m is the modulating frequency. The factor in

the second set of parentheses in eq. 2.50 represents the phase lag as well as the reduction

in signal current due to the detector rise time τ_d. For detected frequencies well below the response time such that

$$\omega_m \ll \frac{1}{\tau_d} = \frac{1}{R_e C_d}$$

where R_e is the diode incremental (ac) resistance and C_d is the junction capacitance, the second term in parentheses in equation (2.50) approaches unity giving

$$i(t) = Re\left[\frac{Pe\eta}{h\upsilon}\left(1 + \frac{m^2}{2}\right) + \frac{Pe\eta}{h\upsilon}2me^{i\omega_m t}\right] \tag{2.51}$$

2.6.1.4.1 Detection in the presence of noise

For unit modulation index $m=1$, the photogenerated current due to the optical signal

$$\overline{i_s^2} = 2\left(\frac{Pe\eta}{h\upsilon}\right)^2 \tag{2.52}$$

There are two noise sources present in the detection, the first one is the shot noise, source as described earlier due to the random arrival of photons on the detector, and can be written

$$\overline{i_{n1}^2} = \frac{3e^2(P+P_B)\eta\Delta f}{h\upsilon} + 2ei_d\Delta f \tag{2.53}$$

Where Δf is the bandwidth of the detection, P_B is the background optical power and i_d is the dark current in the absence of any signal power. The second source represents the Johnson or thermal noise generated due to the output load and can be expressed as

$$\overline{i_{n2}^2} = \frac{4kT_e\Delta f}{R_L} \tag{2.54}$$

Where T_e is the noise equivalent temperature and R_L is the load resistance of the measurement apparatus (e.g. optical power meter or oscilloscope). Combining eq. 2.52, eq. 2.53 and eq. 2.54, the signal to noise ratio is

$$SNR = \frac{\overline{i_s^2}}{\overline{i_{n1}^2}+\overline{i_{n2}^2}} = \frac{2\left(\frac{Pe\eta}{h\upsilon}\right)^2}{\frac{3e^2(P+P_B)\eta\Delta f}{h\upsilon}+2ei_d\Delta f+\frac{4kT_e\Delta f}{R_L}} \tag{2.55}$$

36

When the input signal is very close to the detection limit of the detector (i.e. S/N=1) the shot noise is much smaller than the thermally generated Johnson noise and in that case eq. 2.55 simplifies to

$$SNR = \frac{2\left(\frac{Pe\eta}{h\upsilon}\right)^2}{\frac{4kT_e\Delta f}{R_L}} \tag{2.56}$$

Minimum detectable power found for SNR=1 and $P_B = 0$ to be

$$P_{min} = \frac{h\upsilon}{e\eta}\sqrt{\frac{2kT_e\Delta f}{R_L}} \tag{2.57}$$

The noise equivalent power (NEP) is calculated by simply dividing it P_{min} by the system bandwidth. However, we did not have proper equipment to measure all the quantities in eq. (2.57) and so used an intensity modulation approach to measure NEP directly. The technique is described in next section. In addition, neglection of 1/f noise at low frequencies can lead to underestimation of P_{min}. Corrections for 1/f noise are considered in Sec. 2.8.2.

Similarly, for SNR=0, eqs. 2.48 and 2.49 for QPDs give

$$P_{min} = \frac{\langle v_{Xn}^2\rangle\Delta f}{R_L} = \left[R_L\langle i_n^2\rangle + \frac{55}{16R_L}\langle e_n^2\rangle + \frac{1}{8}R_L qI + 9kT\right]\Delta f \tag{2.57a}$$

2.6.1.4.2 Intensity modulation of laser beam

The minimum detectable optical power of a photodetector (or a QPD) is measured by using an optical chopper as shown in Fig. 2.14. Choppers are used because they provide 100% depth of modulation (i.e. m=1 in eq. 2.51).
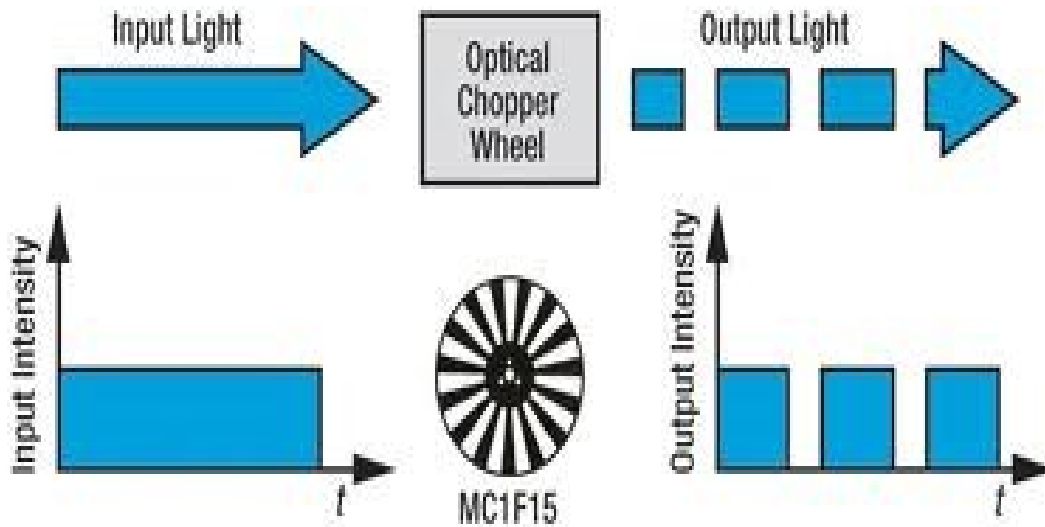
Figure 2.14. Intensity modulation of a laser beam

Before passing the light through the optical chopper, the intensity of the incident light is constant over time and the chopper modulates the intensity of the light with a square wave. The intensity is detected by the detector being characterized and the signal is recorded using a PC-interfaced A/D card. The spectrum of the detected signal is calculated by the fast fourier transform (FFT). The minimum detectable power, or NEP, of the detection system is found by lowering the optical power to the level where it is detected at the same level as the detector noise. The chopper frequency is selected to avoid various background interference, especially leaking from 60 Hz line frequency and its harmonics.

2.6.2 Coherent detection

In coherent detection the electric field of a reference beam is interfered with the electric field of the modulated beam to demodulate the modulation signal. Coherent detection can either be homodyne or heterodyne. For homodyne detection, the sense and reference beams are at the same frequency and the interference of the two beams gives the signal. For heterodyne detection, the interference of the two beams gives the signal modulated at the difference frequency of the two beams. The theory for these two detection schemes are presented next.

2.6.2.1 Optical heterodyne detection

This form of optical interferometry provides low noise amplification. The main concept is similar to the radio-frequency technique used in the superheterodyne receiver where a reference oscillator amplifies the weak radio signal while improving the overall signal to noise ratio (SNR). Fig. 2.15. shows a block diagram of an optical heterodyne receiver. This optical detection technique was demonstrated in 1963 by S. F. Jacobs[85]. Optical heterodyne detection works well under the following set of restrictions.

- **Coherent superposition**

  Coherence between both beams require that they interfere. Therefore, the two beam must be of the same polarization and one beam must be delayed from the other by less than the coherence length of the light.

- **Power requirement**

To achieve a reasonable gain for a weak optical signal, the power of the reference oscillator must be very large compared to the signal.

- **Fluctuation of the laser frequency:**

Ideally output of a laser light is monochromatic. In reality, no laser is perfectly monochromatic. All lasers generate some degree of shot noise as part of their lasing output. Laser generated shot noise is given by

$$i_{shot\ noise(rms)} = (2ei_{dc}\Delta f)^{1/2} \qquad (2.58)$$

Where Δf is the bandwidth of the reference oscillator and i_{dc} is the dark noise current generated when the reference oscillator is on.
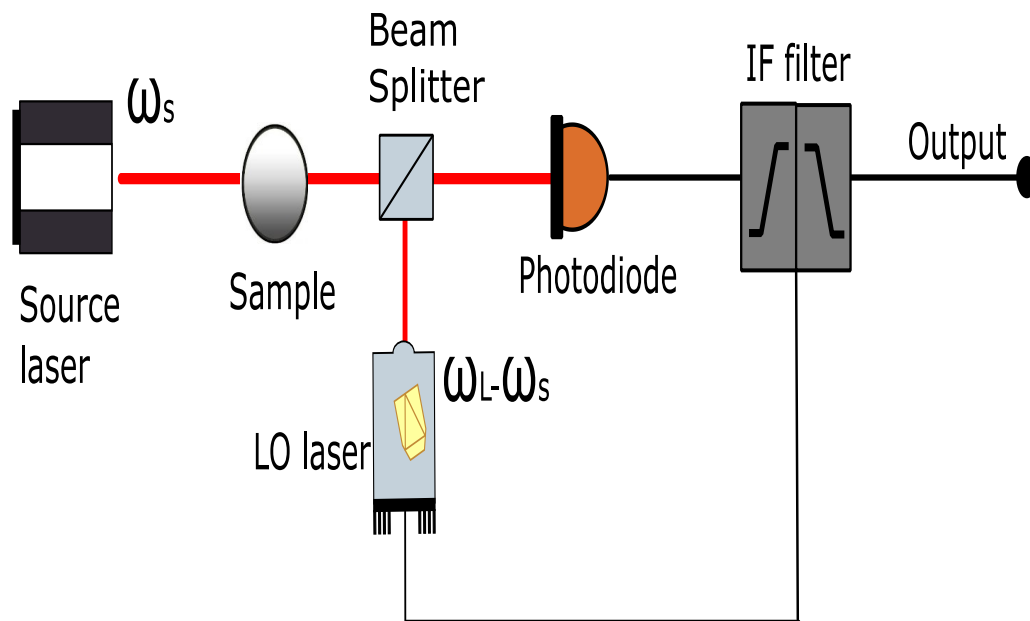
Figure 2.15. Schematic of a heterodyne detection optical receiver

2.6.2.1.1 Signal to noise ratio in heterodyne detection

Let E_L and E_s be the electric field amplitudes of the reference oscillator and the signal, respectively. The signal and reference oscillator fields add coherently on the photodetector giving a total field as[86]

$$E = E_L cos\omega_L t + E_S cos\omega_S t \tag{2.59}$$

The photocurrent is proportional to the intensity of the superimposed signal

$$i \sim E^2 = \frac{1}{2}E_L^2 + E_L E_S \cos(\omega_L - \omega_S)\, t + \frac{1}{2}E_S^2 \tag{2.60}$$

The signal amplitude E_s is detected when detector bandwidth exceeds the difference frequency. Expressed in terms of the rise time of the detector τ, then the signal is detected if

$$\omega_L - \omega_S < \frac{1}{\tau} < \omega_L \tag{2.61}$$

Ratio of the signal to the unmodulated detection from eq.2.60 can be rearranged as

$$i_{ac} = \left[\frac{2E_L E_S}{E_L^2 + E_S^2}\right] i_{dc} \tag{2.62}$$

Where $i_{peak\, ac}$ is the peak value of current generated in the photodetector due to the information signal. When $E_L \gg E_S$, as is assumed (see section 2.6.2.1), the equation can be rewritten as

$$i_{ac} = \left(\frac{2E_S}{E_L}\right) i_{dc} \tag{2.63}$$

Squaring both sides

$$(i_{ac})^2 = \left[2\left(\frac{E_S}{E_L}\right) i_{dc}\right]^2$$

$$= 4\left(\frac{P_S}{P_L}\right) i_{dc}^2 = 2\left(\frac{\eta e}{h\nu}\right) P_L P_S \tag{2.64}$$

41

This shows that the mean square AC signal power increases proportionally with reference oscillator power, providing gain. The dc component of the current is given by

$$i_{dc} = \frac{\eta P_L e}{h\nu} \tag{2.65}$$

Where, h is planck's constant, η is the quantum efficiency of the detector, P_L is the reference oscillator power, and e is the charge of a single electron.

The signal to noise ratio by using eqs. 2.58, 2.64 and 2.65 is

$$SNR = \frac{i_{ac}^2}{i_n^2}$$

$$= \frac{\eta P_s}{h\nu\Delta f} = \eta \frac{signal\ photon\ rate}{detection\ bandwidth} \tag{2.66}$$

This result shows that the SNR is independent of reference oscillator power.

2.7 Homodyne detection
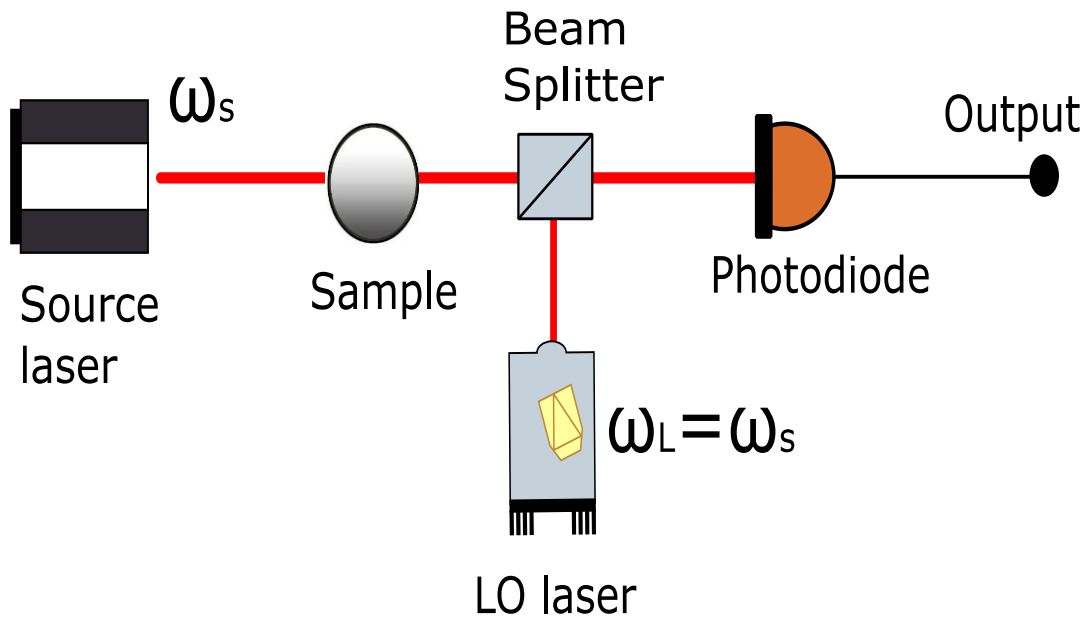
Figure 2.16. Schematic of a homodyne detection optical receiver

Fig. 2.16 is a schematic of coherent homodyne detection[87]. The only difference for the homodyne detection is that the source is at the same frequency as the local oscillator (LO).

2.7.1.1.1 Sensitivity of homodyne detection

The current generated by a photodetector in a homodyne detection can be expressed as[87]

$$I_{hom} = R_L(P_S + P_L) + 2R_L(P_SP_L)^{\frac{1}{2}}cos\varphi_p(t) \tag{2.67}$$

Where P_S and P_L are the power of source and reference oscillator lasers respectively. Equation (2.67) indicates that the current in the photodiode can be increased by both increasing the power of the reference oscillator as well as the sensitivity of the detector. The power of the reference oscillator can be increased as long as the total amount of light is below the saturation limit of the detector. For a homodyne detector with high reference oscillator power, shot noise from the signal current, thermal noise and dark-current noise (see sec.2.5) can be ignored. Signal amplitude to noise current (signal-to-noise ratio SNR or S/N) for a homodyne detection is

$$SNR = \frac{\left(2R_L(P_SP_L)^{\frac{1}{2}}\right)^2 R_L}{\left(2q\Delta f R_L P_L + \frac{4kT\Delta f}{R_L}\right)R_L}$$

$$\approx \frac{R_i P_S}{q\Delta f} = \frac{2\eta P_S}{hv\Delta f} \qquad \text{for } R_L \gg 4kT\Delta f \tag{2.68}$$

The SNR of homodyne detection is twice the SNR of heterodyne because of using two optical sources of same frequency.

2.7.2 Mixed position detection methods

This section reviews two other types of nanostructure position sensing. These are polarization interferometry and back focal plane detection.

2.7.2.1 Polarization interferometry

In polarization interferometry (PI), polarization of light can be used to measure the displacement of objects of all scales, from molecules to stars [88-91]. In PI, plane polarized light is split into two laterally displaced beams by a Wollaston prism. One beam is passed through a vibrating object and then the two beams are recombined using a second Wollaston prism. If the object is stationary, the polarization of the transmitted light is unchanged from the incident light. If the object moves, the resulting polarization is elliptically polarized. The larger the displacement, the greater the polarization shift of the probe beam. The polarization is measured by rotating a polarizer to find the maximum and minimum intensities of linear polarizations which define the major and minor axes of the polarization ellipse.

2.7.2.2 Back focal plane detection

Back focal plane detection (BFP) uses the interference between forward scattered light from the vibrating sample with the non-scattered light [92-95] to improve the contrast of the object. Fig. 2.17 shows a BFP set-up used to measure the position of a sample. Here, the condenser lens is used both for illuminating the sample as well as imaging the object onto the QPD. The dichroic mirror permits the laser beam to pass to the sample but reflects the incoming light from the sample to the QPD. The light pattern at the back focal plane of

the condenser lens is collected by a relay lens and imaged onto the QPD. The QPD is placed at a conjugate of the back focal plane of the condensing laser and the interfered signal is captured. The displacement of the object is calculated from the interfered signal.
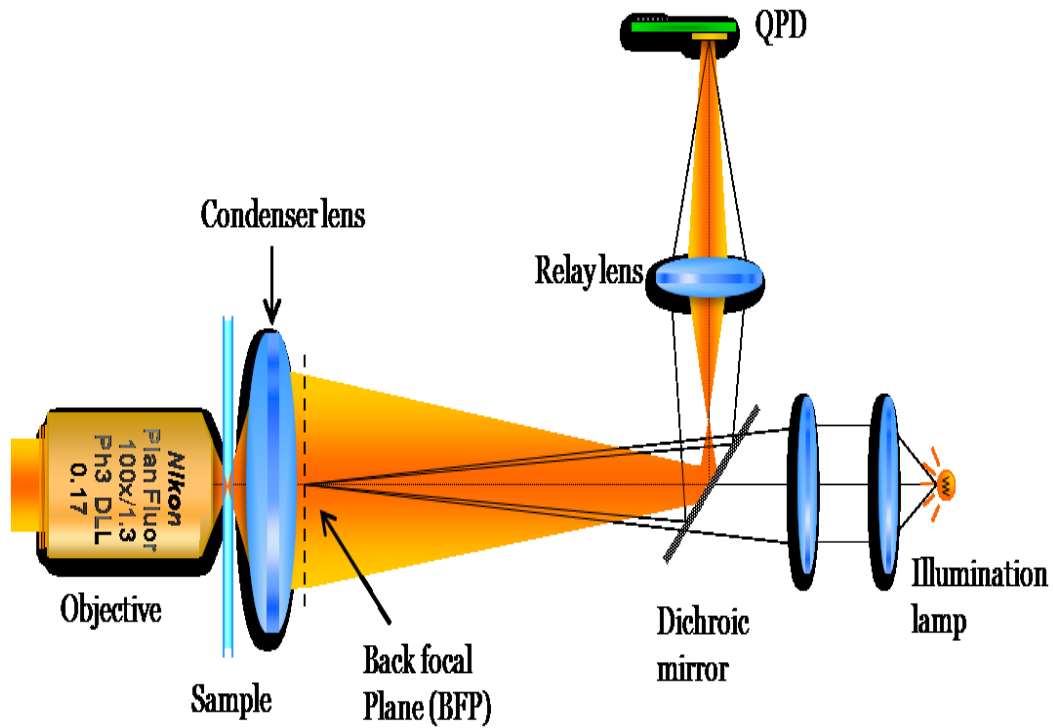
Figure 2.17. Back focal plane detection method (image from University of Barcelona at http://biopt.ub.edu/force-detection/back-focal-plane-interferometry)

Table 2.3

Summary of optical measurements of linear displacement

Name of the devices/techniques	Sub-catagory	Range	Resolution	Applications/Notes
Coherent	Homodyne	nm to µm	nm	Single light source, simple optical alignment.

	heterodyne	Å to µm	Å	Precise and complex alignment. Requires more than one light sources. Sensitive to both source and detector noise. Used in space doppler velocimeters.
	Video analysis	mm to µm	0.5 µm	Limited speed, Expensive hardware for computation. Used in monitoring bio samples such as bacteria, protein etc.
Incoherent	PSD	µm to cm	2 µm	Inexpensive, easy to use. Machine tool alignment, motion analysis, guidance system, targeting, beam alignment.
	QPD	Å to µm	0.1 Å	Low noise, fast, works with a wide range of optical sources. Robotic vision, 3-D TV, surveying, optical tracking, AFM.
Mixed	Polarization interferometry	pm to nm	1 pm	Measure position in terms of degree of polarization. More sensitive than most of the optical detection techniques.

Back focal plane	Å to nm	5.0 Å	Distance measurement of self-luminous objects. Lidar

2.8 Stiffness measurement

There are many ways to measure stiffness of nanostructures. Many of these methods involve a force calibration step. In atomic force microscopy, the cantilever is calibrated before measuring the force exerted by the sample on the cantilever [96-103]. The calibration is performed by measuring the thermal vibration of the cantilever tip, by using a reference cantilever, and by measuring the deflection by pressing the tip against a hard surface. Depending on the type of cantilever and samples, either one or a combination of these techniques is used. In optical trapping, trap stiffness is often calculated by measuring the thermal vibration of the trapped bead [104, 105].

There are three models to determine the stiffness of a micro-nanostructure i.e. 1) variance calculation, 2) measuring Brownian motion and 3) power spectral density. These three methods are equally applicable in the measurement of stiffness of an AFM cantilever tip, stiffness of a trap or the stiffness of a BOS structure.

2.8.1 Variance calculation

In this technique the cantilever beam (or trapped bead or BOS structure) is modeled as a spring. Average energy stored in a spring excited by random white (or Brownian) noise is

$$E = \frac{1}{2}k < x^2 > \tag{2.69}$$

where <.> is the expectation operator defined as

$$< X > = \sum_{i=1}^{k} x_i p_i$$

where x_i is the ith sample outcome of random variable X and p_i is the probability of the ith outcome. For white noise, p_i is identical for each outcome. According to the equipartition theorem, the average thermal energy equals the random vibration energy of the object

$$E = \frac{1}{2} k_b T \tag{2.70}$$

where k_b is the Boltzman constant and T is the temperature. Equating eqs. 2.57 and 2.58, gives the spring constant or stiffness of the object as

$$k = \frac{<x^2>}{k_b T} \tag{2.71}$$

The stiffness of the object is determined from the mean square average of the time series of position in eq. 2.71.

2.8.2 Measuring Brownian motion

The second model is to measure the power spectral density of the Brownian motion of the structure. This model is for the case of overdamping (Sec. 2.3). If the structure is small, inertial forces are ignorable compared to hydrodynamic forces of the system. These structures can be modeled as low velocity, low Reynolds number object in the stokes drag regime. The system can be considered as a massless damped oscillator in which the prime driving force is the Brownian motion. This model is described by the differential equation

$$\beta \dot{x}(t) + kx(t) = F(t) \tag{2.72}$$

48

where β is the drag coefficient of the structure is

$$\beta = 6\pi\eta r \tag{2.73}$$

where r is the radius of the structure, η is the viscosity of the surrounding fluid and $F(t)$ is the white source with a Fourier spectrum power

$$\left|\tilde{F}(f)\right|^2 = 4\beta k_b T \tag{2.74}$$

The Fourier transform of eq. 2.72 is

$$2\pi\beta \left(\frac{k}{2\pi\beta} - jf\right)\tilde{x}(f) = \tilde{F}(f) \tag{2.75}$$

This gives and displacement power spectral density of

$$|\tilde{x}(f)|^2 = \frac{k_b T}{\pi^2 \beta \left[\left(\frac{k}{2\pi\beta}\right)^2 + f^2\right]} \tag{2.76}$$

Eq. 2.76 is a Lorentzian function. It has a corner frequency $f_c = k/2\pi\beta$ giving stiffness

$$k = 2\pi\beta f_c \tag{2.77}$$

2.8.3 Power spectral density

Power spectral density of a time series x(t) is defined as

$$S_{xx} = \lim_{T\to\infty} E[|\hat{x}(\omega)|^2] \tag{2.78}$$

Where $\hat{x}(\omega)$ is the Fourier Transform of $x(t)$. For discrete time signals it can also be expressed as

$$S_{xx} = \lim_{N\to\infty} E\left\{\frac{1}{N}\left|\sum_{t=1}^{N} x(t)e^{-j\omega t}\right|^2\right\} \tag{2.79}$$

The relationship between the stiffness of a vibrating nanomechanical structure and the amplitude of the vibration is similar whether the object is a trapped bead, micromachined cantilever or a BOS structure. Fig 2.18 shows the relative power-frequency relationship of

a 2.1 μm diameter polystyrene particle trapped in the same medium for different laser trapping powers[106]. The figure shows that, the corner frequency of the trap increases, and amplitude of vibration decreases with increasing laser power, which corresponds to stiffening of the trap (See eqs. 2.76, 2.77).
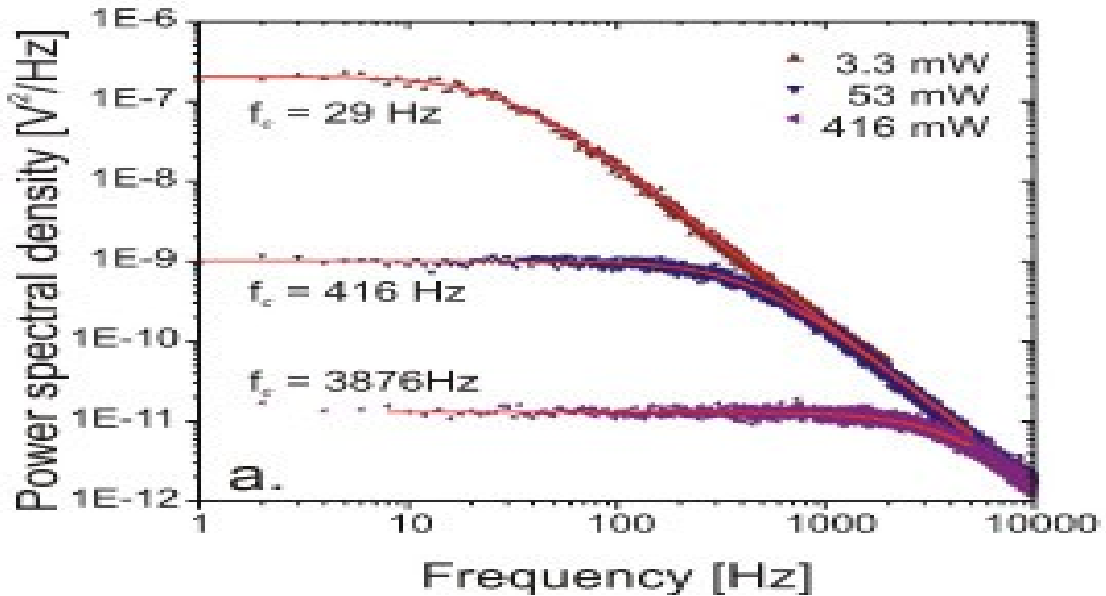
Figure 2.18. Power spectral densities for a laser trap at three trap stiffnesses as measured by QPD. Plot from [106]

2.9 Gaussian beam characterization

The waist diameter of the laser beam affects QPD displacement measurement sensitivity (Sec.3.5). This section reviews laser beam profiling. There are many methods available to measure different beam parameters. Yoshida and Asakura[107] placed a thin wire of known diameter to cut-off some of the light from the beam and measured the beam waist by taking the ratio of the powers in the presence and absence of the wire. This method works well if the beam diameter is larger than the diameter of the wire. It is difficult to

implement in optical trapping and single molecule tracking, where the laser beam is focused below one micron. Other methods includes using a slit developed by Gupta and Bhargava[108], using a CCD camera by Riza and Jorgesen[109], and a chopper technique by Ortega et al.[110].

The method of beam profiling chosen for this study is the knife edge method[111]. The blade edge of a sharp knife is scanned transversely across the beam path while measuring the transmitted power, which gives a function of power vs. position. In the original knife-edge method, the derivative of the power vs position curve gives the Gaussian profile of the beam, from which the waist diameter is calculated. Since the derivative of the error function is a Gaussian, it is also possible (as done in this study) to fit the power-position curve with an error function, from which the Gaussian shape and waist diameter is then found analytically.

2.10 Conclusion

The main results from this chapter that will be applied in subsequent chapters are

- The Lorentzian spectral model (eq. 2.8) will be fit to the thermal vibration spectra of the structures studied in chapters 5 and 6.

- Models of noise contributions that are expected to arise from the QPD photodetection electronics are described.

- A QPD has been selected for measuring the thermal vibration spectra in the subsequent chapters.

CHAPTER 3
INSTRUMENTS AND METHODS

This chapter describes the how the optical vibrometer is assembled, characterized, and calibrated, and how the test samples are prepared and mounted in the vibrometer.

3.1 Vibrometer layout

The vibrometer (Fig. 3.1) measures the vibrations of structures placed in the sample plane. A frequency, temperature and power stabilized, single transverse and longitudinal mode semiconductor laser (New Focus Velocity 6316) is regulated at a wavelength of 850 nm (see Table 3.1). The laser is used either in a constant power mode, or its power is
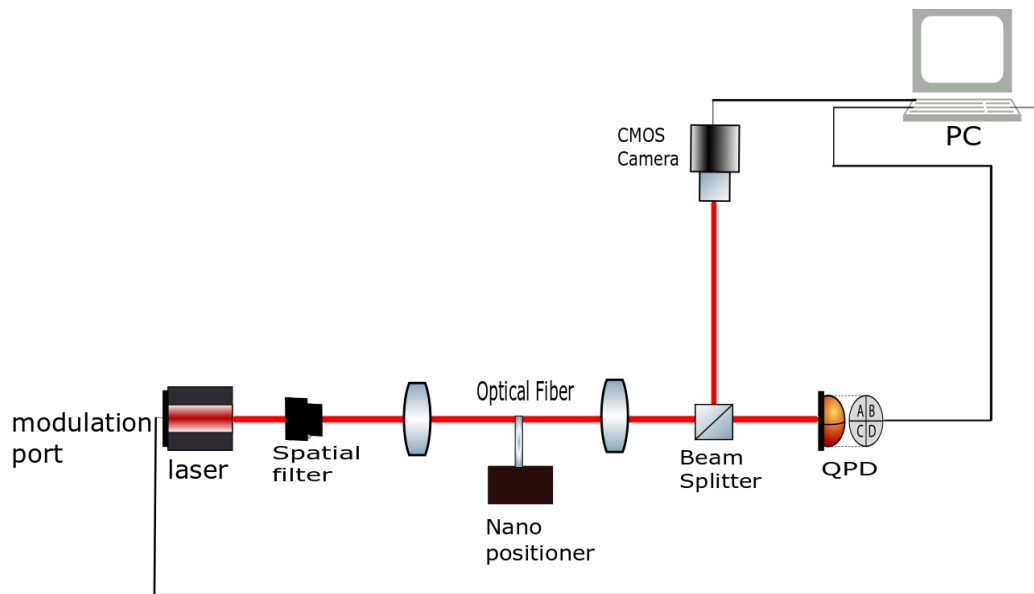
Figure 3.1. Optical vibrometer with tip of cantilevered fiber positioned in the laser beam at the sample plane

modulated with external voltage applied to the modulation input. The laser appears to produce the least noise in vibrometer measurements when its output power is 3.0- 3.8 mW. The laser beam passes through a spatial filter (Newport 910A), producing a nearly ideal Gaussian beam. A 20X microscope objective (L1) after the spatial filter focuses the laser beam to a beam diameter of 6.05 µm at waist. The light from the sample is collected and collimated by a second 20X microscope objective (L2). The beam is centered on the QPD (First Sensor QP10-6SD2) when no sample is present, and the beam is displaced from the center by refraction from the sample. The refraction angle and beam displacement vary as the object moves transversely to the beam. The manufacturer recommended diameter of the spot that maximizes position accuracy is 0.5 mm. The beam splitter splits the image of the spot between the QPD and the camera. The image of the spot is used to simultaneously align the spot on the QPD and sample. The sample is positioned using a three-axis piezo nanopositioning stage (Mad City Labs Nano-2D200). It has less than 1 nm position drift and hysteresis.

Table 3.1. Preferred laser settings used in the vibrometer

Parameter	Value
Wavelength (nm)	850
Temperature (°C)	70
Laser Power (mW)	3.0-3.8
Laser spot size at sample (µm)	10-125 (same diameter as the sample)
Laser spot size at QPD (mm)	0.5

3.2 Supporting instruments

3.2.1 Microscope

An Olympus IX-71 inverted light microscope that can perform both transmission and reflection imaging is used to image and measure dimensions of the BOS structures. All samples are imaged with air microscope objectives that cover 10-100X magnifications (with numerical apertures up to 0.95). The microscope has a Prior Scientific X-Y-Z motorized stage. A Pixelink video camera attached to the microscope collects still and video images. A Slidebook microscope interface controls scanning and image collection, and other operations, including active stabilization of the object position in 3D. Slidebook also includes tools for making dimensional measurements, stray light removal, sharpening and contrast control of collected images. These features are used to measure the dimensions of the micron scale structures studied in Chapters 5-6.

3.2.2 Scanning Electron Microscope

The diameter of the BOS structure can be between 3-25 microns and the diameter of the string can be as small as 30 nanometers. A scanning electron microscope (SEM) is used to measure dimensions below the resolution limit of the optical microscope (~300 nm for the 0.95 NA objective). The SEM (Zeiss Supra 35VP) has an image resolution of 1.2 nm. Since the samples are non-conductive, the samples are sputter coated with a conductive film (Au/Pd). In addition to increasing the contrast of the samples, the conductive coating shields polymer materials from damaging heating and bond scission.

3.2.3 Optical chopper

An optical chopper (Palo Alto Research, Model 300) is used in measurements of NEP of the QPD (sec.2.5.1). The chopping frequency can be set from 4 to 6,400 Hz by

selecting specific combinations of motor rotational speed and the number of slits around the circumference of the chopping wheel.

3.2.4 Signal generator and oscilloscope

A waveform generator (Tektronix AFG 3022) is used both to modulate the laser and drive a piezoelectric actuator (SM SPK2724300) that vibrates the samples. The pulse output is used for impulse response measurements of the QPD. Frequency sweeping is used to measure the frequency response of the vibrometer. Fixed sinusoidal frequencies and narrow band sweeps are used to excite the samples near around their resonance frequencies. An Oscilloscope (Tektronix TDS 2022B) monitors the excitation signals.

3.3 Sample preparation
3.3.1 Polymer solution preparation

BOS structures are formed from a starting solution of 485 mg of deionized water and 15 mg of polyethylene oxide (4 MDa PEO from Sigma-Aldrich) resulting in a 3 wt% solution. The weights are measured with a precision of 100 µg on a Mettler AJ100 balance. The solution requires mixing to ensure that the PEO dissolves. The mixture is stirred at 1000 rpm for 1 min, then at 3000 rpm for 2 min with a vortex mixer (Thermo Scientific M37615). The solution then stands for 48-72 hr to allow the PEO to fully dissolve and for air bubbles to come out of the solution.

3.3.2 BOS fabrication

BOS fibers are formed by capillary-force self-assembly that is initiated by macroscale hand brushing the PEO solution over an array of micropillars (Fig. 3.2)[112].

A 10-20 μg drop (estimated from image analysis of microscope images) of the PEO solution is deposited on the edge of an applicator (a glass coverslip) and then the applicator is drawn over the pillar array as shown in Fig. 3.2. Brush-on speeds between 3.33-5.00 mm/s were found to most often produce the BOS structures of desired bead dimensions (between 10-20 μm. (See Table 3.2).

Cleanroom-fabricated glass micropillar arrays are used as the supporting structures. The pillar center-to-center spacing (pitch) is 1.0 mm with a 0.5 mm gap.

The optical path needs to be obstruction free to maximize the optical signal strength on the QPD. A pillar array having several rows past a BOS fiber can block and rescatter the laser beam. Instead a pillar array consisting of two columns of pillars is fabricated by separating two columns of micro-pillars from the full array with a diamond dicing saw. Then the pillars are glued on a glass slide using Super Glue.

Three kinds of structures form during the fabrication process: (1) BOS with a single bead, (2) BOS with multiple beads, and (3) cylindrical fibers with no beads. No one single structure forms predictably. This is shown in Table 3.3 where a single beaded BOS, the target structure for BOS studies in chapter 6, forms 14 times out of 1000 attempts (at a brushing speed of 3.33-5.00 mm/s).

Table 3.2

Distribution of structures formed from 1000 brush-on attempt

(50 brushes over an array having 20 sites for fiber formation)

Structure type	Bead diameter (μm)	Number
Single bead	1-5	2
	6-10	6

	11-20	6
Multi-beads	NA	73
Only fibers	NA	79
No structures	NA	834
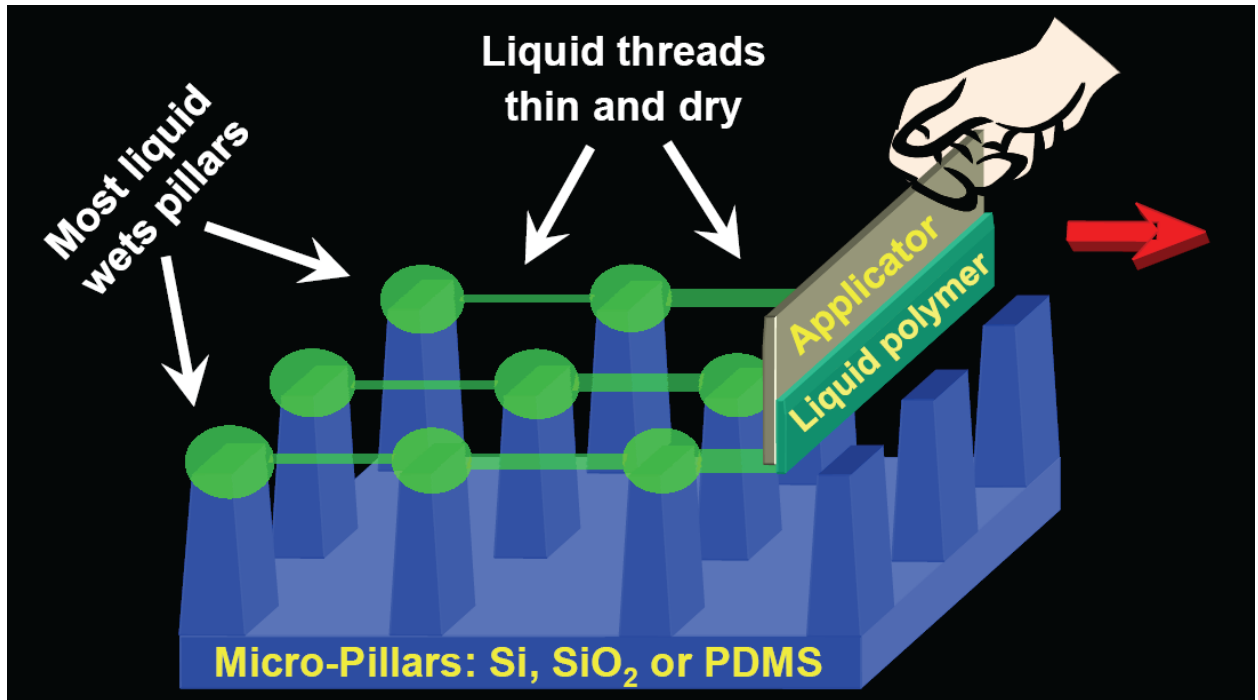
Figure 3.2. BOS fabrication by the brush-on method. Schematic from [112]

3.3.3 BOS solidification

The BOS fibers, because they are fabricated from a 3 wt% polymer solution, solidify as the water evaporates from them. After brush-on, the micropillar array is viewed under the microscope. Heating caused by the microscope lamp dramatically increases evaporation rate. Room temperature in the lab is 22 °C, while the temperature under the microscope is 31 °C. Evaporation rate can be adjusted by controlling temperature, ambient humidity and drying time. The rate of evaporation from PEO droplet on solid surfaces is influenced by molecular weight of the polymer, initial concentration[113-115], size of the

droplet[116, 117], ambient temperature, relative humidity[118-120], pressure, contact angle[120, 121] on the surface, and time. In Sec. 6.4 evaporation is considered as a source of drift of the thermal vibration spectra (see Sec 6.4). In this study however none of these parameters were varied to control the solidification.

3.4 Vibrometer characterization

A numerical simulation (Appendix C) shows that the vibration amplitudes of the BOS and cantilevered fibers are expected to be on the order of 1 Å. Vibration amplitudes at this level require a high sensitivity vibration sensor. A Thorlabs QPD (PDQ80A) and First Sensor QPD (QP10-6SD2) are evaluated for this purpose. Noise equivalent power (NEP), dynamic range, impulse response, and linearity are evaluated.

3.4.1 Noise Equivalent Power of the QPD

Noise equivalent power (NEP) (Sec 2.6.1.4) is measured using the setup in Fig. 3.3. The photodetector gives an absolute measurement of the optical power in the laser beam. The power on the photodetector is related to the power on the QPD by the splitting ratio (1:99) of the beam splitter. The measurement is done in a dark room and the photodetector is zeroed to offset dark current. Then the chopper is turned on, and the modulated QPD signal is captured by an A/D convertor (National Instruments PXI 4462) and recorded on a PC using LabView. The modulated signal is Fourier Transformed showing peaks corresponding to the harmonics of the square wave modulation. The laser power is reduced by adding neutral density filters (NDF) until the peak of the fundamental frequency of the chopped signal is at the level of the background noise.

Sensing characteristics of the QPDs are presented in Table 3.3 The measured NEP of the First Sensor QPD is within 5% of the value published in the data sheet by manufacturer.

Table 3.3

Characteristics of Thorlabs and First Sensor QPDs

Parameter	Thorlabs	First Sensor
Dark voltage (mV DC)	21	2
Drift with laser on (μV)	-300 to 400	-100 to 100
Noise level in dark (dB)[*]	-128.4	-141.1
Noise level with laser spot centered (dB)*	-128.4	-141.2
NEP (pW)	35.4	0.212
Detection sensitivity (Å)	0.42	0.1

*dB with respect to 1.0 V. See Appendix A
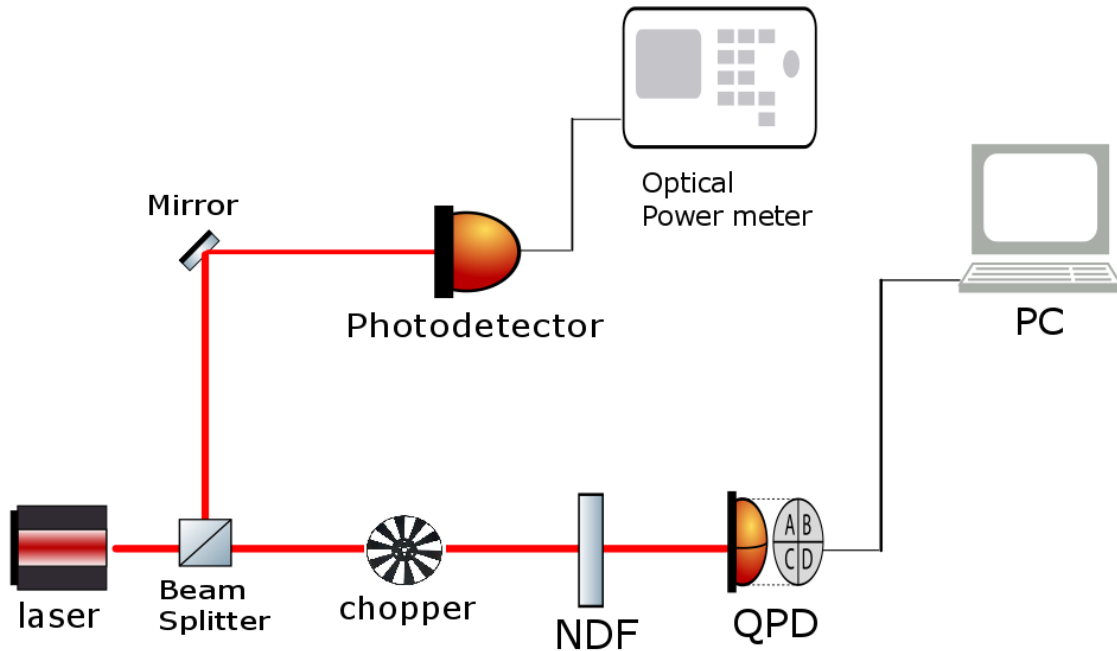
Figure 3.3. NEP measurement setup

59

3.4.2 Modeling the Vibrometer as a linear system.

A system is linear if it obeys the properties of homogeneity (scaling) and superposition (additivity)[122]. A linear time invariant (LTI) system also obeys time invariance where time invariance is for system $y(t)=h[x(t)]$ the property that shifts of t_0 of the input signal, shifts the output by t_0 to $y(t- t_0)=h[x(t-t_0)]$. Homogeneity ensures that the output signal is amplified/attenuated by the same factor as the input signal $Ay(t)=h[Ax(t)]$. This property is relevant to the vibrometer which has multiple devices that attenuate (beam splitter, spatial filter), amplify (op-amp in QPD driver circuitry), sample and quantize (A/D converter). The superposition property ensures that the output is identical when multiple inputs are added together in different orders. This property is relevant to the vibrometer in that the system is driven by applying various excitation signals both at the input to the laser modulation port and to the piezoelectric plate.

The vibrometer response is characterized for impulse, swept frequency and white noise inputs.

3.4.2.1 Impulse frequency-response analysis (IFRA)

For a linear time invariant (LTI) system with impulse response $h(t)$ and input $x(t)$, the output is

$$y(t) = \int_{-\infty}^{\infty} h(\tau)x(t - \tau)d\tau \qquad (3.1)$$

If the input $x(t) = \exp(j2\pi ft)$, then

$$y(t) = \int_{-\infty}^{\infty} h(\tau) \exp\big(j2\pi f(t - \tau)\big) d\tau$$

$$= \exp(j2\pi ft) \int_{-\infty}^{\infty} h(\tau) \exp(-j2\pi f\tau) \, d\tau$$

$$= H(f) \exp(j2\pi ft) \tag{3.2}$$

Where *H(f)*, the transfer function, is the Fourier Transform of the impulse response.

The frequency response of the vibrometer is measured by inputting an impulse to the amplitude modulation port of the laser and detecting the beam with the QPD and recording the QPD signal on the PC. The transfer function is then found from the Fourier Transform of the recorded signal.

3.4.2.2 Swept frequency response analysis

The bandwidth of the sweep is preselected. Then the sinusoidal swept is input to the laser and the QPD output is recorded on the PC. The sweep frequency can be linear or exponential. An exponential sweep signal $S(n)$ start from ω_1 to ω_2 over T seconds is expressed as[123]

$$S(n) = sin\left[K\left(e^{T/L} - 1\right)\right] \tag{3.3}$$

Where $K = \frac{\omega_1 T}{ln\frac{\omega_2}{\omega_1}}$ and $L = \frac{T}{ln\frac{\omega_2}{\omega_1}}$. The time delay Δt_n between any sample n_0 and a later point with instantaneous frequency N times larger than that instantaneous frequency at $S(n)$ is constant and given by

$$\Delta t_n = T\frac{\ln(N)}{ln\frac{\omega_2}{\omega_1}} \tag{3.4}$$

The resolution of the sweep frequency depends on total sweep time T and the bandwidth $\Delta\omega$ of the measurement. The resolution of the sweep is proportional to the total sweep time

and inversely proportional to the bandwidth. A waveform generator (Tektronix AFG 3022) generates a sinusoidal sweep signal over the range 1.0 Hz to 2.499 KHz.

3.4.2.3 White noise test

White noise is a random signal having equal average intensity at all frequencies. White noise is a random process $Z(t)$ such that $Z(t)$ is independent and uncorrelated with $Z(t - s)$ for s not equal to t, or [124]

$$E[Z(t)Z(s)] = \delta(t - s) \tag{3.5}$$

Where $\delta(t)$ is the Dirac delta function. I built a white noise generator for measurements of the frequency response of the vibrometer. The A/D converter samples the QPD as fast as 100 KHz. The bandwidth of the noise generator is limited to 10 KHz (because the resonance frequency of all the structures in this study are less than 10 kHz). I also built a 5th order Butterworth filter with cutoff frequencies of 1.0 KHz and 10.0 KHz. Band limited white noise from the cascade of the white noise generator and the band pass filter is used as the input to the laser for frequency response and dynamic range measurement of the QPD.

3.5 Measurement of QPD sensitivity

The signals X_{diff} and Y_{diff}, from the four discrete photodiodes of QPD (see Sec. 2.5.1) give lateral position of the spot. A scaling or sensitivity factor (S) is needed to convert the voltage signals X_{diff}, and Y_{diff} into displacement of the sample. Because the sensitivity is tied to the amount of refraction by the sample, the sensitivity depends on the object shape and the location of the object in the laser footprint. A calibration method is used to determine the sensitivity of each sample measured by the vibrometer. The

sensitivity is measured after allowing the laser output power to stabilize (usually within 3-5 min after turning it on). The sample is placed on a sample mount that is attached to a nanopositioner for fine positioning and scanning of the sample (Fig. 3.4). This is mounted on top of a manual 3D stage., for coarse positioning of the sample. The video camera (see Fig. 3.1) aids in the coarse alignment step. Then, the sample is scanned by the nanopositioner in x or y while recording X_{diff} or Y_{diff}. Sensitivity S is then determined (eq. 3.7) from the scan distance

$$\Delta x = a + b \qquad (3.6)$$
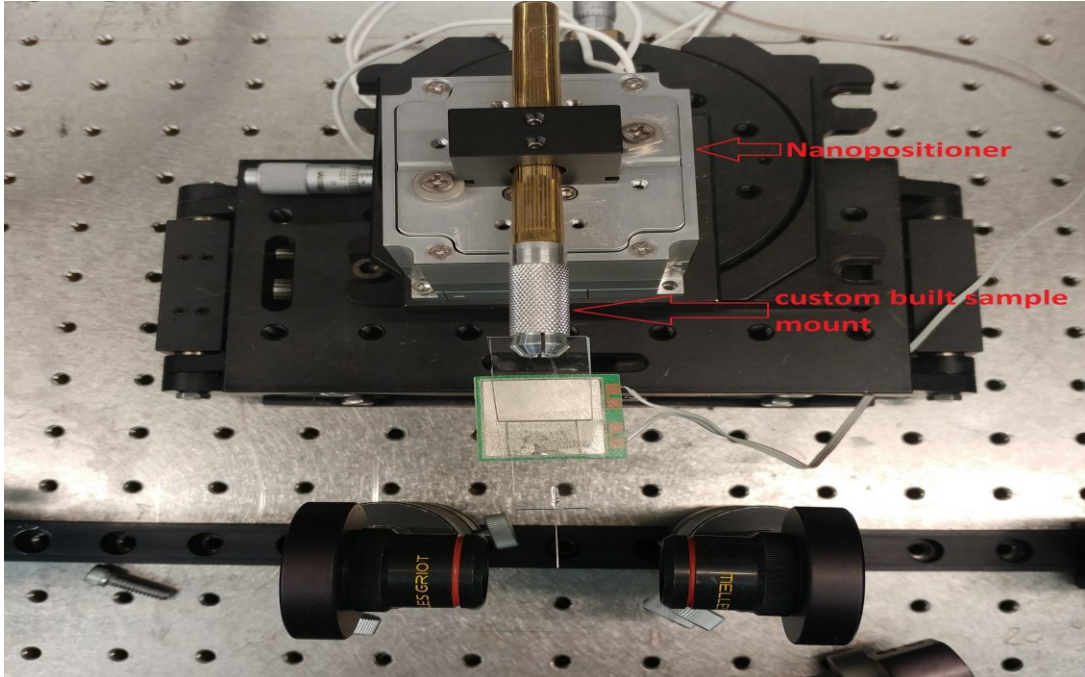
Figure 3.4. Sample mount shown with the sample (a glass fiber) placed near the beam focus that is centered between the two objectives.

where a is sample diameter, b is the diameter the laser spot on the sample, and the corresponding QPD voltage response ΔV in the linear region where the sensitivity is then

$$S = \frac{\Delta x}{\Delta V} \qquad (3.7)$$

The measurement is repeated several times at different axial locations near the focal point to determine the position of maximum sensitivity.

3.6 Estimates of the vibration dynamics of BOS fibers

The vibration of single bead BOS fibers is modeled as a fixed-fixed cantilever with a central mass (see Table 2.1). This is simulated in Appendix C and a summary of these results is in Table 3.4. When the BOS fiber first forms it contains a large amount of water, which decreases with time due to evaporation and which leads to corresponding changes in the frequency and amplitude.

Table 3.4

Estimated ranges of BOS mechanical properties

Measured dimensions		Simulated vibration parameters			
Bead diameter (μm)	String diameter (nm)	Resonance frequency (Hz)	Amplitude (nm)	Stiffness (μN/m)	Q
10-25	200-800	12-740	16.9-273	0.055-14.33	0.1-2.7

The model of BOS structure with a single bead (20 μm diameter), located exactly middle of a 300 nm diameter string has a thermal vibrational amplitude of 29.17 nm at 155 Hz resonance frequency. A 50% mass loss from the bead due to evaporation would move the resonance frequency to 219 Hz (eq. 2.68), assuming the diameter and string mass are unchanged with evaporation. The vibrometer can easily detect this 64 Hz of frequency change. Both the bead and string diameter varies during the fabrication process depending on amount of starting polymer solution, room humidity and speed of brushing. Stiffness of

64

the structure determines the amplitude and the frequency of the vibration. Note that, stiffness depends on the 4th power of the diameter of the string. A change in the diameter of the string from 200 nm to 800 nm increases the stiffness of the structure from 0.055 μN/m to 14.33 μN/m. The resonance frequency of the vibration would be in the range of 12 Hz to 756 Hz for a BOS with a bead diameter between 10 μm and 25 μm (with string diameter between 200~800 nm). Amplitude of the vibration for the BOS structures having the dimensions in these range would be in the range of 4.1 nm and 65 nm.

A more detailed analysis of the vibrational parameters for BOS structures are presented in Appendix C.

3.7 Design of fiber cantilevers that have similar vibration dynamics as BOS fibers

Transparent cylinders have well defined light scattering properties. For this reason, glass optical microfibers, that have diameters that are similar to the BOS bead diameters, are selected for the first objects to be measured with the vibrometer. Cantilevered fibers of sufficient length can have bending stiffnesses in the same range as expected for BOS fibers (Appendix C). From eq. 2.7 a 20 mm long, 30 μm diameter glass cantilever vibrates at a resonance of 52 Hz with a thermal amplitude of 2.06 nm while a 15 mm long fiber vibrates at 92 Hz with an amplitude of 1.33 nm

CHAPTER 4
DETECTION LIMIT AND POSITION SENSITIVITY OF THE OPTICAL VIBROMETER

4.1 Introduction

The thermal vibration amplitudes of interest in this study are in the range of angstroms to nanometers. Structures vibrating by this amount deflect the laser beam by a similar amount. Increasing the distance between the sample and the detector increases position sensitivity, but reduces the power detected because of overfilling the detector. Therefore, there is a tradeoff between measuring position and the limit of power detection. In this chapter the vibrometer position measurement is characterized and optimized in terms of these two competing parameters. The chapter also represents a comparison of the performance of this system to other reported position detectors.

4.2 Measurement of the Noise equivalent optical power

A square wave with period $T=2\pi$, amplitude $A=1$, as shown in figure 4.1 can be expressed as

$$f(x) = \begin{cases} 1, & \text{for} \quad 0 < t < \pi \\ 0, & \text{for} -\pi < t < 0 \end{cases} \tag{4.1}$$
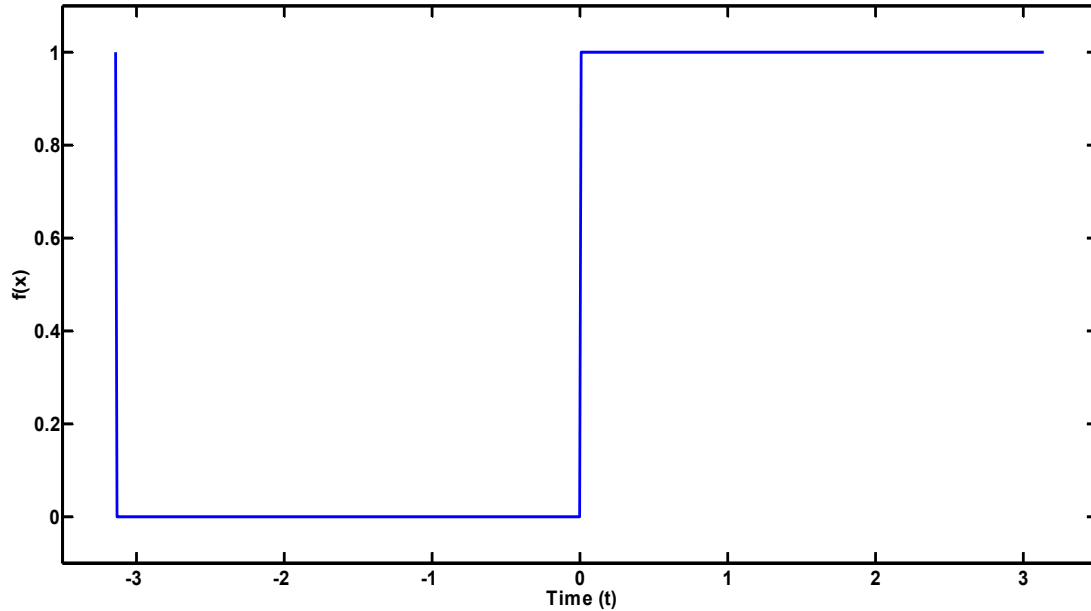
Figure 4.1. One period of a square wave

The Fourier series of this periodic waveform can be represented as a summation of infinite number of sinusoidal signals. The mathematical representation in trigonometric form is

$$f(x) = a_0 + \sum_{n=1}^{\infty}(a_n \cos(n\omega t) + (b_n \sin(n\omega t)) \qquad (4.2)$$

Where a_0, a_n, and b_b are coefficients of Fourier series and represent average/mean/DC amplitude, amplitudes of even components, and amplitudes of odd components respectively. For a duty cycle of 50% the Fourier coefficients are

$$a_0 = \frac{1}{2\pi}\int_{-\pi}^{\pi} f(x)dx = 0.5$$

And for n≥1, coefficient of the even terms is

67

$$a_n = \frac{1}{\pi} \int_{-\pi}^{\pi} f(x) \cos(nx) \, dx = 0$$

And the coefficient of the odd terms is

$$b_n = \frac{1}{\pi} \int_{-\pi}^{\pi} f(x) \sin(nx) \, dx$$

$$= \begin{cases} 0 & \text{if n is even} \\ \dfrac{2}{n\pi} & \text{if n is odd} \end{cases}$$

The resulting Fourier series can be expressed as-

$$f(x) = \frac{1}{2} + \frac{2}{\pi}\sin(x) + \frac{2}{3\pi}\sin(3x) + \frac{2}{5\pi}\sin(5x) \dots \dots \dots \dots \quad (4.3)$$
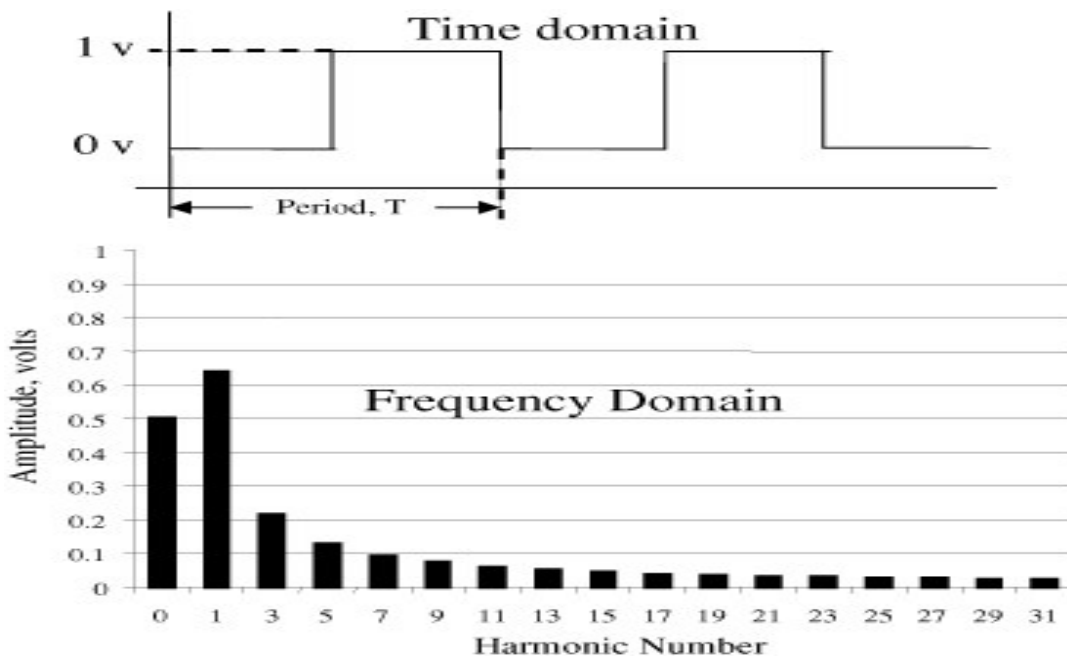
Figure 4.2. A square wave and distribution of its voltage among DC and odd harmonics (Sine coefficients in Eq. 4.2) Image from chapter 2 of Signal and Power Integrity, 2nd edition

The above equation demonstrates the distribution of amplitudes of a square wave among

its sinusoidal components.

Noise equivalent power of two different QPDs are measured by modulating the intensity of the laser beam with an optical chopper. The chopper produced a near ideal square wave with 50% duty cycle. The laser output is set at 3 mW and less than 10% of this power is transmitted through the spatial filter. The splitter passes 99% of the remaining laser light to the QPD and 1% to the reference photodetector. The photodetector is connected to an optical power meter, which is read by the host PC. Power on the QPD is calculated from the ratio of beam splitter and the reading from the optical power meter (Sec. 3.4.1). The chopper is placed after the beam splitter and before the QPD (Fig. 3.3). The frequency of the chopper is set to 800 Hz and the modulated light signal is collected by QPD. The output is a square wave as shown in Fig. 4.2. Once the chopper speed stabilizes, the data is recorded, and a neutral density filter is placed in the beam path to lower the optical power to the QPD. The process is repeated until the peak of the fundamental
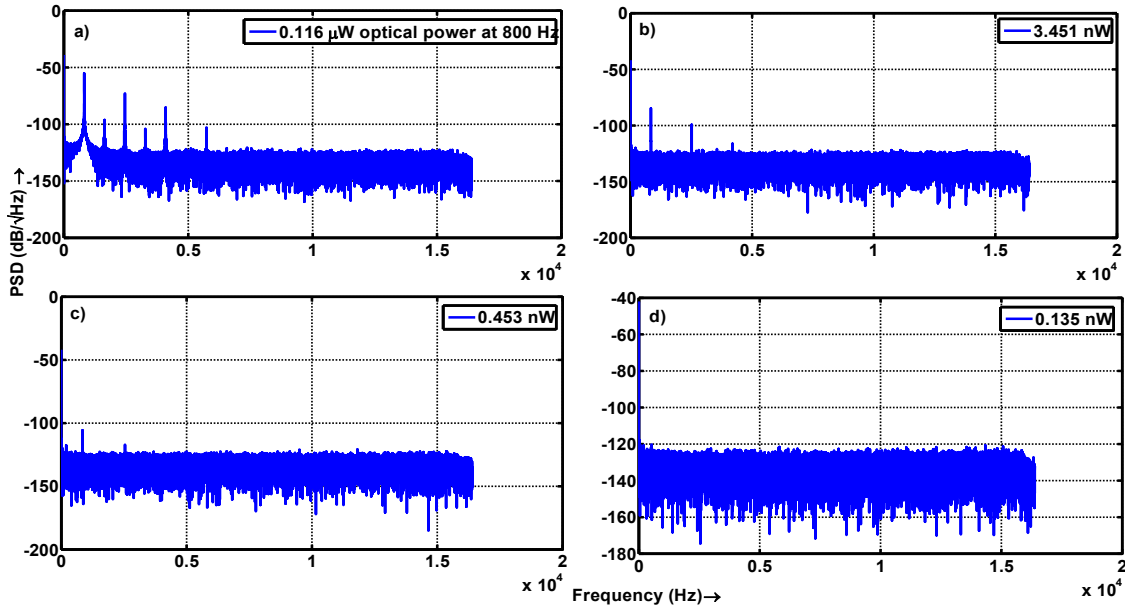
Figure 4.3. Power spectra of the chopped laser beam incident on the Thorlabs QPD. a-d) Changes in spectral response of the SUM signal as the incident optical power at 800 Hz is reduced to 0.116 µW, 3.451 nW, 0.453 nW, and 0.135 nW

(at 800 Hz) is at the same level as the noise.

NEP is calculated by monitoring the peak of only the fundamental frequency (at 800 Hz) of the SUM signal when the peak is equal to the electronic background noise. Note that, the OPD output voltage is proportional to the incident laser power which makes the coefficients a_n, b_n, and a_0 (eq. 4.2) of chopped SUM signal proportional to the incident optical power. In Fig. 4.3a total power incident on the Thorlabs QPD is 0.183 µW which makes the power at the peak of the fundamental as 0.116 µW (i.e. 63.66 %. See Fig. 4.2b). Similarly, the peak is 0.135 nW when the incident optical power at QPD is reduced to 0.213 nW (Fig. 4.3d) and this 0.213 nW which is the NEP of the Thorlabs QPD. Repeating the same measurements using the First Sensor QPD gives an NEP of 0.212 fW.

Before the measurement of the modulated signal is conducted, the dark power of both QPDs is determined. The dark power is measured by zeroing the power meter and then reading the power output of the QPDs in the dark. The dark power for the Thorlabs QPD is measured at 40 pW. However, the dark power measurement of the First Sensor was unsuccessful because of the lack of sensitivity of the optical power meter used in the study. The lowest detectable power by the optical power meter is 0.05 pW and the First Sensor QPD output was measured at 0.0 W in the dark. The power meter shows a 0.0 W because the dark power generated by the First Sensor QPD was less than 0.05 pW and the power meter rounds the number to 0.0W. Dark power is subtracted from the calculated NEP to get the actual NEP. Table 4.1 compares the results from the NEP measurements of both QPDs. Because the NEP of the First Sensor QPD is 6 orders lower than the NEP of the Thorlab QPD, all the remaining experiments after this section is conducted by using the First Sensor QPD.

Table 4.1. Comparison of NEPs between Thorlabs and First Sensor QPDs

QPD manufacturer	Dark Power (pW)	Measured NEP (fW)	NEP provided by manufacturer (fW)
Thorlabs	40	95596	Not provided
First Sensor	<0.05	0.212	0.18

4.3 Pulsed spectral response of the First Sensor QPD

The frequency response of the vibrometer is measured by the technique described in section 3.4.2.1. A rectangular pulse (see Table 4.2) modulates the laser which is detected by the First Sensor QPD. The impulse has a rise and fall time of 18.0 ns. That is fast enough

71

to consider the signal as an impulse. Fig. 4.4a-b shows the input to the laser and SUM output of the QPD respectively. The response (power spectra) of the vibrometer due to the impulse is in
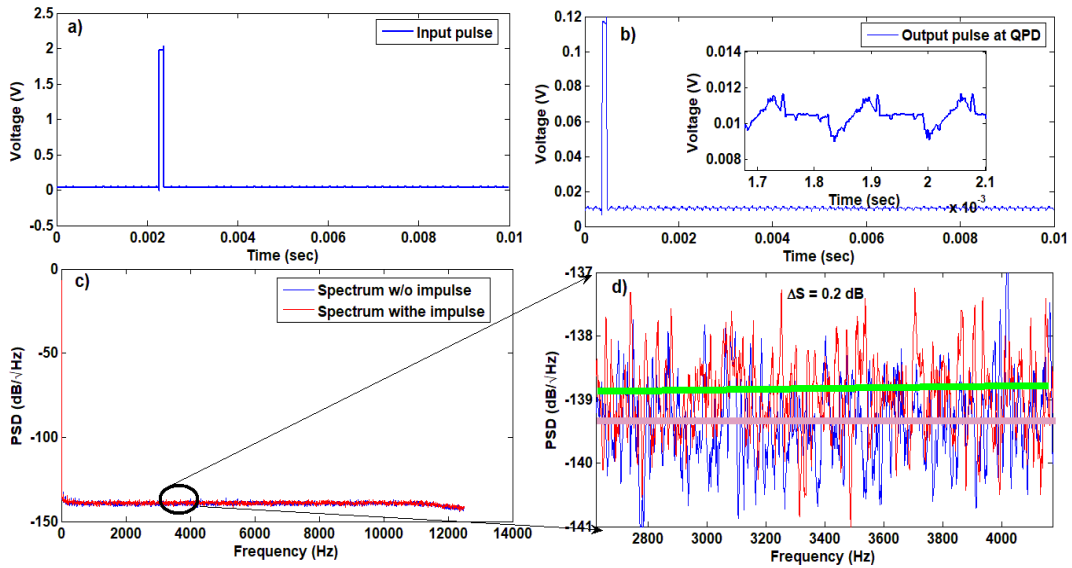
Figure 4.4. Impulse frequency response analysis of First sensor QPD. a) Impulse applied to the amplitude modulation port of the laser. b) Signal detected by the QPD at SUM output. c) Change in the spectral response of the SUM signal due to the pulse. d) Close up view of the spectral response.

figs.4.4c-d. The blue curves in these figures indicate the spectrum of the QPD SUM signal without modulation and the red ones are pulse modulated response. The average of the spectrum (straight lines in Fig. 4.4) only increases by 0.2 dB due to the pulse.

Table 4.2. Parameters of impulse signal

Parameters	Value	Change in spectral level
Amplitude (V)	2.0	
Width (µs)	100.0	
Frequency (mHz)	100.0	0.2 dB
Rise time (ns)	18.0	

Fall time (ns)	18.0	

4.4 Swept frequency response of the First Sensor QPD
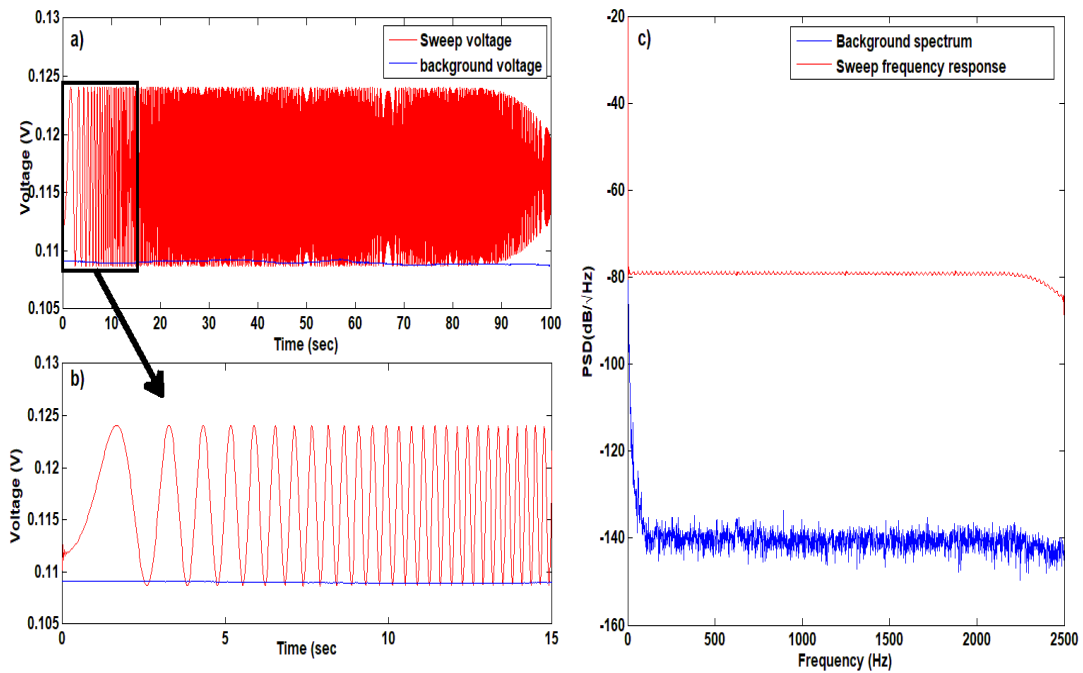
Figure 4.5. Swept frequency response of the First Sensor QPD. a) Changes in SUM signal of the QPD with sweep signal. b) Close up view of sweep and background SUM signal. c) Noise spectrum and the swept frequency response (SFR)

Fig. 4.5 shows a swept signal (Table 4.3) and the frequency response (Sec. 3.4.2.2) of the First Sensor QPD.

The blue curves in Fig. 4.5a-b represent the SUM signal of the QPD when the laser is not modulated, and the red curve is when the laser is modulated. Figure 4.5c is the

power spectrum of the signals in Fig. 4.5a-b. The blue spectrum, which is the Fourier

Transform of the SUM signal without any modulation, increases by 61 dB due to the

swept frequency modulation.

Table 4.3. Parameters of SFRA test

Parameters	Value	Spectral level Change
Amplitude (V)	2.0	
Offset (V)	1.0	21.0 dB
Frequency span (Hz)	1-2500	
Time span (s)	100	

4.5 White noise response of the First Sensor QPD
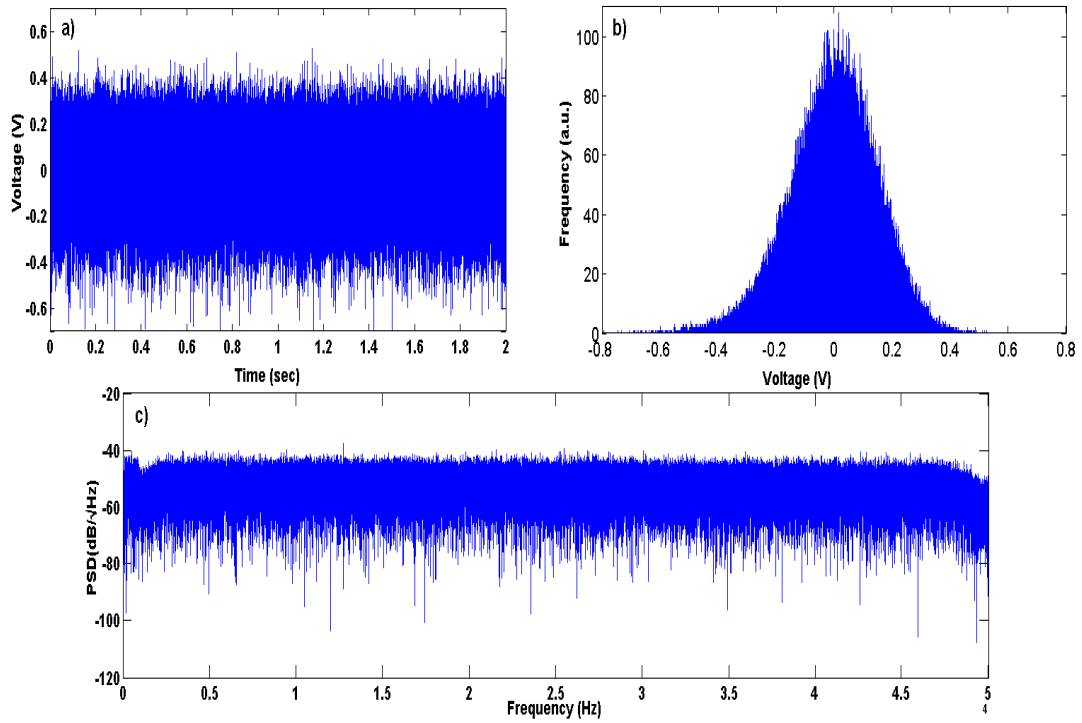
Figure 4.6. Characteristics of white noise generator. a) Output voltage of the generator. b) Histogram of the output voltage. c) Power spectral density of the white noise.
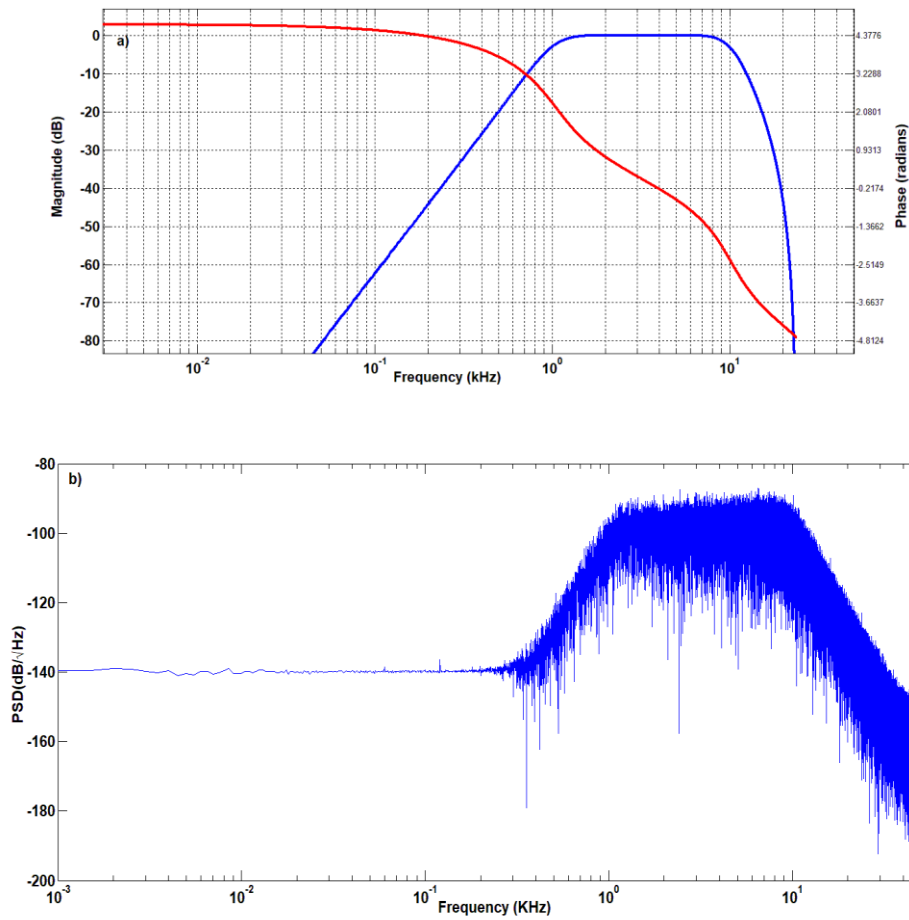
Figure 4.7. Filter response and white noise response. a) magnitude and phase response of the 5th order Butterworth filter. b) Frequency response of the SUM signal of the First Sensor QPD for white noise modulation.

The response of the First Sensor QPD is measured with the laser modulated by bandlimited white noise (Sec. 2.5.4 & 3.4.2.3). A custom built white noise generator is used for these measurements. Table 4.5 and Fig. 4.6 describe the characteristics of the white noise generator used to modulate the laser. Figs. 4.6a-c show the voltage, histogram and the power spectrum of the generator, showing it to be white over the 0-50 KHz. The output of the noise generator is cascaded with a fifth Butterworth filter (Filter response in Fig. 4.7b) to make it band limited. The band limited white noise is then offset by a 2.0 V DC prior to

sending to the laser to avoid inputting a negative voltage in the laser modulating port. The

response of the SUM signal of the First Sensor QPD to the modulated laser is shown in

Fig. 4.7b as a nearly flat spectrum over the filter passband (i.e. 1-10 KHz).

Table 4.4. Parameters of the white noise generator

Parameters	Values (mV)	Nature
Maximum output voltage	600	
Minimum output voltage	-800	White
Mean Voltage	1.5	
Standard Deviation	139.6	

A brief summary of all the linearity tests is given in table 4.5

Table 4.5. Comparison of three linearity tests

Number	Name of the test	Frequency range tested	Results	Comment
1	IFRA	0-12.5 KHz	Linear	• Fast • Limited energy delivered to the system under test • Not suitable to test a system with large frequency range
2	SFRA	0-2.5 KHz	Linear	• Slow • Not limited by supply energy • System with all kinds of frequency range is testable
3	WNT	1-10.0 KHz	Linear	• Fast • Low energy, energy can be increased with amplifier • Suitable for small band limited system

4.6 Dynamic range

Dynamic range is the ratio of the highest measurable signal (without distortion) to the lowest measurable signal. For a detector with a maximum voltages of V_{max} and the minimum voltage $V_{min} = V_N$ (is at the level of the noise floor), the dynamic range expressed is in dB is

$$D = 20 \, log \left(\frac{V_{FS}}{V_N} \right) \qquad (4.4)$$
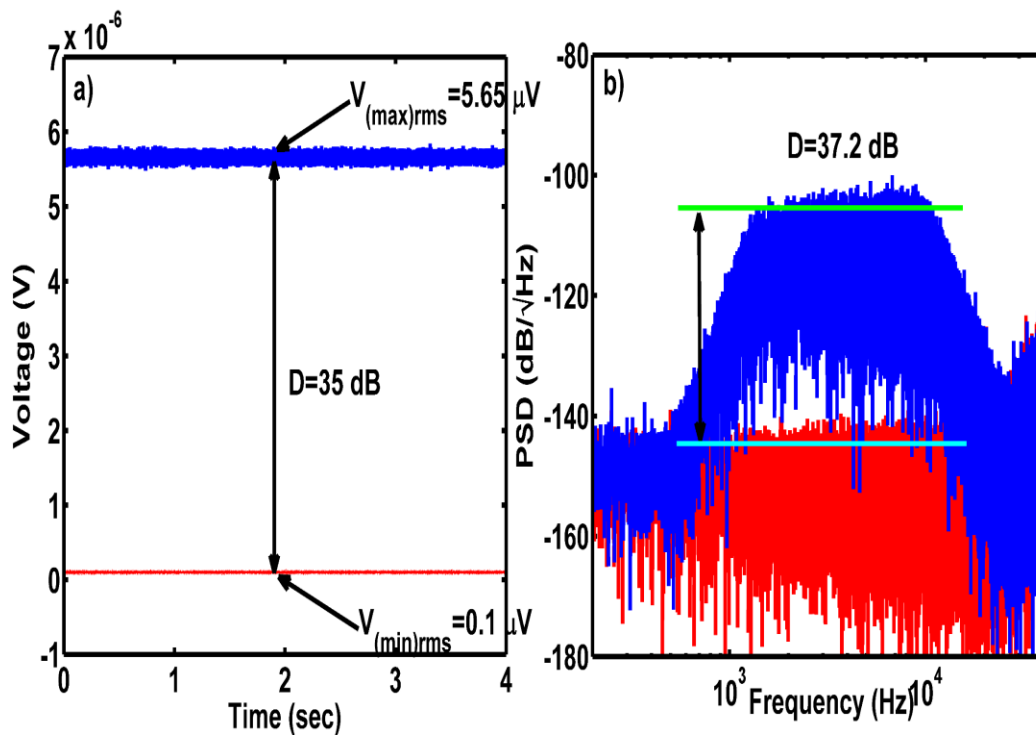
Figure.4.8. Dynamic range of the First Sensor QPD. a) Time domain dynamic range measurement. b) Frequency domain dynamic range measurement.

Dynamic range can be measured in the time domain and frequency domain analysis. Fig. 4.8 shows the results in both domains. Because the estimated frequencies were between 1.0-10.0 KHz range, the 5th order Butterworth filter and white noise generator (Sec. 3.4.2.3)

are used for this measurement. The QPD (SUM signal) generates a root mean square voltage of 5.65 µV when the laser is driven by the white noise without any reduction in optical power. When the laser is attenuated to 3.5 OD with a neutral density filter the voltage decreases to 0.1 µV (Fig. 4.8a). This voltage reduction is 35 dB which is identical to the optical power reduction with the 3.5 OD filter. In Fig. 4.8b the spectral levels decrease from -107 dB to -144.2 dB which gives a dynamic range of 37.2 dB. This 2.2 dB difference could be due to the dark current in the QPD.

4.7 Gaussian beam profiling

The waist of the gaussian beam of the laser is measured by knife-edge measurement (Sec.2.9). Fig. 4.9 shows the result of this measurement and the waist of the beam is calculated to be 6.05 µm.
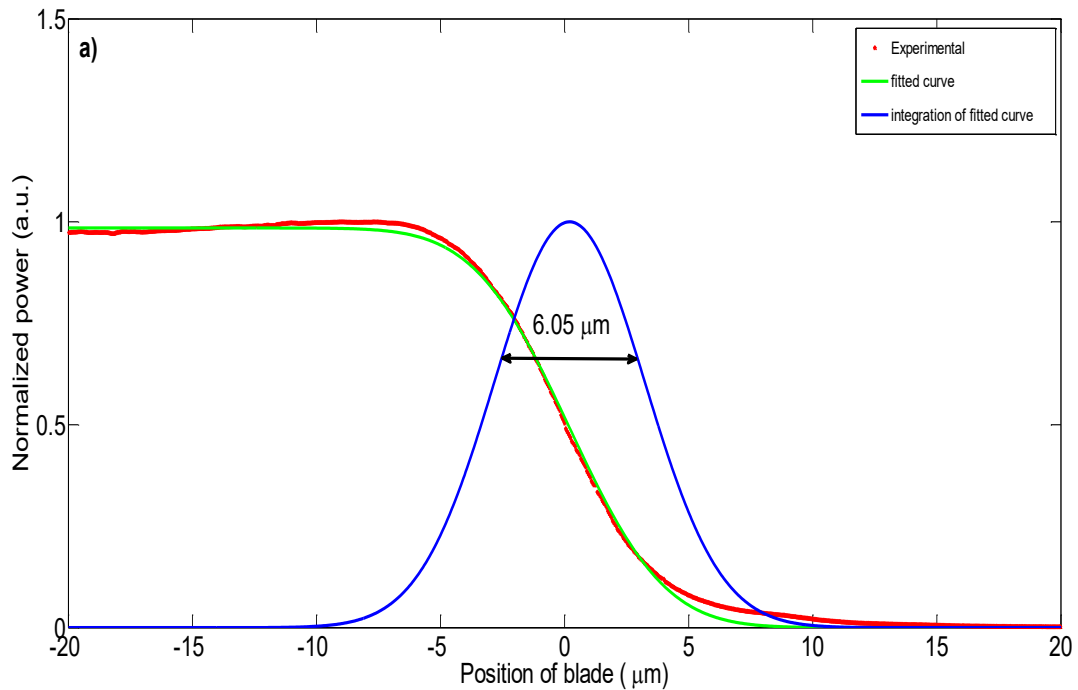
Figure.4.9. Gaussian waist measurement
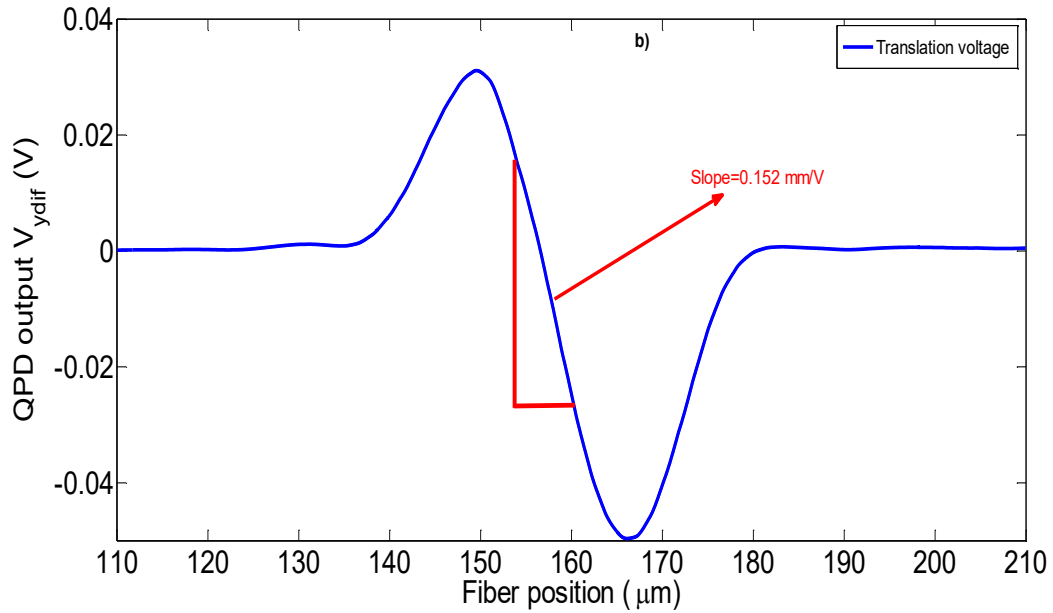
Figure. 4.10. Sensitivity of First Sensor QPD

4.8 Sensitivity factor measurement of QPD

Sensitivity factor of the QPD converts the voltage signal generated by the QPD into its equivalent displacement (Sec. 3.5). Figure 4.10 shows the measurement of this quantity using a 30 µm Schott glass fiber. The maximum sensitivity for this fiber is found to be 0.152 mm/V which is measured at an approximate distance of 300 µm from the beam focus. This value is 0.149 mm/V for 125 µm fibers. For BOS structures, the sensitivity factor is always between these two numbers. The sensitivity factor converts the QPD voltage into displacement. Multiplying the QPD X_{diff} voltage (without any sample) with these two numbers gives the limit of detection of the vibrometer (Fig. 4.11).

4.9 Discussion

  The measured vibrometer characteristic are reported in sections 4.2-4.8 and they are summarized in table 4.6. A spectrum, without any sample, represented in terms of amplitude in meter is in Fig. 4.11

Table 4.6. Summary of the measured First Sensor QPD characteristics

Parameters	Values	Notes
NEP (fW/√Hz)	0.212	Tested with a sampling rate of 16,384 Hz over a bandwidth of 8,192 Hz
LOD (Å)	0.1-0.2	Calculated by multiplying lowest and highest sensitivity factors S by X_{diff}
Linearity	Linear	Tested by three different approaches
Dynamic range (dB)	37.2	Tested both in time domain and frequency domain analysis. 35 dB using time domain.
Beam waist (µm)	6.05	Measured by knife-edge technique
Sensitivity (mm/V)	0.149-0.152	Measured by scanning a 30 µm glass fiber. The variation in sensitivity S is for the samples reported in this study
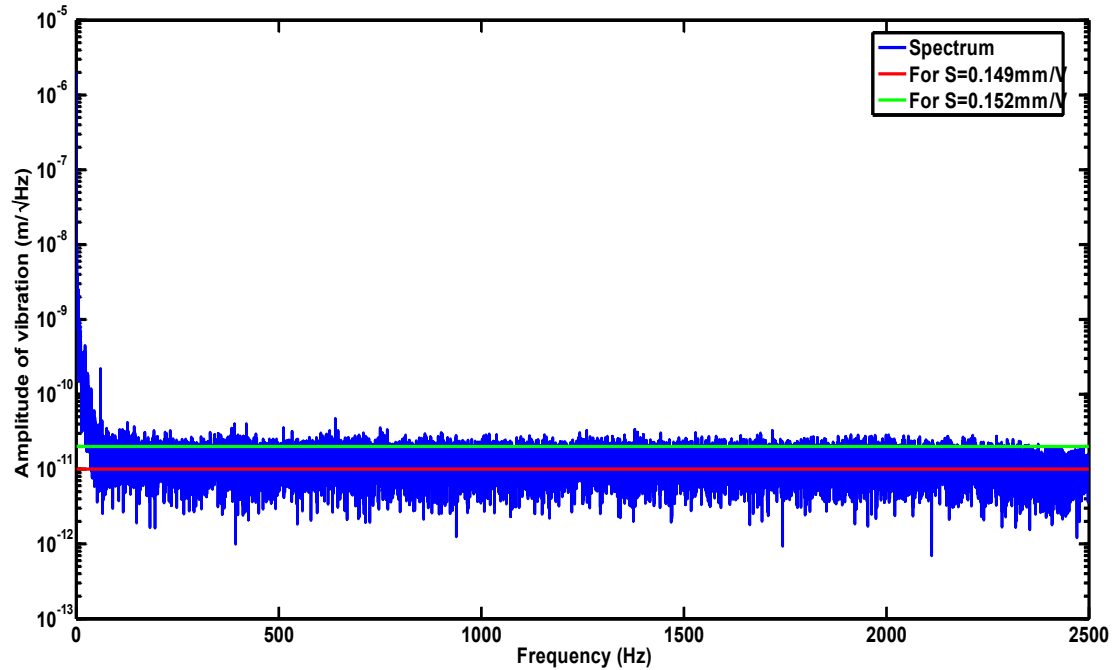
Figure.4.11. Limit of detection of the vibrometer. This X_{diff} signal is measured with the laser beam centered for minimum displacement output. X_{diff} is multiplied by S to give spectrum in m/√Hz.

The blue curve in this figure is a typical spectrum that shows noise equivalent displacement or LOD of the QPD. This blue curve is obtained by multiplying sensitivity factor 0.152 mm/V to the QPD X_{diff} signal when there is no sample present in optical beam path. The straight green line is the RMS value that makes the LOD as 0.2 Å. Multiplying the same spectra (of QPD X_{diff} voltage) with sensitivity factor 0.149mm/V gives an RMS LOD of 0.1 Å which is shown by red straight line. The range of sensitivity factor between 0.149-152 mm/V dictates the LOD between 0.1-0.2 Å.

To place the results in perspective, we compare the vibrometer with the results in the literature. Table 4.7 summarizes the optics-based displacement detection instruments reported from 1970 to date, including the vibrometer studied here. Note the prevalence of interferometry-based detection. Only three papers reported a lower detection limit of

82

amplitude compare to ours. Royer and Dieulesaint reported the most sensitive

interferometer based detection with a sensitivity of 10^{-4} Å [125]. Denk [90] and Celik [126]

reported lower sensitivities than the vibrometer. But note that all these works are based on

interferometry, which is recognized as a being more sensitive than the incoherent method

presented here.

Table.4.7. Performance of several optical displacement detection methods

Reference	Type	Resolution
[127]	Photomultiplier	5.0 μm
[128]	Interferometer	50 pm
[129]	Optical microscope	1.0 nm
[125]	Interferometer	10^{-4} Å
[90]	modified differential interference contrast microscope	1 pm
[130]	optical-heterodyne interferometer	0.26 nm
[131]	Balanced interferometric detection	< 1.0 nm
[132]	Optical Heterodyne	5 nm
[133]	Optical trap	3 nm
[134]	Intensity modulation	90 nm
[135]	Confocal scanning microscopy	5 nm
[136]	Optical modulation	14 nm
[137]	Speckle analysis	1 nm
[138]	Variable-air-gap optical waveguide	1.7 nm
[139]	Optical coherence tomography	10 nm
[140]	Optical heterodyne	0.2 nm
[141]	Michelson interferometer	10 nm
[126]	X-Ray interferometer	5 pm
[142]	Image processing	30.8 nm
[143]	Optical modulation	0.99 Å

The vibrometer reported here	QPD based direct detection	0.1 Å
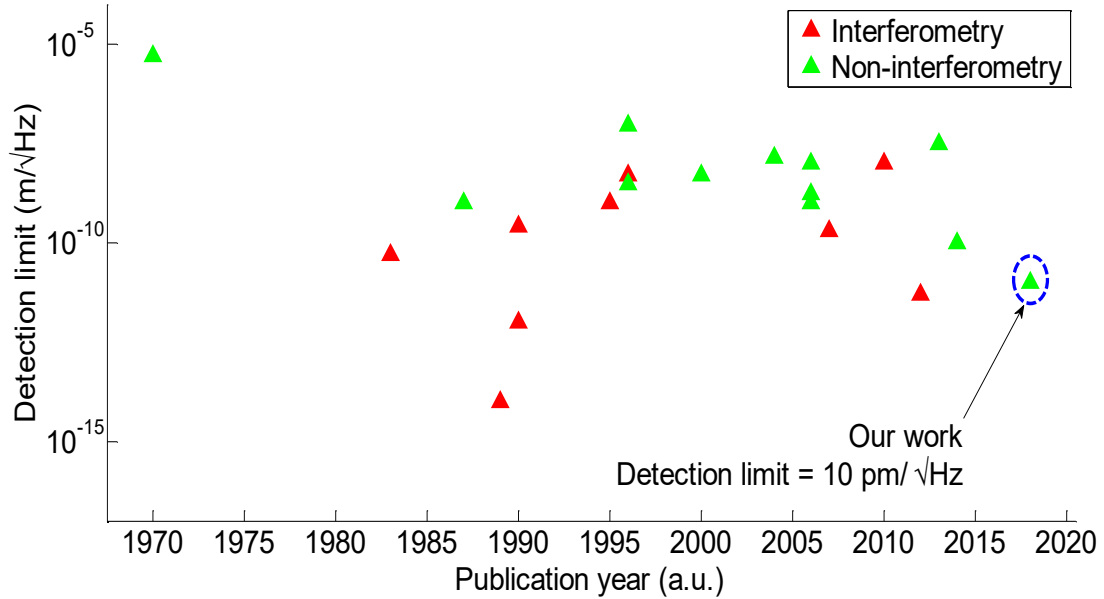
Figure.4.12. Trend of reported sensitivities of optical displacement detection since 1970

Fig. 4.12 plots the reported detection limits by year, with interferometric and non-interferometric methods distinguished. The sensitivity of our detection system is higher by ~10X than the previous non-interferometric system reported [143].

4.10 Conclusion

The vibrometer characterization has been in this chapter. The limit of detection of the QPD is below 0.2 pW. The sensor can detect vibration amplitudes as low as 0.1 Å (at a SNR of 1). IFRA, SFRA, and WNT tests indicate that the instrument is linear over a 12 KHz bandwidth. The dynamic range of the instrument is 37.2 dB. Comparison with previous reports on displacement sensors shows the position measurement sensitivity of

the vibrometer is ten times better than the best non-interferometry based systems reported. In Chapters 5 and 6, the vibrometer will be used to measure the thermal vibration spectra of nanomechanical structures.

CHAPTER 5
DEMONSTRATION OF VIBROMETER WITH MICROFIBER CANTILEVERS

5.1 Introduction

This chapter demonstrates the ability of the vibrometer (Chapter 4) to detect and measure thermal vibrations of cylindrical microfibers. Then in Chapter 6 the method is used to measure more complex-shape BOS structures. Using cylindrical fibers as cantilevers provides a useful reference structure for the calibration of the vibrometer. The fibers are 30 µm diameter glass fibers (Schott GOF85) and 125 µm single mode fiber optic light guides (Thorlabs SM600). The 30 µm fiber has about the same diameter as the beads of the BOS structures. The length of the cantilever is chosen to have stiffness in the same range as anticipated for the BOS structures. The uniformly cylindrical shape and refractive index of the fibers produces well controlled refraction of light. The vibrometer measurements of these fibers give results that are consistent with bulk property measurements of the modulus of the glass that comprises the fibers, and are shown to be sensitive enough to measure sub-nanogram changes in mass loading

5.2 Mounting fibers in the vibrometer

The fibers are highly insulating and build up charge which leads to them attracting dust and oil from the air. Therefore, before mounting them in the vibrometer, the fibers are cleaned with ethanol and deionized (DI) water, then dried with a filtered air gun. For 125 μm fibers, the buffer jacket is removed with a Newport Micro-Strip Precision Stripper. Then dry optical tissue is used to remove the residual particles left from the buffer layer. Mounting supports for the fibers are made from a glass microscope slide that is cleaned in the same way as the fibers, and then using a diamond dicing saw cut into a small-pieces (~1" × 0.75"). The fiber is hot glued (Gorilla 4" high-temp mini glue stick) to the glass support using a heat gun (Stanley GR25-Pro). The glass support is clamped into the long cylindrical holder (Fig. 5.1). In experiments where the fiber is driven by an external excitation, the glass is glued onto a piezo plate (STEMINC SM SPK2724300). A second piece of glass glued to the piezo plate fits into the clamp of the sample holder.
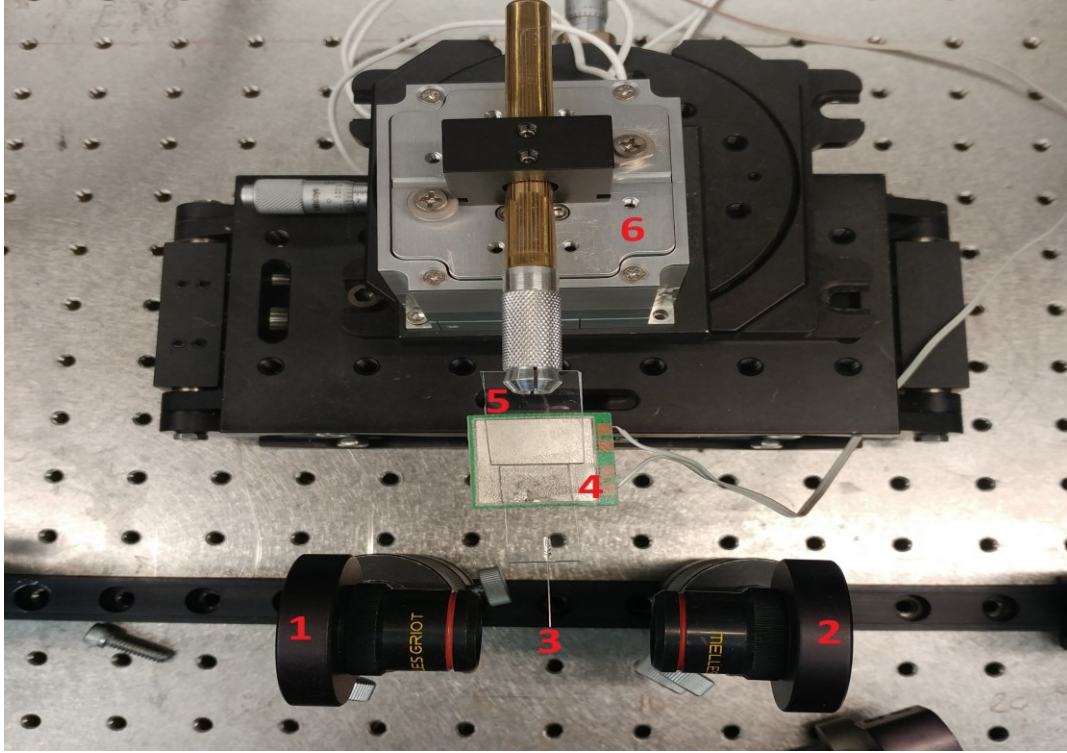
Figure 5.1. The mechanics used to position micromechanical structures, e.g. the fiber shown, in the laser beam path of the vibrometer. (1~2→ lenses, 3→fiber, 4→piezo plate, 5→glass slide, 6→nanopositioner)

The sample holder is mounted (as shown in Fig. 5.1) to a 3D nanopositioning stage (Mad City Labs Nano-2D200) that has positioning resolution of 1 nm (in all three axes) and a scan range of 200 μm. The nanopositioner rests on top of two coarse positioning stages (Thorlabs L490 and XYR1) that provide alignment of the sample to the laser in x,y,z, (13.0 mm×13.0 mm×57.4 mm) and 360° rotation in the x,y plane.

The fiber oriented horizontally is positioned 10-20 μm above the laser beam for vibration measurements. The nanopositioner then scans the tip of the fiber downward through the laser beam while the deflection voltage from the QPD is recorded. This

measurement is repeated at several locations along the axis of the laser beam to determine the position of maximum sensitivity (as described in sec. 4.8). This position of maximum sensitivity is found ~ 15-20 μm from the waist of the beam. When the length of the 30 μm diameter fiber exceeds 20 mm, the fiber bends due to gravity, which makes the beam-fiber alignment difficult. Thermal vibration of other glass fibers has also been studied. Thorlabs SM600 single-mode fiber is tried without any kind of modification to the fiber structures. The translation curve (Fig. 4.9) with this fiber is distorted due to the buffer jacket. Later the buffer is removed, and vibration is measured. Sensitivity S (Sec. 3.5) of a 125 μm diameter fiber is measured to be 149 μm/V, while for the 30 μm diameter fiber the sensitivity is measured to be 152.0 μm/V (as in Sec. 4.8).

5.3 Thermal vibration measurements

5.3.1 Measurements of 30 μm fibers

Vibrometer measurements of thermal vibration (i.e. no external drive) are performed with the First Sensor QPD (Figs. 5.2-5.6). The spectra are calculated by FFT from 20 s of data sampled at a 5 KHz rate. The laser spot size is chosen between 28-32 μm that correspond to the maximum sensitivity factor S (Sec. 3.5) by placing the sample away from the focus, for measurements of the 30 μm fibers and 120-130 μm for the 125 μm fibers. Table 5.1 reports the vibration parameters derived from the spectral measurement by fitting the spectra with the Lorentzian (Eq. 2.8) by the technique described in Appendix B. The parameters are also modeled (stiffness k using eq. B1 in Appendix B, amplitude $\bar{x}$ using eq. 2.71 and resonance frequency f_0 using eq. 2.9. Manufacturer provided value of elastic modulus E=71 GPa and density ρ= 2650 Kg/m^3 are used in these model equations.

Table 5.1. Measured and modeled results for cantilevered fibers

Sample #	Dimension		Measured from spectra					Modeled		
	d (μm)	L (mm)	f_0 (Hz)	SNR (dB)	$\bar{x}$ (Å)	k (mN/m)	Q	f_0 (Hz)	$\bar{x}$ (Å)	k (mN/m)
1	30	10.2	209.2	31.2	7.3	8.1	27.0	209.5	7.15	8.0
2	30	20.9	49.4	41.4	19.2	0.93	8.3	49.9	21.0	0.93
3	125	60.2	24.1	53.2	6.0	11.1	5.0	25.0	5.9	11.8
4	125	20.05	224.4	23.8	1.2	313.9	39.0	225.9	1.1	318.0

(**Measured** f_0, $\bar{x}$, and k using eq. 2.8. **Modeled** f_0 using eq. 2.9, $\bar{x}$ using eq. 2.71, and k using eq. B1)
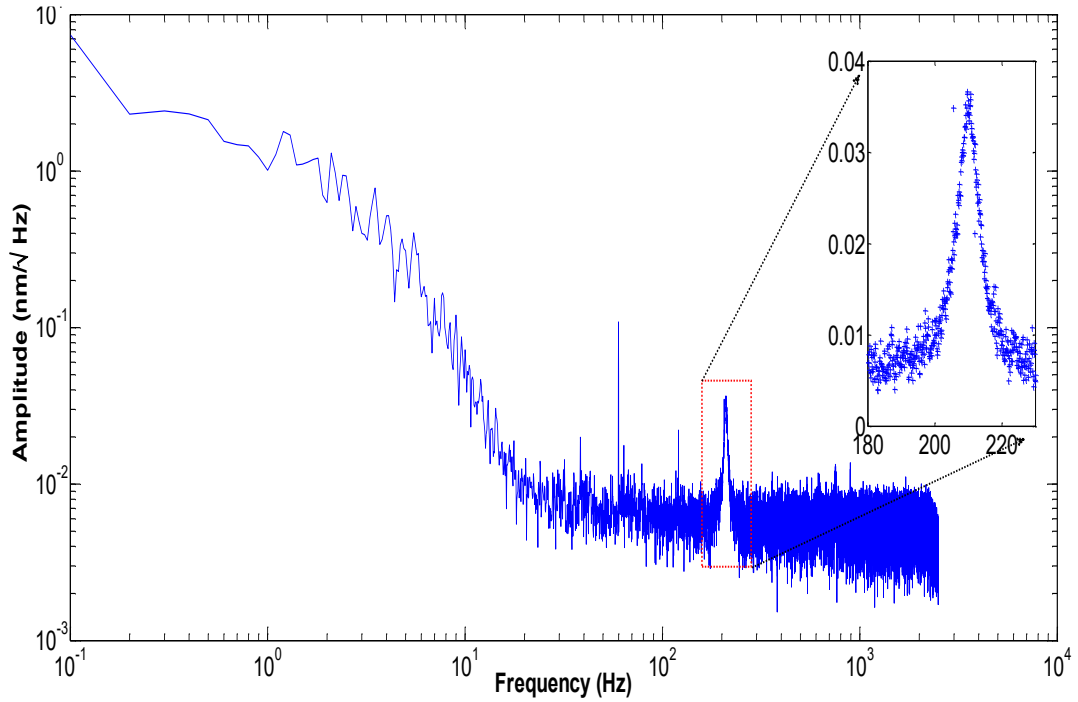
Figure 5.3. Thermal vibration spectrum of Sample 1. Inset: Closeup of the resonance that is fit to eq. 2.8 by method from Appendix B that yields the measured values reported in Table 5.1

Figure 5.3 is the spectrum of Sample 1. The 1/f noise is evident up to 10.0 Hz. The narrow peak at 60 Hz is leakage of line voltage from the QPD power supplies. The peak at 209.2 Hz is the fundamental resonance of the fiber. As shown in Table 5.1, the peak amplitude is 7.3 Å and Q is 27. The modeled values (Appendix B) of 209.5 Hz and amplitude of 7.15 Å closely matches the measured values.

For the spectra of the 20.9 mm fiber (Fig. 5.4) the modeled and measured values are also close to each other.
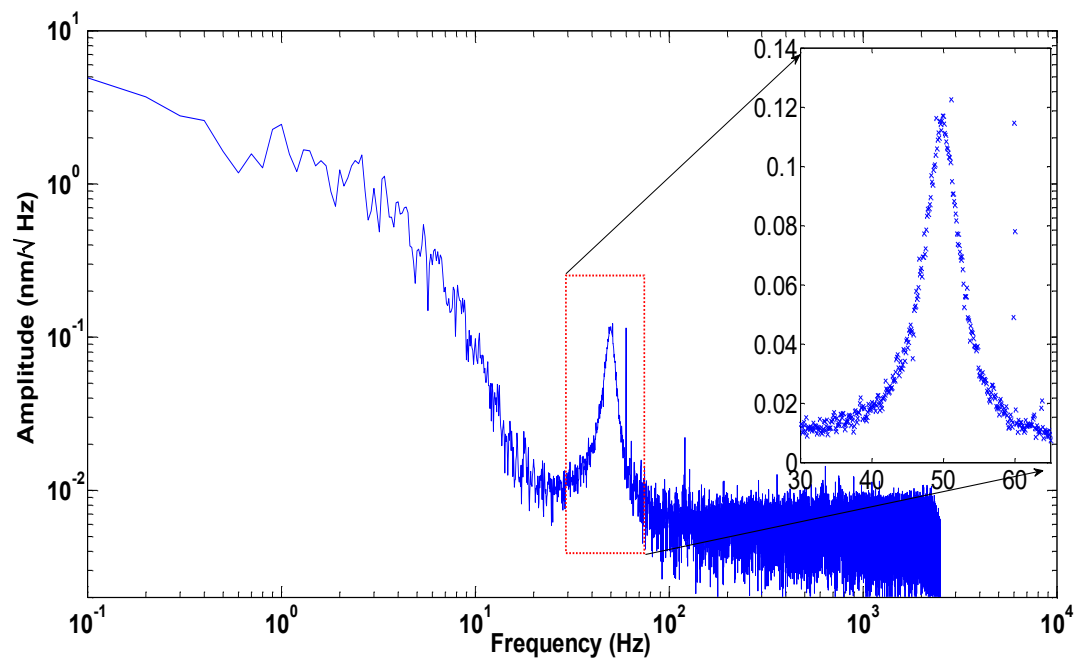
Figure 5.4. Thermal vibration spectrum of Sample 2. Inset: Closeup of the peak that was fit to eq. 2.8 by method from Appendix B that yields the measured values reported in Table 5.1

5.3.2 Measurements of 125 μm fiber optics
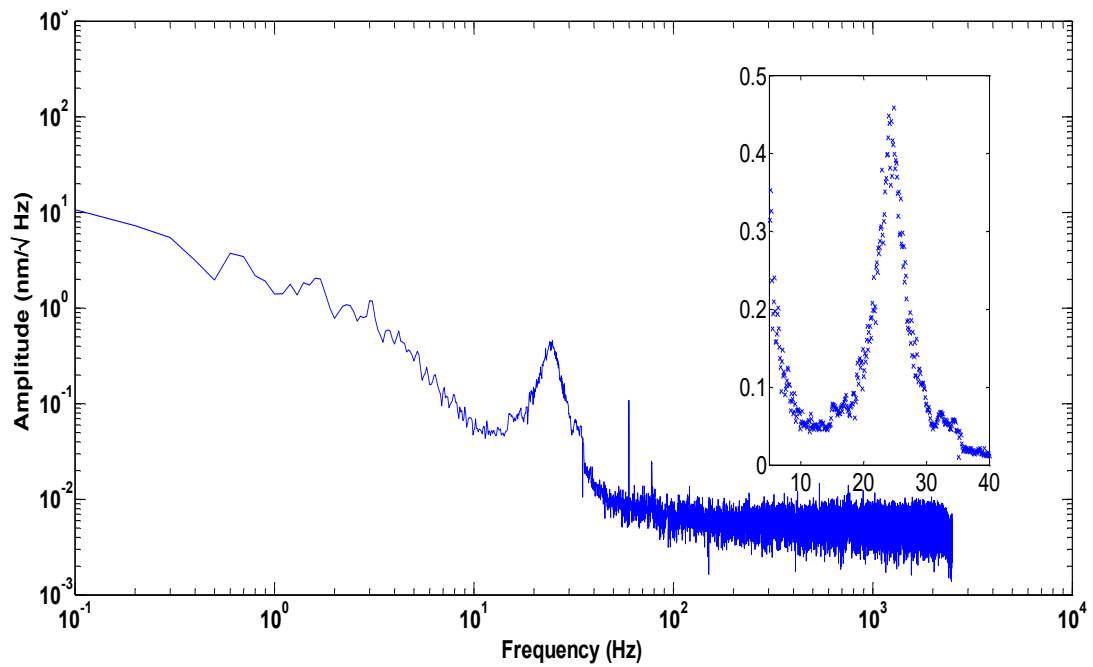
Figure 5.5. Thermal vibration spectrum Sample 3, Inset: Closeup of the peak that was fit to eq. 2.8 by method from Appendix B that yields the measured values reported in Table 5.1

These cantilevers are stiffer than the cantilevers made with the 30 μm fibers, giving amplitudes that approach the noise floor limited detection limit. Even for Sample 4 that has only a 1.1 Å amplitude, it is nonetheless possible for the modeled and measured parameters to closely match each other.
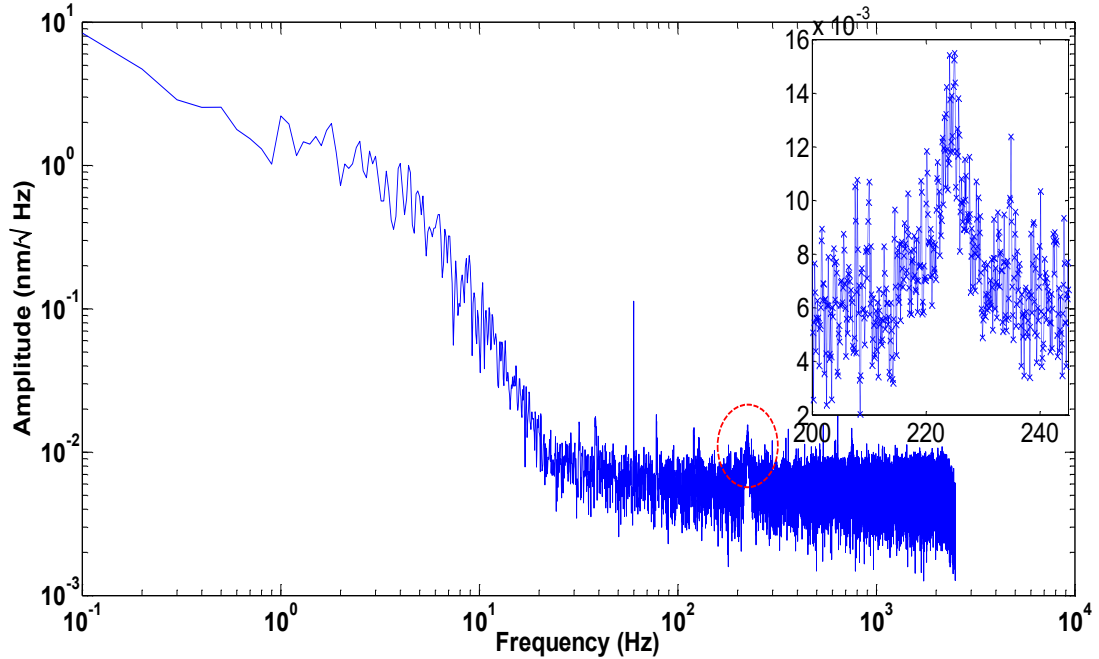
Figure 5.6. Thermal vibration spectrum Sample 4. Inset: Closeup of the peak that was fit to eq. 2.8.

Table 5.1 shows how the vibration parameters change based on the dimension of the fibers. The white noise background (above 10 Hz) is ~0.1 Å (calculated by multiplying the QPD difference voltage by sensitivity factor S as described in sec. 4.9). As an example of the structures (Sample 4 in Table 5.1) that can be measured by thermal vibration (with no external drive), from eq. 2.71, a stiffness of 0.3 N/m and Q of 39 has an average amplitude of 1.2 Å at resonance is measured at SNR=23.8. Stiffness of 0.3 N/m and less that can be measured. If the Q is 1, then the minimum stiffness that can be measured at SNR=1.8 is 0.001 N/m (using Eqs. 2.8 and 2.71).

5.4 Externally driven vibration measurements

As part of vibrometer development it worth verifying that the spectrum remains

Lorentzian at levels lower than the noise floor. Therefore, the fiber cantilevers are also excited with an external drive signal. The samples are mechanically excited with a piezo plate (StemInc Smspk724300) driven with constant amplitude (white) swept frequency signals (using method described in Sec. 3.4).
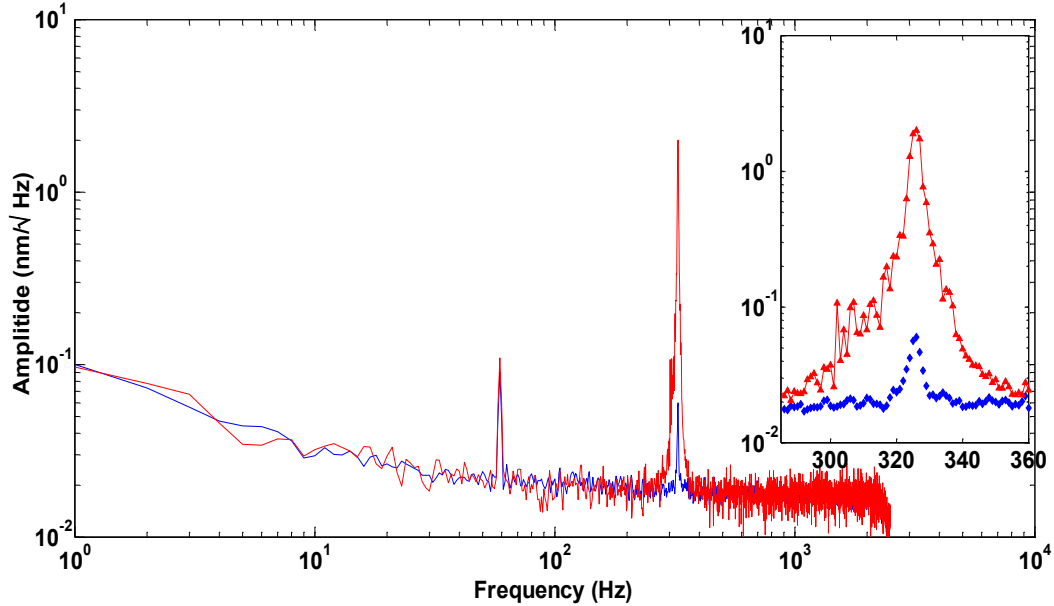
Figure 5.7. Comparison of the spectra of Sample 1 fiber excited by thermal noise (blue curve) and by a piezoplate driven with a swept frequency signal (red curve).

Sample 1 is tested by the swept frequency method (Sec. 4.4). The frequency sweep is from 270 to 370 Hz at a linear sweep time of 100 s. The amplitude of the sweep signal is 1.5 V, which is observed to generate the strongest signal. Higher drive levels cause the piezoplate to produce distorted vibration signals and nonlinear harmonics. The driven vibration spectrum is viewable over a greater dynamic range than the thermally excited spectrum (Fig. 5.7) while showing a Lorentian shape to lower levels for thermal vibration spectrum. Drive signal increases the vibration amplitude from 5.13 Å to 15.6 nm, while the

Q from 34 to 37, which is probably due to the influence of noise on estimating the half-power points (eq. 5.1b).

Figure 5.8 shows the same comparison for Sample 5 (a 14.52 mm x 30 μm fiber). The piezo-plate is driven with a 1.2 V, 50-150 Hz, 100 s sweep. Driving the cantilever increases the amplitude from 1.2 nm to 38.13 nm. The *Q* of 17.9 is the same whether driven or thermally excited.

5.5 Young's modulus from the thermal vibration spectra
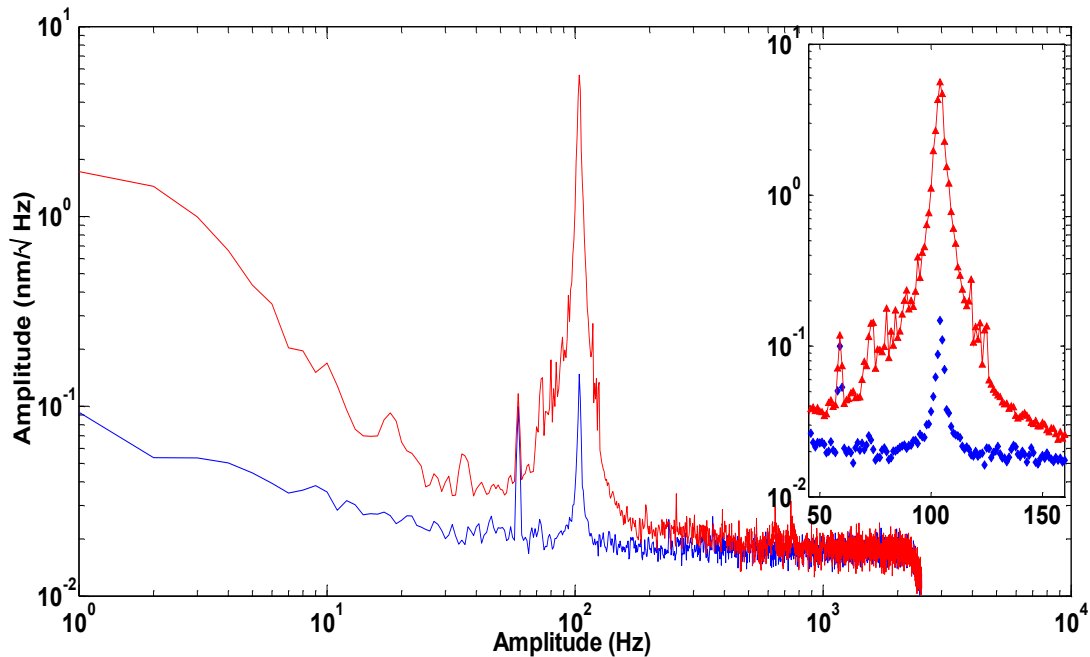
Figure 5.8. Comparison of the spectra of Sample 5 (14.52 mm x 30 μm fiber) driven by thermal noise (blue curve) and by a piezoplate (red curve).

Thermal vibration spectra of microstructures have been used as sensors, e.g. in the calibration of AFM cantilevers[20, 144, 145], determination of optical trap stiffness[76,

146, 147], ultra-small mass detection[148-150], and various temperature, pressure and composition related environmental changes. In this section we demonstrate these capabilities by determining Young's modulus of the fibers and in measuring mass loading of the fibers from thermal vibration spectra.

The elastic properties of cantilevered glass fibers are associated with the parameter of the lumped-element mass-spring-damper system presented in Chapter 2.
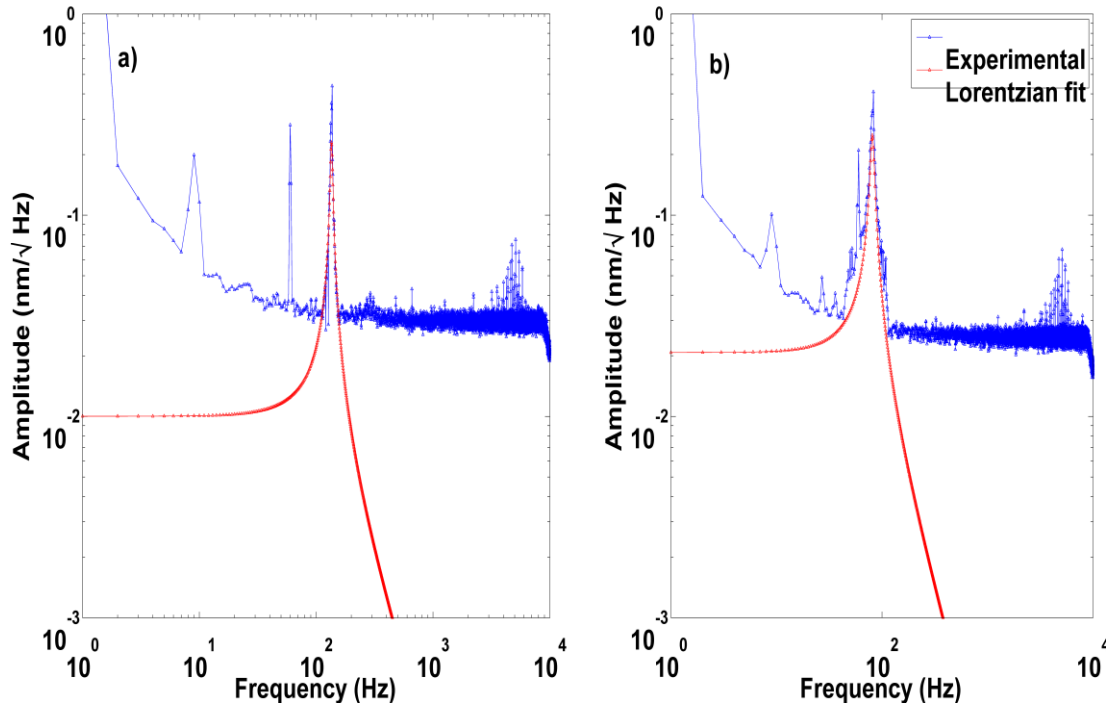
Figure 5.9. Thermal vibration spectra (blue curves) and Lorentzian fits (red curves) of a) a 12.72 mm x 30 μm and b) a 16.45 mm x 30 μm fiber cantilever.

Figure 5.9 shows the thermal vibration and best Lorentzian fits to equation 2.8 (by method of Appendix B) for two fiber cantilevers. In Fig. 5.9a the resonance frequency is 135.3 Hz, the vibration amplitude $\bar{x}$ is 0.991 nm and Q is 23. These values of $\bar{x}$ and Q are from a first fit to eq. 2.8 that correspond to the best fit (see Appendix B for detail of fit technique) with

the smallest root mean square errors (RMSE) values. Q from this first fit is then used in a second fit to eq. 2.31 to calculate elastic modulus E. Unknown parameters δ and R (Sec. 2.8.1) are also determined from this second fit using the same lowest RMSE error as the goodness of the fit. These values are reported in Table 5.2.

In Fig. 5.9b the 16.45 mm fiber has a resonance frequency of 81.4 Hz, a vibration amplitude of 1.45 nm and a Q of 13. The average Young's modulus found from these fits is 72.32.

5.6 Comparing Young's modulus results with the force-elongation measurement method

As a verification that the method of thermal vibration along with the spectral fitting (Appendix B) gives reasonable results, Young's modulus is measured by a classic macroscopic method of measuring stress vs. strain from force vs. change in length. Three glass fibers with different lengths are stretched while the force and length changes are recorded.

In the linear elastic regime of a material, a tensile force F is applied to a fiber of cross sectional area A and length L, causes the length to increase by ΔL. The parameters when combined to give stress/strain, gives Young's modulus as

$$E = \frac{\left(\frac{F}{A}\right)}{\left(\frac{\Delta L}{L}\right)} \qquad (5.1)$$
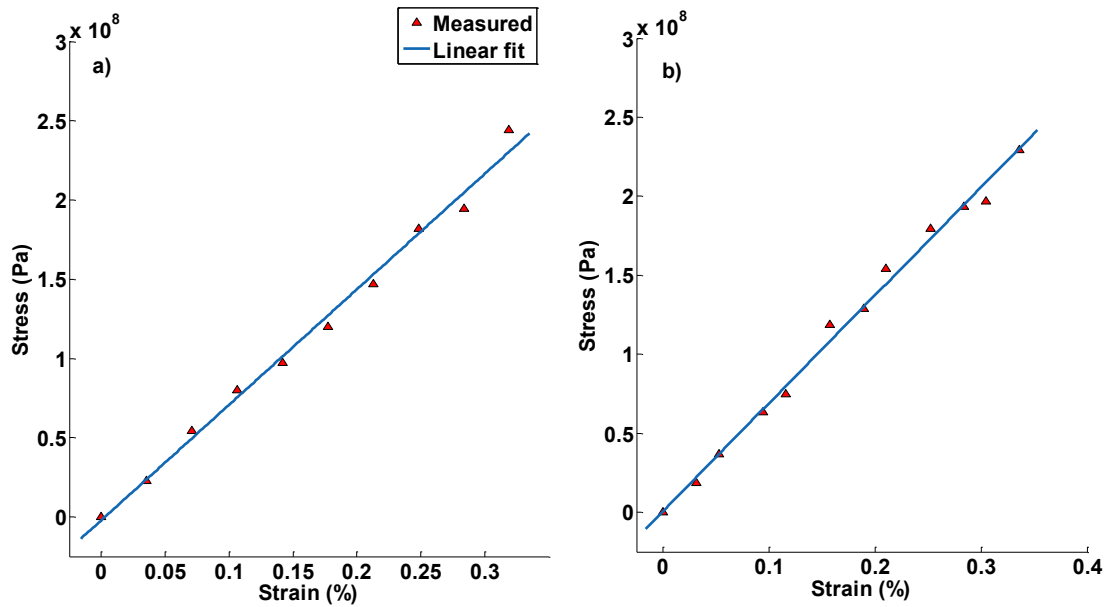
Figure 5.10. Force-elongation response of a) 56.4 mm and b) 95.2 mm long glass fibers

A digital slide caliper (Mitutoyo Cd-6 CSX, accuracy 10 μm) measures the length change. Force is measured with a laboratory balance (Mettler PM4000, sensitivity 10 μg). One end of the fiber is rigidly attached to the weighing plate of the balance and the other end is attached to the caliper. Silver epoxy (MG Chemicals 8330S) is found to be a sufficiently rigid adhesive for the forces applied to the fiber (10 mN - 0.3 N). The first reference position (corresponding to zero force) is with the fiber initially tensioned at an elongation of 10-30 μm. The fiber is stretched up to ~ 10 % (0.5 GPa) of the elastic limit (~5.0 GPa) of typical glassess. This corresponds to around 300-600 μm maximum extension and at a force of ~ 0.2 N) for the samples.

Figure 5.10 shows the force distance response of two 30 μm fibers. Red triangular spots in the curve represent the actual measurements and the blue line indicates the fit of the data to a straight line.

The slopes of the curves in Fig. 5.10a and b give a Young's modulus of 72.84 GPa and 68.25 GPa.Table 5.2 compares the two types of measurements of Young's modulus.

Table 5.2. Results of vibration measurements and force-elongation.

Thermal vibration spectra									Force-elongation		
L (mm)	$\bar{x}$ (Å)	f_0 (Hz)	SNR	R (μm)	δ (μm)	Q	E_t (GPa)	E_{avg}	L (mm)	$E_{f\text{-}l}$ (GPa)	E_{avg}
8.95	5.86	252	31.3	190	4.43	31	71.98		30	67.49	
12.72	9.91	135.32	53.9	221	6.05	23	71.87	72.32	56.4	72.84	69.53
16.45	14.5	81.4	55.3	287	7.80	13	73.1		95.2	68.25	

Columns shaded with blue in the table are values determined from the fitting method (Appendix B). The average value of Young's modulus derived from the thermal vibration measurements is 72.32 GPa which is close to manufacturer provided value of 71 GPa. And the average value from the force-elongation measurement is 69.53 GPa.

Despite using shorter fibers than the force-distance method and the high levels of background noise in the spectral measurements of the Young's modulus measurements, the thermal vibration method produces lower standard deviation. These results demonstrate the accuracy and applicability of thermal vibration spectra for characterizing the elastic properties of microstructures.

5.7 Discussion on Modulus measurement

There are numerous techniques to measure the elastic properties including elastic modulus. Numerical calculation[151-153] and finite element analysis[154-156] are used as a preliminary step to predict the elastic properties of unknown/new synthetic materials in order to choose a proper instrument for actual measurements. Experimental techniques

include scattering, tensile (Force-elongation), AFM/indentation and spectral resonance measurements. Raman[157, 158], X-rays, and neutron scattering[159] spectroscopies are widely used when the materials are in liquid or powdered form, Table 5.3 summarizes these techniques and their accuracies.

Table 5.3. A comparison of methods of measuring elastic properties

Category	Reference	Technique	Accuracy (± %)
Computational modeling	[151-153]	Numerical calculation and Finite element analysis	NA
Scattering	[157, 158]	Raman Scattering	2-5
	[160-163]	X-Ray scattering	5-40
	[159, 164-166]	Neutron scattering	2-8
Tensile	[167-169]	Force-elongation	5-15
Indentation/ AFM based	[170-177]	Nano-indentation	2-20
	[168, 178-183]	AFM indentation	3-25
	[75, 180, 184-188]	AFM force measurement	5-25
	[189-192]	Three-point bending test	3-18
Spectral identification of resonance	[193]	Forced vibration	2-14
	[24, 194-199]	Thermal vibration	1-10
	vibrometer (this report)		1-5

While scattering based techniques, especially Raman scattering, provides the most accurate (as low as 2%) measure of elastic properties, a laser vibrometer achieves the same accuracy with a fraction of cost and measurement time.

5.8 Measurements of mass loading

The vibrometer also is able to sense small changes in mass loading, well as numerous other environmental changes. Nanomechanical properties are influenced by changes in air pressure, density and relative humidity[200-202], temperature[203, 204], adsorption (mass loading), and adsorption-induced surface stress[205-207]. Changes in the environmental variable are reflected in changes in amplitude, Q and resonance frequency[208-210]. In 2004 Gupta et al.[25] measured the mass of a single vaccinia virus (9.5 fg) by using a laser doppler vibrometer. Here we specifically report on measurements of mass loading and demonstrate a sensitivity as low as 120 ng.

5.8.1 Mass detection by shifts of the resonant frequency

Shifts in the resonance frequency are used to estimate mass loading. To correctly account for mass loading, it is important to recognize that the effective mass m^* is actually the mass that gives the resonance frequency

$$f_0 = \frac{1}{2\pi}\sqrt{k/m^*} \tag{5.2}$$

The effective mass $m^* = nm$ is usually a fraction n of the total mass m of the sample that accounts for differences in displacement along the length of the cantilever. Its value depends on the shape of the sample. Mass that is more concentrated towards the tip produces an effective mass that is closer to the total mass of the cantilever. For a cylindrical cantilever, the value of n is 0.243.

Changes in the resonance frequency can be caused by perturbations in both mass δm and stiffness δk (due to surface stress produced by adsorbate). The shifted frequency written in terms of these perturbations is

$$f_1 = \frac{1}{2\pi}\sqrt{\frac{k + \delta k}{m^* + \delta m}} \tag{5.3}$$

For small changes in stiffness and mass equation 5.3 can be approximated as

$$f_1 = f_0\left[1 + \frac{1}{2}\left(\frac{\delta k}{k} - \frac{\delta m}{m^*}\right)\right] \tag{5.4}$$

When stiffness changes are ignorable such as loading with a low viscosity liquid, eqs. 5.3 and 5.4 can be combined and approximated to give

$$\delta m = \frac{k}{4\pi^2}\left(\frac{1}{f_1^2} - \frac{1}{f_0^2}\right) \tag{5.5}$$

5.8.2 Measurement of mass of adsorbed liquids

Mass loading measurements are made of liquid drops adsorbed to the tip of fiber cantilevers. For comparison, masses are also estimated by image analysis of drop volumes.

Table. 5.4. Summary of mass detection experiments

Material	Frequency shift			Image analysis		
	Frequency shift (Hz)	Mass (μg)	Q^*	Volume (10^{-12} m^3)	Mass (μg)	Relative difference (%)
Oil	1.0	0.1216	13→8	0.1109	0.102	16.12
	33.6	7.23	13→11	8.269	10.42	30.61
Glycerin	19.61	3.20	13→17	3.108	3.971	19.4
	11.6	1.655	13→10	1.36	1.714	3.4

*→ represents after mass loading

The frequency shift method is performed as follows. First the unperturbed frequency is measured, then the tip of a cantilevered fiber is immersed in the liquid. Either a single drop

or a string of drops forms at the tip of the fiber. The tip is then placed under the microscope to measure the location of the drop. When multiple drops form, all of them, except the one closest to the tip, are blotted off by sliding a paper tissue along the fiber. The preferred configuration is for the remaining drop to rest a few micrometers away from the tip of the cantilever so that a cylindrical shape is presented to the vibrometer's laser beam. For the comparison measurement, the same drop is photographed under the microscope and the dimensions of the image are measured to determine volume of the drop. Resonance frequency f_0 is the only parameter needed to measure the loaded mass and f_0 is determined by visual inspection for all the spectra presented in this section. Figure 5.11 shows that the frequency decreases by 1.0 Hz with this loading of a 14.3 mm x 30 μm fiber. Using the shifted and unshifted frequencies in equation 5.4 gives a mass of 121.6 ng.
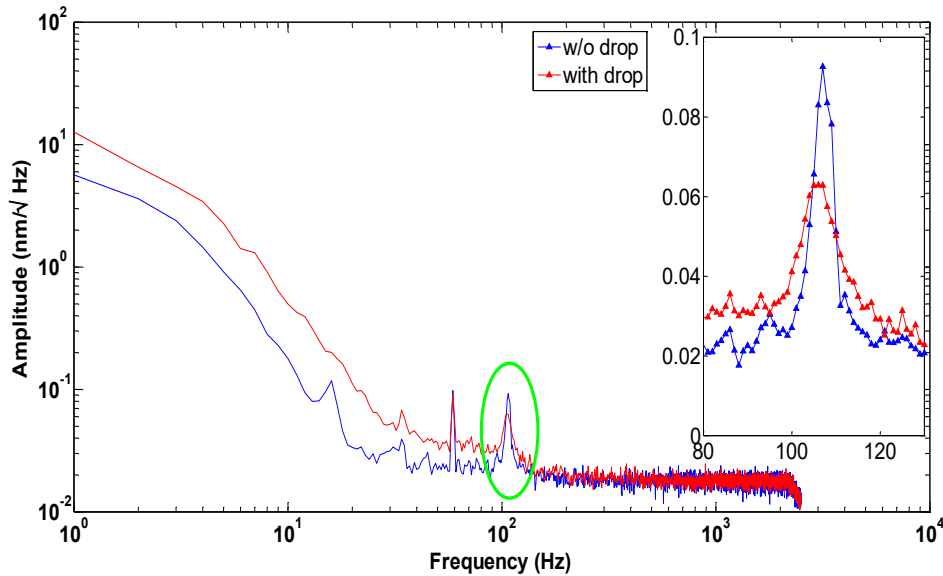
Figure 5.11. Frequency shift due to added mass of the oil drop in Fig. 5.12.
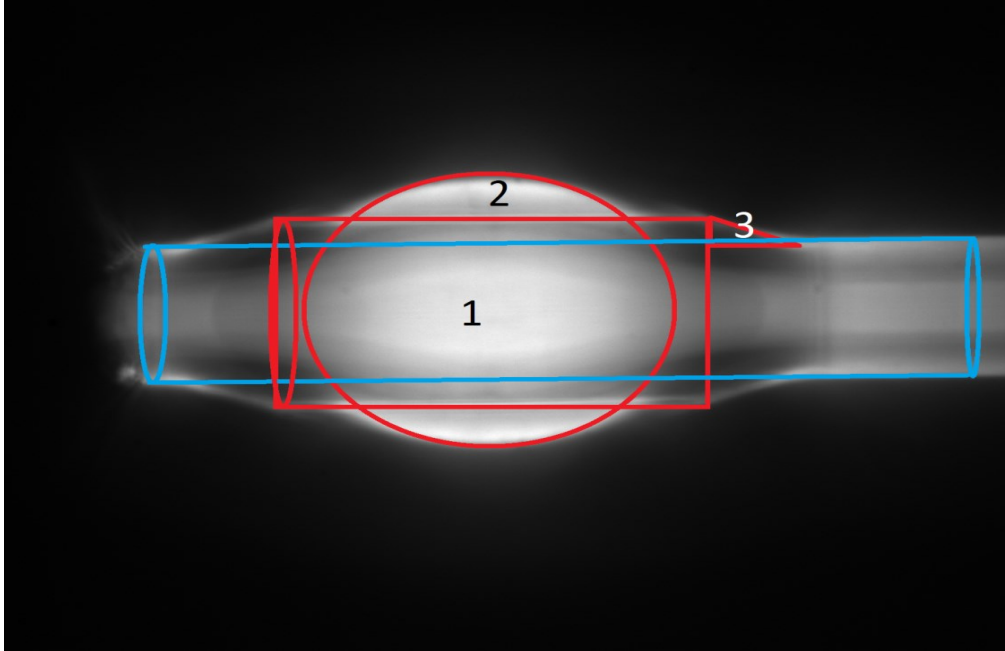
Figure 5.12. Dimension of oil drop on fiber tip

Figure 5.12 shows that the shape of the drop departs from spherical. The volume is estimated by fitting it to three volume elements (labeled 1,2,3 in the figure): a cylinder, hollow sphere, and a cone with a cylindrical section removed from their centers. The drop volume is measured to be

$$V = v_1 + v_2 + v_3 = 1.1091 \times 10^{-13} m^3$$

Multiplying by the density of the oil 920 Kg/m^3 gives a drop mass of $102.0\ ng$ which is 16% lower than by the thermal vibration measurement. This difference appears to be mostly due to the limited frequency resolution of the spectrum. The frequency resolution in this figure was 1.0 Hz which translates to a mass resolution of 120 ng. Increasing the frequency resolution to a factor of 10 would give the shifted frequency to anywhere

between 0.1 to 0.9 Hz. That means the mass measured from the spectra could be 10-90% off from the real value. These results, and for 3 other droplets are summarized in Table 5.5 with spectra and droplet images given in Figs. 5.13-18.
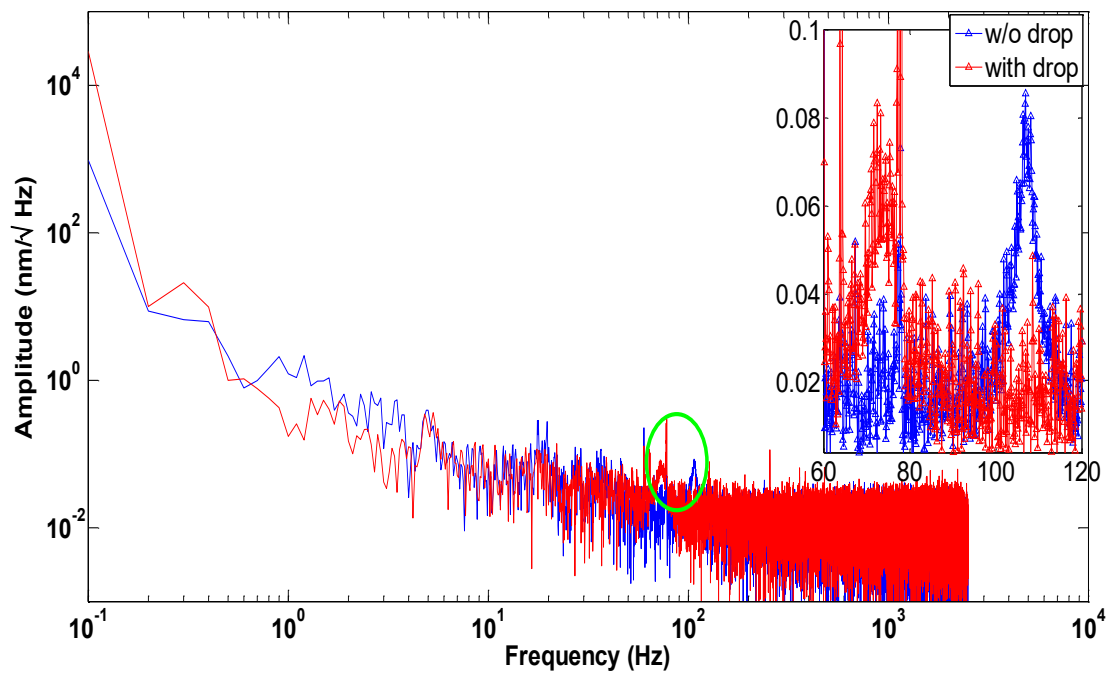
Figure 5.13. Frequency shift when a glycerin drop of Fig. 5.14 is adhered to the fiber.
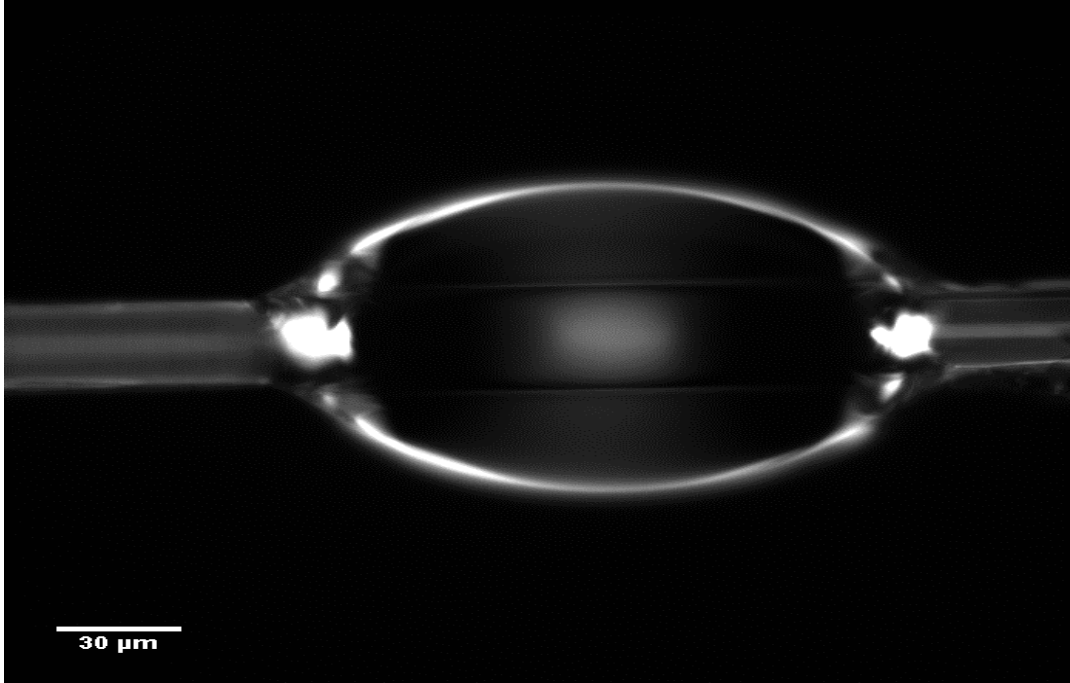
Figure 5.14. A drop of glycerin near the tip of the fiber

The measurement is repeated with the drop of glycerin in Fig. 5.13. This time the data is collected for 10 seconds (instead of 1 second) giving a frequency resolution in the spectrum of 0.1 Hz (corresponding mass resolution of 12 ng). As shown in Fig. 5.14, the resonance decreases by 33.6 Hz. From equation 5.7, the mass of the glycerin drop is 7.23 µg. The shape of the drop in Fig. 5.14 is modeled as a prolate ellipsoid (minus the cylindrical volume of the fiber). The major axis is a = 146.15 µm and the minor axis is b = 116.97 µm. The mass of the drop along with fiber is then calculated as

$$m_1 = V_1 \times \rho = \frac{4}{3}\pi ab^2 \times 1260 = 10.55 \text{ ng}$$

Subtracting the mass of the fiber (0.1229 ng) from this ellipsoid would yield a mass of 10.42 µg. This is 1.44 times larger than the mass calculated from the spectra. A possible

explanation could be the large changes in the spectral shape due to the large change in Q that are not accounted for in the model.
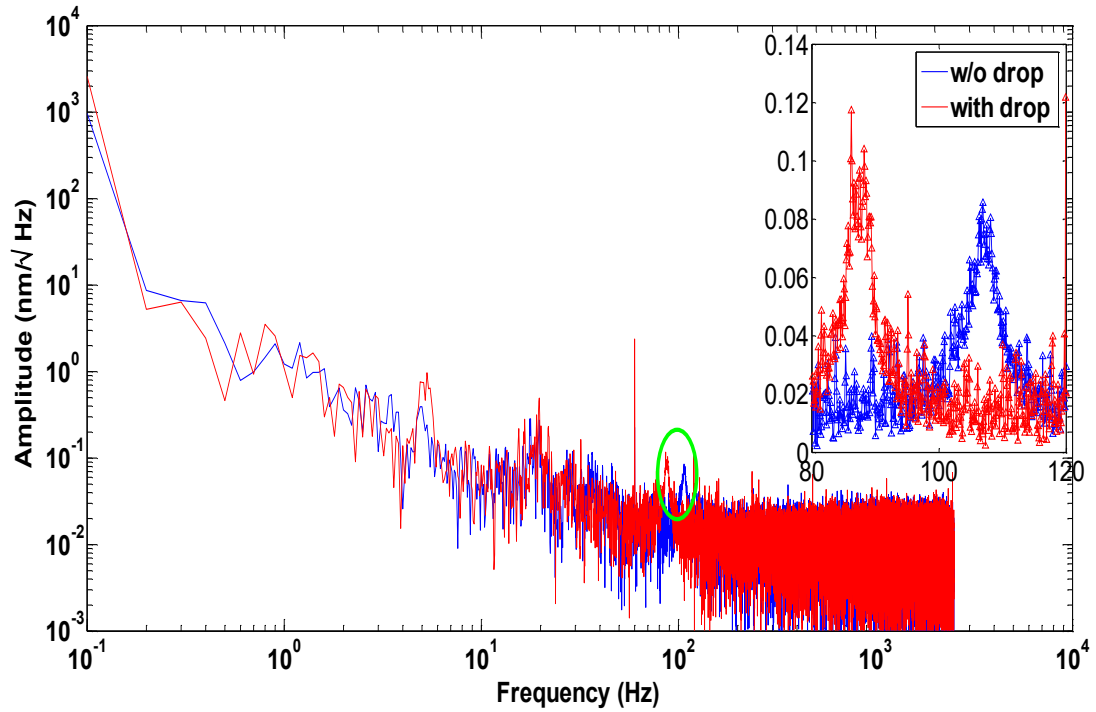
Figure 5.15. Shift in resonance frequency for the added drop of glycerin in Fig. 5.16.
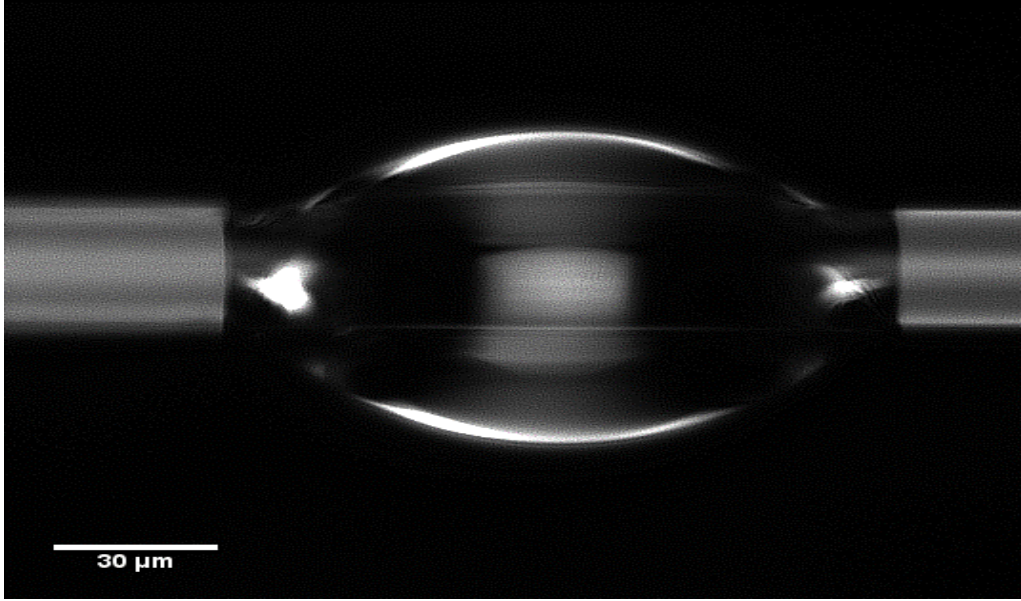
Figure 5.16. Image of glycerin drop on fiber tip
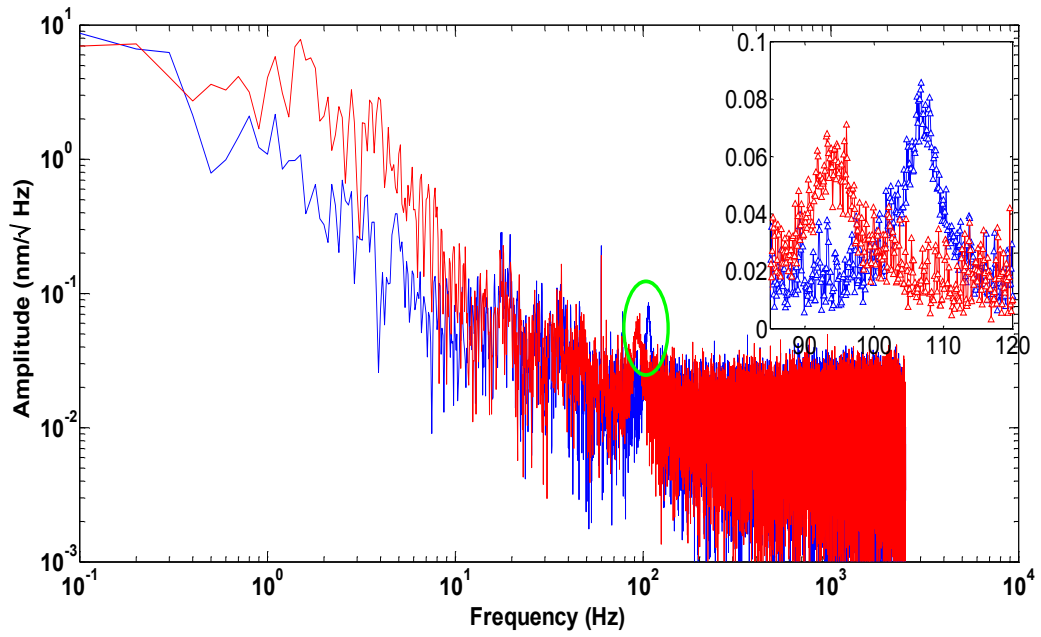
Figure 5.17. Frequency shift for the addition of the glycerin drop in Fig. 5.18.
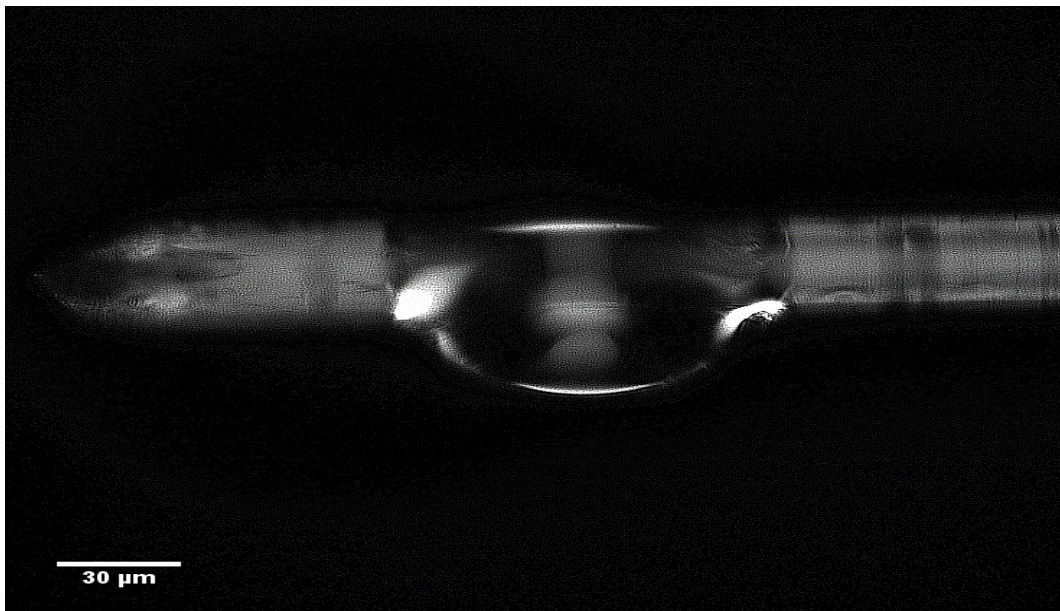
Figure 5.18. Small asymmetric glycerin drop on fiber tip.

Figs. 5.16 and 5.18 show two glycerin drops of smaller size than in Fig. 4.14. The corresponding spectra are Figs. 5.15 and 5.17. The change in the resonance frequency decreases with the drop size. Mass calculated from the spectral shift are 3.2 and 1.6 µg respectively whereas the mass from the image analysis are 3.9 and 1.7 µg. The differences in two techniques are also decreased to 19.4 and 3.4 %. This trend suggests that accuracy of the mass detection is higher for smaller sized drops. It is estimated using eq. 5.5 that the accuracy of the detection can be achieved to 1.2 picogram (compared to 120 ng for drop 1 and 12 ng for drops 2-4) by increasing the sampling resolution to 0.0001 Hz (compare to 1.0 Hz for drop 1 and 0.1 Hz for drops 2-4), but, that better resolution comes with an increase in data acquisition time by a factor of 1000 (i.e. longer experiment time). The sensitivity can be further improved using a longer cantilevered fiber of lower stiffness. These suggestions however only true if the Q of the vibration does not decreases more than ~10% from the original structure (i.e. fiber).

5.9 Review of mass detection methods

The most sensitive mass detection methods are cryogenic detection[211-213], Fourier transform ion cyclotron resonance (FTICR)[214-216], charge detection[217-219], ion trapping[220-222], and nanomechanical resonators[223-227]. A comparison of these techniques in terms of their detection sensitivities is given in the table 5.5[228]

Table. 5.5. A comparison of ultra-small mass detection techniques

Technique	Reference	Range of detection sensitivity (Da) $Da=1.66\times10^{-27}$ Kg	Limitations
Cryogenic detection	[211-213]	$1-10^7$	Poor energy resolution for charge determination

111

FTICR	[214-216]	10^5-10^8	Time consuming measurements
Charge detection	[217-219]	10^{12}-10^{15}	Requires high potential difference
Ion trapping	[220-222]	10^5-10^{17}	Only applicable to very highly charges objects
Nanomechanical resonators	[223-227]	10^5-10^{14}	Stiffness of the resonators must be known

Cryogenic detection which is based on time of flight measurement is the most sensitive mass spectrometry that can detect a mass as low as 1 Da (atomic mass unit). This technique along with the next three methods in the table require acceleration of the target objects through a high electric or magnetic field. While these techniques offer a better mass detection capability, they also come with large set-up and maintenance cost due to regular calibration requirement. Our detection technique falls under nanomechanical resonator category. A nanomechanical sensor with 1.66 Da resolution has been reported by J. Chaste et al. [229] which is the lowest detection limit reported in this category. These highly sensitive resonators are either nanotubes that several hundred nanometers long or micromachined cantilevers where the stiffness of the cantilever is minimized significantly by carefully choosing their dimensions. These structures have much high resonance frequencies (MHz-GHz) than the fiber cantilevers. Because mass loading changes are relative to the resonance frequency, much larger frequency shifts occur for the higher frequency sensor. This sensitivity of our detection can be improved to at least 2-3 orders of magnitudes by 1) increasing the duration of the time-series data 2) using a thinner fiber 3) using a softer fiber 4) using a longer fiber.

5.10 Conclusion

This chapter demonstrates that the vibrometer (outfitted with cantilever glass microfibers) can

- Detect thermal energy driven Brownian fluctuations down to amplitudes as low as 0.1 Å without any external excitation.

- Measure Young's modulus of the glass microfibers to within 3.0%.

- Measure mass loading down 120 nanogram and with increased frequency resolution by increasing data acquisition time and using low stiffness fibers, it could measure down to 1.2 picogram.

These studies confirm the usefulness of the vibrometer for studying vibrations of polymer BOS structures, which is the subject of chapter 6.

CHAPTER 6
THERMAL VIBRATION SPECTRA OF BEAD-ON-A-STRING (BOS) FIBERS

6.1 Introduction
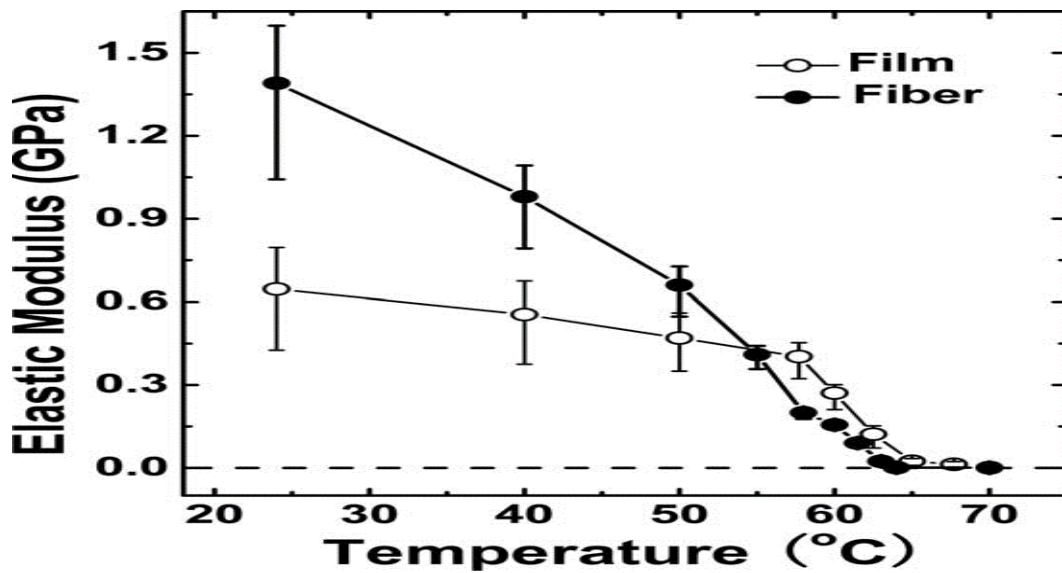
Figure 6.1. Change in elastic modulus of PEO fiber and film with temperature. Graph from [230].

The fabrication and processing of polymer fibers has been extensively studied due to the broad applicability of polymer fibers in lightweight structural materials, textiles, and device concepts, including fiber optics, sensors and smart clothing. Fabrication techniques such as electrospinning[230-232], brush on[112, 233], extrusion, injection molding[234], and vacuum transfer molding produce fibers with diameters ranging from tens of microns to tens of nanometers[235-237]. Lightweight fiber-polymer composites are increasingly preferred to traditional metal and alloy materials for aircraft, sporting goods and car bodies because of their high strength to weight ratio,

114

stability, heat and chemical resistance, and recyclability[238]. Achieving desirable mechanical properties during fiber manufacture, to a large extent, relies on empirical methods. One of the main reasons for the limited understanding needed for predictive control is that polymers are large molecules that, as a result of chain entanglements and correspondingly very high viscosities and large relaxation times, seldom reach their thermodynamic equilibrium when being processed into fibers. Studies continue to be needed to better understand the dynamics of fiber formation in order to predictably manufacture fibers with the designed material properties and dimensions.

A particularly interesting fiber formation process is the one that results in bead-on-a-string (BOS) fibers[2] (Fig. 2.1). The formation of these fibers demonstrates unusual dynamics that produce structures that while appearing stable, are actually far from thermodynamic equilibrium in terms of the BOS structures and the underlying molecular chain organization. For reference, other well-known materials are non-equilibrium materials, including steel and diamond, which are rapidly cooled or depressurized from the melt to prevent conversion to equilibrium iron and graphite phases. Polymers, due to their long chain lengths that cause chain-chain entanglements, seldom fully equilibrate even at extremely slow cooling rates.

The shape and molecular organization of the chains determines the mechanical properties of BOS fibers. Environmental changes including temperature and humidity can affect molecular organization, which should be reflected in the mechanical properties of the fiber and the thermal vibration spectrum. Also, there can be dramatic changes in bulk properties over a narrow temperature range from molecular reorganization near the crystallization temperature, glass transition temperature, and the transition temperature

from rubber to rubbery flow. It is the goal of this chapter to see if such changes are detectible with the vibrometer. The mechanical model of the spectrum (eq. 2.7) provides access to elastic modulus E which is affected by molecular organization. A successful outcome to this study is the demonstration of detectability. If successful, future studies will be devoted to an in-depth examination of the mechanics of BOS fibers to develop an understanding of the role of molecular organization in establishing the mechanical properties of the polymer materials and of BOS fibers made from these materials. In other words, the purpose of this study is to show that the vibrometer is a viable tool for the study of the material properties of polymers by sensing small changes in mechanics of BOS fibers.

6.2 Thinning dynamics of polymer liquid threads

This section reviews how polymer fibers, dynamically transform from threads of polymeric liquids into fibers, including BOS fibers. This involves discussion of rheology of polymeric liquid and molecular organization of polymers in both the liquid and solid state. BOS fibers form structures within a few seconds that appear stable and unchanging to the eye.
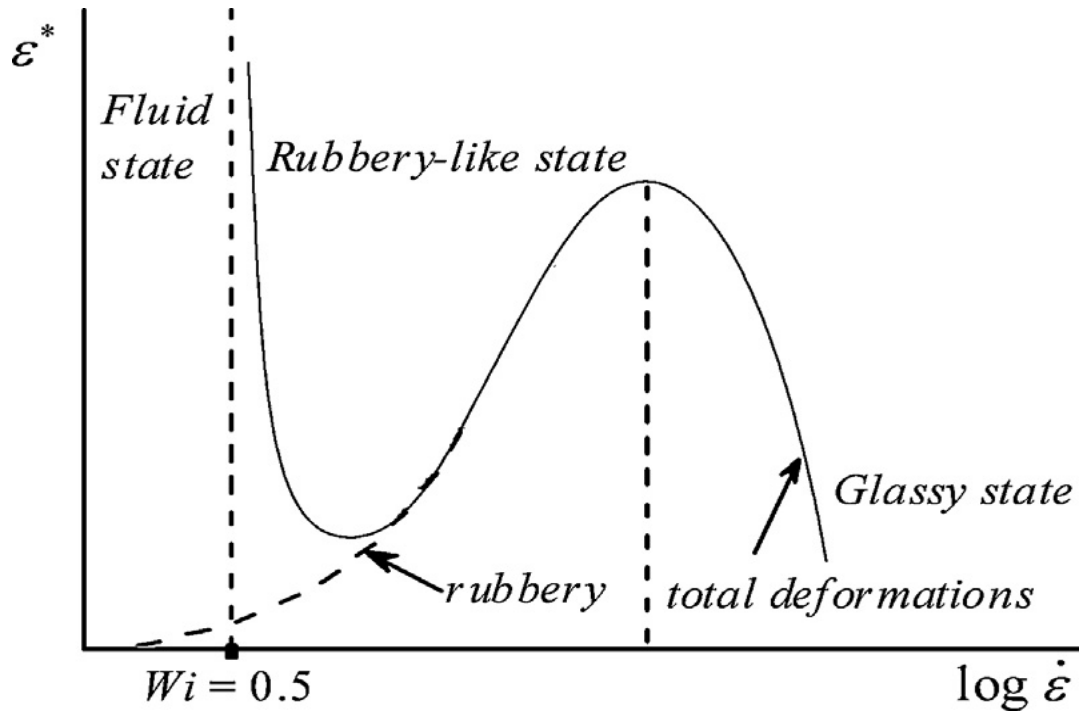
Figure 6.2. Limiting deformation as a function of the deformation rate. Graph from [243]

However, the microscopic or molecular level organization is not fully stabilized both mechanically and thermodynamically[239-242].

Fig. 6.2[243], which is a sketch of the strain dependence on strain rate for typical linear chain polymers, shows time-dependent changes in material properties and state[244-247]. The rate dependent properties can be a source of instabilities that underlie the formation of BOS fibers. The curve suggests that a liquid polymer thread changes its elastic behavior at various deformation rate. At a very low deformation rate, the elongation of the polymer thread is very high due to large viscous flow. This large and dominant viscous flow is only limited by capillary instability at this point. Deformation at higher rates brings the thread to a rubbery state that increases to a maximum value (indicated by the second dotted vertical line). At the maximum, most of the strain comes from the

deformation and almost none from the viscous flow. At even higher deformation rates the thread behaves as a glassy and barely stretchable material. The hardening of the material with strain rate is referred to as "strain hardening". During BOS formation the strain and strain rate due to capillary forces varies dramatically both in time and position between the bead and fiber regions, with the polymer chains being highly strained and extended in the fiber regions and relaxed and unstrained in the bead regions. Way to observe changes in the state of the molecular stretching throughout the BOS fiber is the overriding motivation for the development of the vibrometer.

6.2.1 Polymer properties of interest

This section considers the scope of material properties that affect the thermal vibration of BOS structures. Some of the properties that are exclusive to polymers are 1) entanglement, 2) crystallinity 3) glass transition temperatures (T_g), and 4) cross-linking. And all of these properties affect stiffness of the BOS fiber and the Young's modulus of the underlying material. The density of polymer chain entanglements also changes due to strain induced deformation[248-250]. Degree of crystallinity changes due both to heating above the melting point and with strain rate. [251-254] Glass transition temperatures also decrease
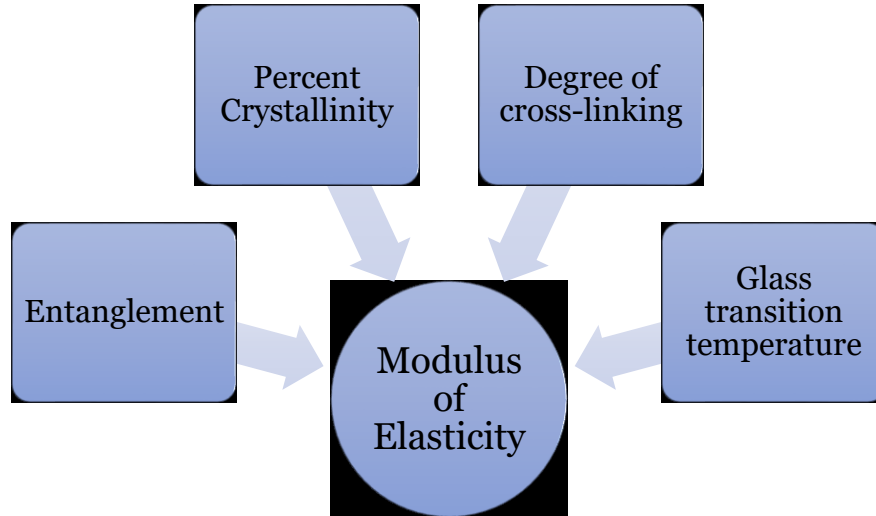
Figure 6.3. Factors that contribute to static and dynamic modulus of elasticity

with decreased thickness (of both fibers or thin films) [255-257] Cross-linking is relevant

to this study because entanglements are essentially transient crosslinks. At shorter times,

entanglements behave as crosslinks and at longer times the entanglements impede viscous

flow. All of these polymer properties affect the elastic modulus of the polymer micro-nano

structures as shown in Fig. 6.3.

6.3 BOS formation

The most comprehensive model of BOS formation is Bhat et al[2]. BOS fibers form from polymeric liquid threads when there is a specific balance among 1) viscous, 2) gravitational, 3) capillary, and 4) elastic forces. At the scale sizes of the threads in this study (under 1 mm), surface tension or capillary force dominates over gravity. Capillary force drives viscous flow that makes a thread thin into a fiber. In the absence of elastic force, the thread would ultimately thin to the point of breaking. (For a simple liquid like water, the thread will break apart into droplets.) The elastic force, together with a dramatic rise in viscosity is supplied by the entanglement and longitudinal extension of the polymer chains and their lateral confinement as the fiber thins into a decreasingly thin fiber channel. Liquid flow appears to virtually stop resulting in a stable fiber. However, after even longer times the extended polymer chains begin to relax and form droplets, separated by fiber regions where the chains are too entangled to relax. At even longer times the fiber segments can relax into smaller droplets separated by even thinner fibers. [258]

6.3.1 Features of BOS

The BOS structures are formed by brushing polymer liquid over a micropillar array (Sec. 3.3) that has either 500 µm or 1 mm edge-edge spacing (i.e. gap) between pillars. The resulting fibers have diameters of 50 -200 nm with a length to diameter aspect ratio of 2500-20000. For these aspect ratios, bending stiffnesses are 0.05-15 µN/m (by eq. 6.13). A summary of the characteristics of the fibers studied, including thermal vibration amplitudes are given in Table 6.1.

Table 6.1. Estimated characteristics of BOS fibers in this study

Parameter	Range	Note
Total length ($L = L_1 + L_2 + D$)	0.5-1.0 mm	Measured with Optical microscope
String diameter (d)	50-200 nm	Measured with SEM
Bead diameter (D)	5-20 µm	Measured with Optical microscope
Aspect ratio (L/d)	2500-20000	
Bending stiffness (k)	0.05-15 µN/m	eq. 6.13
Resonance frequency (f_0)	10-800 Hz	eq. 6.15
Amplitude of vibration (x)	4-65 nm	eq. 2.59
Q	0.5-7.0	eq. 2.70

6.3.2 Theory of BOS vibration
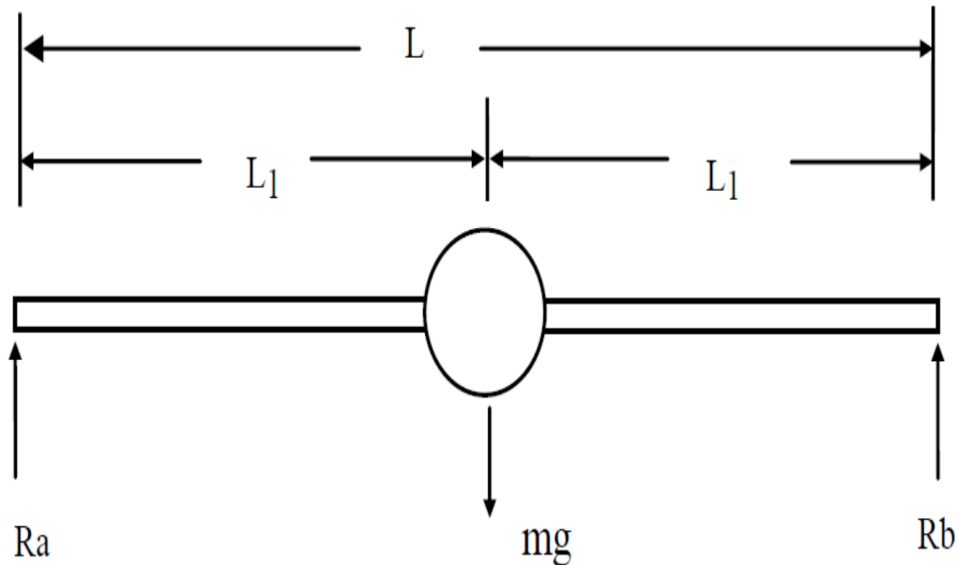
Figure 6.4. Free body diagram for beam analysis of BOS fibers.

The BOS fiber is modeled here as a spherical bead with a mass of m supported on a massless beam (or "string") of length L. The bead is located at distance of L_1 from the

121

left and L_2 from the right support. At steady state mechanical equilibrium, the weight $F = mg$ is counterbalanced by the summation of the reaction forces R_a and R_b. Net force F_T is zero based on Newton's second law

$$\sum F_T = 0 = R_a + R_b - mg \qquad (6.1)$$

where g is acceleration due to gravity. For fixed-fixed boundary conditions, the net moment at the left side of the structure is

$$\sum Moments = 0 = R_b L - mgL_1$$

which for a centered bead 2L1=L gives

$$R_b = R_a = \frac{mg}{2} \qquad (6.2)$$

The sum of the moments at the right side of the segment is

$$\sum Moments = 0 = -R_a x + mg < x - L_1 > -M \qquad (6.3)$$

Where <x-L₁> is a step function defined as

$$< x - L_1 >= \begin{cases} -0, & x < L_1 \\ x - L_1, & x \geq L_1 \end{cases} \qquad (6.4)$$

Substituting eq.6.3a into equation 6.3 yields

$$M = \left(-\frac{x}{2} + < x - L_1 > \right) mg \qquad (6.5)$$

The moment

$$M = EI \frac{d^2}{dx^2} y(x) \qquad (6.6)$$

is proportional to the second derivative of displacement where E is Young's modulus and I is the moment of inertia. Substituting eq. 6.5 into equation 6.4 gives

$$Y'' = \left(-\frac{x}{2} + < x - L_1 >\right)\left(\frac{mg}{EI}\right) \tag{6.7}$$

which after integrating twice gives

$$Y(x) = \left(-\frac{x^3}{12} + \frac{<x-L_1>^3}{6}\right)\left(\frac{mg}{EI}\right) + ax + b \tag{6.8}$$

where a and b are the undetermined coefficients that depend on the specific boundary conditions of the problem. For the fixed-fixed boundary conditions

$$Y(0) = 0, Y(L) = 0 \tag{6.9}$$

gives $b = 0$ and

$$a = \left(\frac{L^2}{16}\right)\left(\frac{mg}{EI}\right) \tag{6.10}$$

and finally

$$Y(x) = \left(-\frac{x^3}{12} + \frac{xL^2}{16} + \frac{1}{6} < x - L_1 >^3\right)\left(\frac{mg}{EI}\right) \tag{6.11}$$

for the fixed-fixed beam with concentrated applied force at its center.

The displacement of the bead at the center $x=L/2$ is

$$Y\left(\frac{L}{2}\right) = \frac{1}{48}\left(\frac{mgL^3}{EI}\right) \tag{6.12}$$

Identifying $mg=F$ then this expression has the form of Hooke's law for a linear spring of spring constant

$$k = \frac{F}{y} = \frac{48EI}{L^3} \tag{6.13}$$

Using this expression for stiffness in the eq. 2.9 for natural frequency gives

$$f_0 = \left(\frac{1}{2\pi}\right)\sqrt{\frac{k}{m}} = \left(\frac{1}{2\pi}\right)\sqrt{\frac{48EI}{mL^3}} \tag{6.14}$$

For a non-centered bead with fixed-fixed end support condition, eq. 6.15 becomes[259]

$$f_n = \frac{1}{2\pi} \times \frac{1}{L_1 L_2}\sqrt{\frac{3EIL^3}{mL_1 L_2}} \tag{6.15}$$

6.4 Vibrometry of BOS fibers
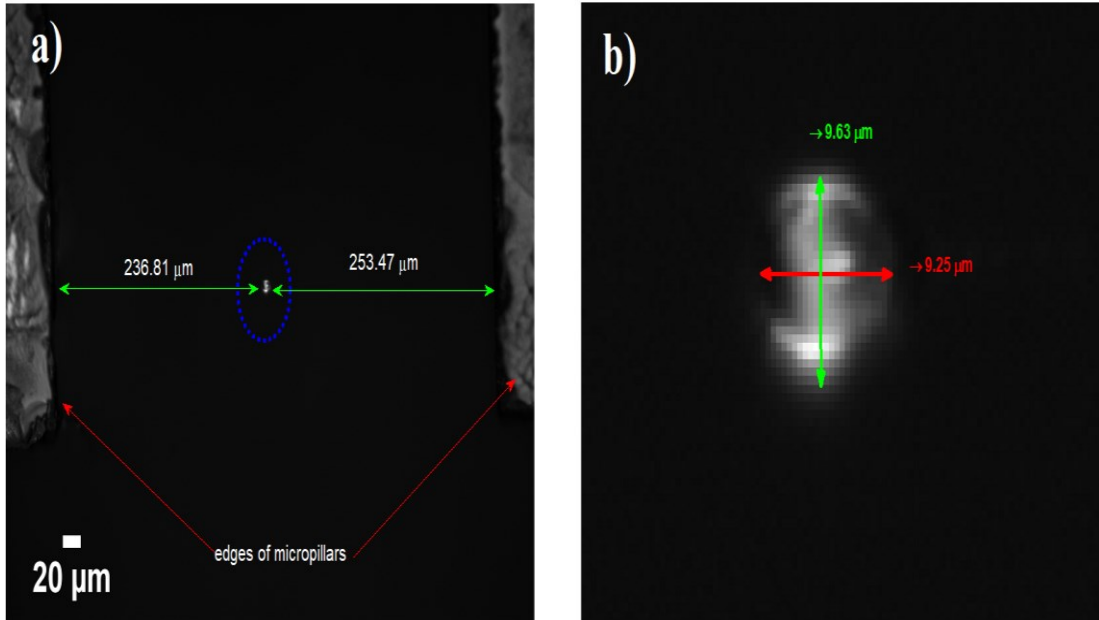
Figure 6.5. Image of BOS fiber 1. a) Location of the bead relative to pillars. b) Geometry of the elliptical bead.

Vibration spectra are monitored for each BOS fiber (Table 6.2 and Fig. 6.6) over several
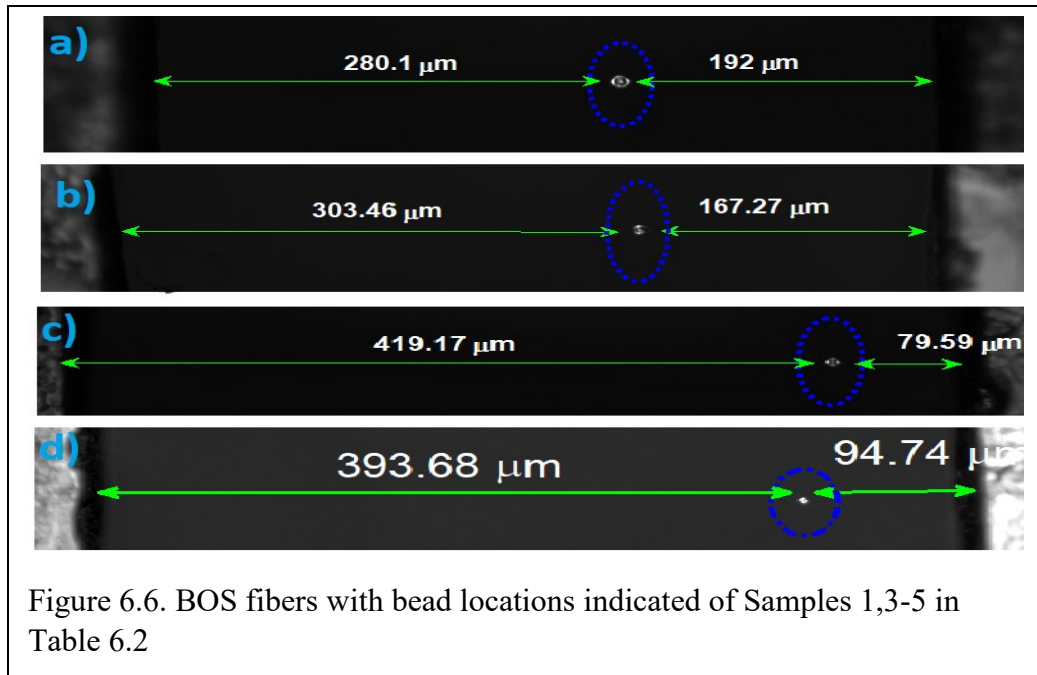
Figure 6.6. BOS fibers with bead locations indicated of Samples 1,3-5 in Table 6.2

hours. Dimensions L_1 and L_2 are measured from the edge of the left and right pillars to the

edge of the bead-fiber attachment point. The diameter of the bead D is measured both horizontally and vertically to calculate the average diameter as shown in fig. 6.5. A summary of their vibration parameters is in Table 6.2.

Table.6.2. Parameters of BOS fibers

Sample	L_1/L_2 (µm)	D (µm)	f_o (Hz)	x (nm)	Q
1	280.1/ 192.7	11.2	335.7→282.5 →259.3	56.9→65.0 →57.5	1.7→1.65 →1.61
2	236.8/ 253.4	9.4	185.9→178.2 →176.5	75.19→75 →81.1	1.4→1.38 →1.31
3	303.4/ 167.2	9.0	79.45→78.8	3.89→3.28	0.2→0.19
4	419.1/ 79.5	6.1	1089→1059 →1053→1051	24.8→30.1 →27.9→27.5	3.1→3.0→ 2.97→2.97
5	393.6/ 94.7	3.9	NA	NA	NA

→ represents shifted value after each 1 hour delay
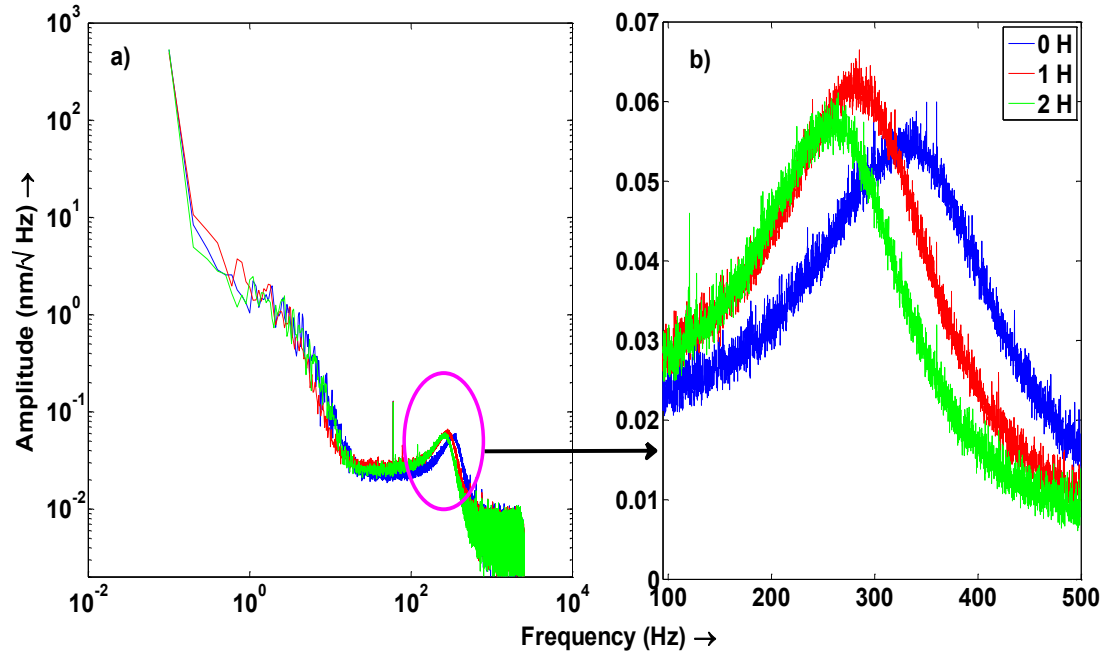
Figure 6.7. Thermal vibration of Sample 1. a) Spectra and b) close up of the spectra.

A typical BOS fiber is shown in Fig. 6.5. Its dimensions are measured within 10 minutes of fabrication (Sec. 3.3.2) and then the fiber is transferred to the vibrometer for measurement.

Fig. 6.7 shows the thermal vibration spectra for 0, 1 and 2 hrs. As shown in Table 6.2, the resonance frequency is 335.7 Hz, the amplitude is 56.9 nm and the Q is 1.7. Also shown
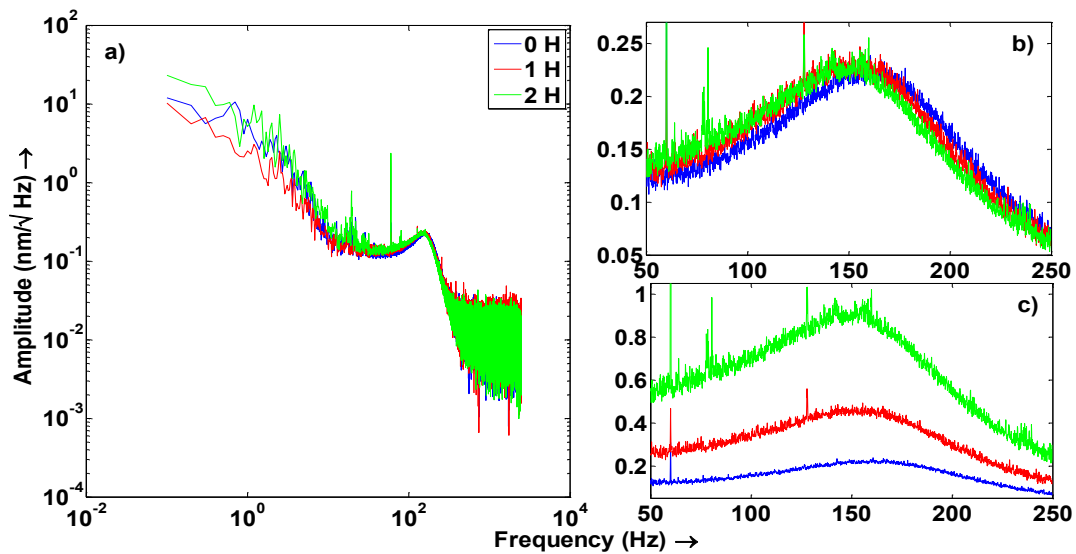
Figure 6.8. Thermal vibration of Sample 2. a) Spectra from 0-2.5 KHz. b) Spectra around the peaks and c) with offset
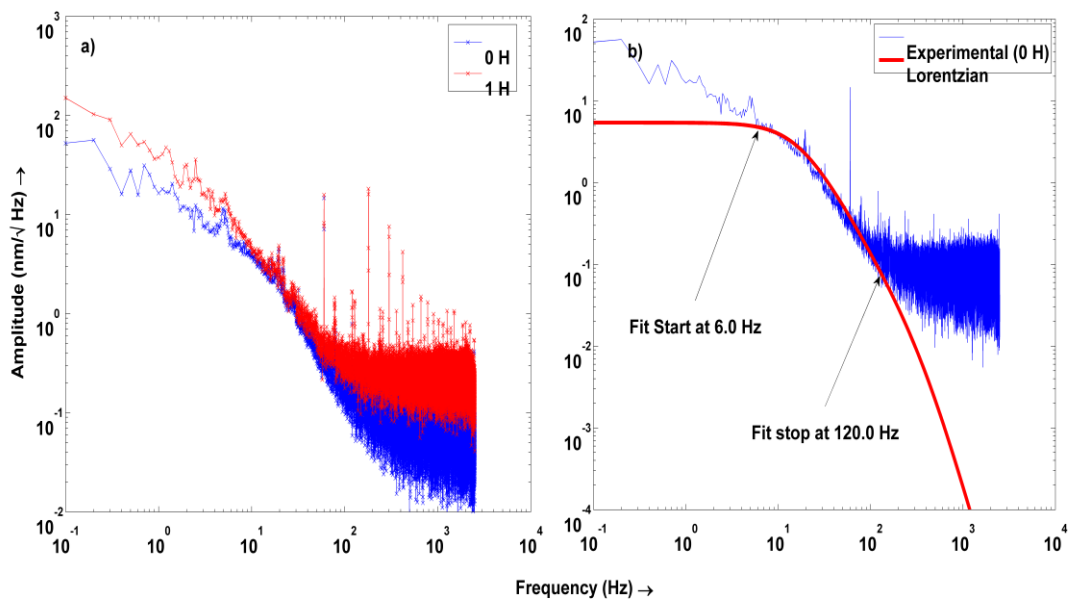
Figure 6.9. Thermal vibration spectra of Sample 3 a) full spectra and b) Lorentzian fit

128
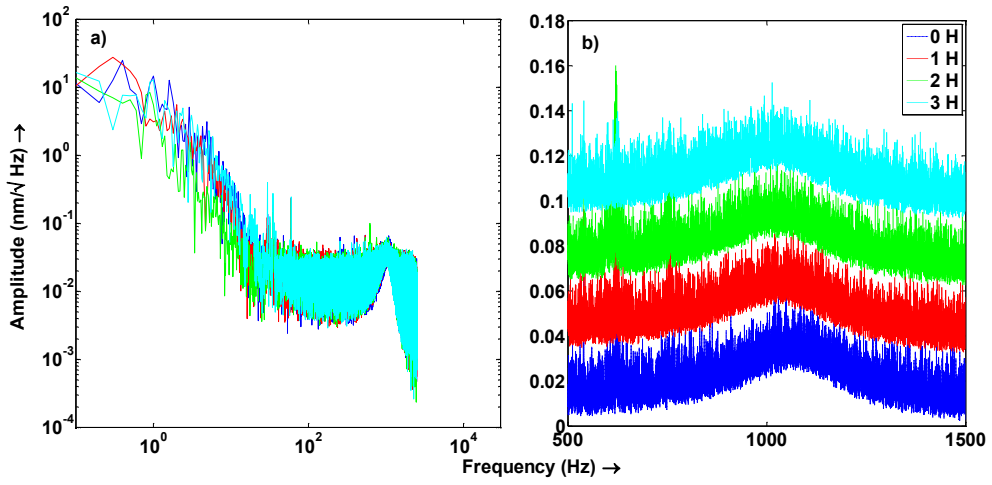
Figure 6.10. a) Thermal vibration of Sample 4. b) Spectra around resonance with offsets.
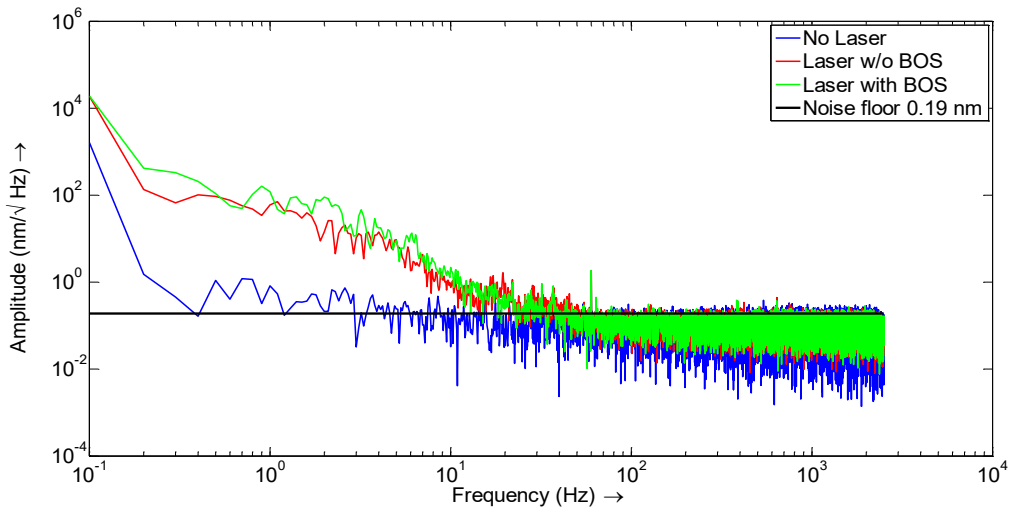
Figure 6.11. Thermal vibration of Sample 5. No resonance is detected for this structure.

in Table 2, at 1 and 2 hrs the frequency shifts downwards with only small changes in Q and amplitude.

Figs. 6.8-6.11 shows the thermal spectra of four more BOS structures as they cure at normal room temperature, humidity and pressure. These shifts could be due to numerous underlying factors that would be investigated in future studies. For instance, the resonance frequency of BOS1 changes from 335.7 Hz to 282.5 Hz. If this 53.2 Hz change is caused by a single underlying factor such elastic modulus E, then it represents a 30% reduction in the modulus (by using eq. 6.15), which is a change from 9 GPa to 4.96 GPa. Our system can detect changes in resonance frequency as low as 1.0 Hz for structures with low Q factor like this one. A 1.0 Hz change in resonance frequency can be attributed to a corresponding modulus change of 0.006 %. If we consider this 53.2 Hz change was caused by water loss, it would represent a 25.4% loss of water. The mass of the bead needed to become 0.663 pg from 0.89pg which is 0.227 pg. Similar to the elastic modulus, a 1.0 Hz resonance frequency could represent a mass loss of 0.006%. All these hypothetical numbers show the same relative change as the elastic modulus, if the resonance frequency change was due to the change in stiffness rather than water loss or elastic modulus, because the stiffness is directly proportional to the elastic modulus.

6.5 Discussion

Thermal vibration spectra of BOS fibers are measured as they go through their final stages of drying. These vibrometer measurements appear to have sufficient sensitivity to study the late stage dynamics of liquid-solid transformation of BOS fibers. Subtle time-varying changes in chain entanglement density, percent crystallization, percent water incorporated, cross-linking density (in case of a crosslinked polymer), will affect BOS

mechanical properties and could be observable as changes in the vibration spectrum, resonance frequency, amplitude of vibration and Q. Stiffness, which is a lumped element parameter is proportional to the elastic modulus, and entanglement density, glass transition temperatures, and percent crystallinity all affect modulus which is reflected in stiffness from the lumped element model. While the vibrometer can accurately detect a frequency change as low as 0.1 Hz if the Q is greater than 10, the low Q of BOS structures limits frequency resolution to 1.0 Hz. For a BOS structure with a Q of 2, a 1.0 Hz change in resonance frequency could be due to $\pm 2\%$ changes in elastic modulus or stiffness or mass loss due to water evaporation.

Table 6.3. Relative change in material properties that would cause a -1 % shift of f_0 in eq. 6.15. Specifically calculated for $f_0 = 10$ Hz and $Q = 2$

$\Delta E/E$ (%)	$\Delta k/k$ (%)	$\Delta m/m$ (%)
-2	-2	+2

6.6 Conclusion

It is important to be able to measure and understand how polymers cure and their mechanical properties evolve as the transform from liquids into solids. Additionally, the role of temperature, humidity, strain rate, etc. affect the solidification process. The development of the vibrometer appears to be a promising candidate for probing these time varying changes, and it can be applied to monitoring evolution of these properties in nanostructures and nanodevice fabrication methods. The vibrometer detects thermal vibration, including the complete instantaneous vibration spectra of nanostructures with sub-nanometer resolution.

REFERENCES

[1]   W. J. M. M. T. Shaw, "Introduction to polymer viscoelasticity," 2005.

[2]   P. P. Bhat, S. Appathurai, M. T. Harris, M. Pasquali, G. H. McKinley, and O. A. Basaran, "Formation of beads-on-a-string structures during break-up of viscoelastic filaments," *Nature Physics,* vol. 6, no. 8, pp. 625-631, Aug 2010.

[3]   C. M. Harris, A. G. Piersol, and ebrary Inc., Harris' shock and vibration handbook, 5th ed. New York: McGraw-Hill,, 2002, p. 1 v. (various pagings). [Online].

[4]   A. G. Piersol, T. L. Paez, C. M. Harris, and ebrary Inc., Harris' shock and vibration handbook, 6th ed. New York: McGraw-Hill,, 2010, p. 1 online resource. [Online].

[5]   S. Timoshenko, D. H. Young, and W. Weaver, *Vibration problems in engineering*, 4th ed. New York,: Wiley, 1974, pp. xiii, 521 p.

[6]   L. D. Landau and E. M. Lifshits, *Fluid mechanics*, 2nd ed. (Course of theoretical physics, no. 6). Oxford, England ; New York: Pergamon Press, 1987, pp. xiii, 539 p., 1 leaf of plates.

[7]   W. E. Newell, "Miniaturization of tuning forks," *Science,* vol. 161, no. 3848, pp. 1320-6, Sep 27 1968.

[8]   M. Hirata, K. Kokubun, M. Ono, and K. Nakayama, "Size effect of a quartz oscillator on its characteristics as a friction vacuum gauge," *Journal of Vacuum Science & Technology a-Vacuum Surfaces and Films,* vol. 3, no. 3, pp. 1742-1745, 1985 1985.

[9]   K. Kokubun, M. Hirata, H. Murakami, Y. Toda, and M. Ono, "A bending and stretching mode crystal-oscillator as a friction vacuum gauge," *Vacuum,* vol. 34, no. 8-9, pp. 731-735, 1984 1984.

[10]   K. Kokubun, M. Hirata, M. Ono, H. Murakami, and Y. Toda, "Unified formula describing the impedance dependence of a quartz oscillator on gas-pressure," *Journal of Vacuum Science & Technology a-Vacuum Surfaces and Films,* vol. 5, no. 4, pp. 2450-2453, Jul-Aug 1987.

[11]   K. Kokubun, M. Hirata, M. Ono, H. Murakami, and Y. Toda, "Frequency-dependence of a quartz oscillator on gas-pressure," *Journal of Vacuum Science & Technology a-Vacuum Surfaces and Films,* vol. 3, no. 6, pp. 2184-2187, 1985 1985.

[12]   H. Lamb, *Hydrodynamics*, 6th ed. New York,: Dover publications, 1945, pp. 2 p.l., vii -xv, 738 p.

[13]   F. R. Blom, S. Bouwstra, M. Elwenspoek, and J. H. J. Fluitman, "Dependence of the quality factor of micromachined silicon beam resonators on pressure and geometry," (in English), *Journal of Vacuum Science & Technology B,* vol. 10, no. 1, pp. 19-26, Jan-Feb 1992.

[14] R. A. Millikan, "Coefficients of slip in gases and the law of reflection of molecules from the surfaces of solids and liquids," *Physical Review,* vol. 21, no. 3, pp. 217-238, 1923.

[15] F. N. Hooge, "1/f noise sources," (in English), *Ieee Transactions on Electron Devices,* Article vol. 41, no. 11, pp. 1926-1935, Nov 1994.

[16] R. Kiely, "Understanding and eliminating 1/f noise," *ANALOG DEVICES Application note.*

[17] A. Yariv, P. Yeh, and A. Yariv, *Photonics : Optical electronics in modern communications*, 6th ed. (The oxford series in electrical and computer engineering). New York: Oxford University Press, 2007, pp. xii, 836 p.

[18] K. Berg-Sorensen and H. Flyvbjerg, "Power spectrum analysis for optical tweezers," *Review of Scientific Instruments,* vol. 75, no. 3, pp. 594-612, Mar 2004.

[19] E. J. G. Peterman, F. Gittes, and C. F. Schmidt, "Laser-induced heating in optical traps," *Biophysical Journal,* vol. 84, no. 2, pp. 1308-1316, Feb 2003.

[20] J. L. Hutter and J. Bechhoefer, "Calibration of atomic-force microscope tips," *Review of Scientific Instruments,* vol. 64, no. 7, pp. 1868-1873, Jul 1993.

[21] J. E. Sader, I. Larson, P. Mulvaney, and L. R. White, "Method for the calibration of atomic-force microscope cantilevers," *Review of Scientific Instruments,* vol. 66, no. 7, pp. 3789-3798, Jul 1995.

[22] A. Pralle, M. Prummer, E. L. Florin, E. H. K. Stelzer, and J. K. H. Horber, "Three-dimensional high-resolution particle tracking for optical tweezers by forward

scattered light," *Microscopy Research and Technique,* vol. 44, no. 5, pp. 378-386, Mar 1 1999.

[23]   A. Ashkin and J. M. Dziedzic, "Optical trapping and manipulation of viruses and bacteria," *Science,* vol. 235, no. 4795, pp. 1517-1520, Mar 20 1987.

[24]   S. S. Chowdhury, A. Sherehiy, C. Jarro, and R. Cohn, "Optical measurement of thermal vibration spectra to determine young's modulus of glass microfibers," in *2018 IEEE 13th Nanotechnology Materials and Devices Conference (NMDC)*, 2018, pp. 1-4.

[25]   A. Gupta, D. Akin, and R. Bashir, "Single virus particle mass detection using microresonators with nanoscale thickness," (in English), *Applied Physics Letters,* Article vol. 84, no. 11, pp. 1976-1978, Mar 2004.

[26]   T. J. Senden and W. A. Ducker, "Experimental-determination of spring constants in atomic-force microscopy," (in English), *Langmuir,* Letter vol. 10, no. 4, pp. 1003-1004, Apr 1994.

[27]   G. Y. Chen, R. J. Warmack, T. Thundat, D. P. Allison, and A. Huang, "Resonance response of scanning force microscopy cantilevers," *Review of Scientific Instruments,* vol. 65, no. 8, pp. 2532-2537, Aug 1994.

[28]   J. M. Neumeister and W. A. Ducker, "Lateral, normal, and longitudinal spring constants of atomic-force microscopy cantilevers," *Review of Scientific Instruments,* vol. 65, no. 8, pp. 2527-2531, Aug 1994.

[29]   Y. Q. Li, N. J. Tao, J. Pan, A. A. Garcia, and S. M. Lindsay, "Direct measurement of interaction forces between colloidal particles using the scanning force microscope," *Langmuir,* vol. 9, no. 3, pp. 637-641, Mar 1993.

[30] J. P. Cleveland, S. Manne, D. Bocek, and P. K. Hansma, "A nondestructive method for determining the spring constant of cantilevers for scanning force microscopy," (in English), *Review of Scientific Instruments,* Article vol. 64, no. 2, pp. 403-405, Feb 1993.

[31] L. P. Ghislain, N. A. Switz, and W. W. Webb, "Measurement of small forces using an optical trap," *Review of Scientific Instruments,* vol. 65, no. 9, pp. 2762-2768, Sep 1994.

[32] L. P. Ghislain and W. W. Webb, "Scanning-force microscope based on an optical trap," *Optics Letters,* vol. 18, no. 19, pp. 1678-1680, Oct 1 1993.

[33] W. J. Greenleaf, M. T. Woodside, E. A. Abbondanzieri, and S. M. Block, "Passive all-optical force clamp for high-resolution laser trapping," *Physical Review Letters,* vol. 95, no. 20, Nov 11 2005, Art. no. 208102.

[34] A. T. O'Neil and M. J. Padgett, "Axial and lateral trapping efficiency of laguerre-gaussian modes in inverted optical tweezers," *Optics Communications,* vol. 193, no. 1-6, pp. 45-50, Jun 15 2001.

[35] W. H. Wright, G. J. Sonek, and M. W. Berns, "Radiation trapping forces on microspheres with optical tweezers," *Applied Physics Letters,* vol. 63, no. 6, pp. 715-717, Aug 9 1993.

[36] W. H. Wright, G. J. Sonek, and M. W. Berns, "Parametric study of the forces on microspheres held by optical tweezers," *Applied Optics,* vol. 33, no. 9, pp. 1735-1748, Mar 20 1994.

[37] K. Svoboda and S. M. Block, "Optical trapping of metallic rayleigh particles," (in English), *Optics Letters,* vol. 19, no. 13, pp. 930-932, Jul 1 1994.

[38] K. Svoboda and S. M. Block, "Biological applications of optical forces," *Annual Review of Biophysics and Biomolecular Structure,* vol. 23, pp. 247-285, 1994 1994.

[39] A. D. Mehta, J. T. Finer, and J. A. Spudich, "Use of optical traps in single-molecule study of nonprocessive biological motors," *Molecular Motors and the Cytoskeleton, Pt B,* vol. 298, pp. 436-459, 1998 1998.

[40] A. D. Mehta, M. Rief, J. A. Spudich, D. A. Smith, and R. M. Simmons, "Single-molecule biomechanics with optical methods," *Science,* vol. 283, no. 5408, pp. 1689-1695, Mar 12 1999.

[41] S. C. Kuo, "Using optics to measure biological forces and mechanics," *Traffic,* vol. 2, no. 11, pp. 757-763, Nov 2001.

[42] A. Ishijima and T. Yanagida, "Single molecule nanobioscience," *Trends in Biochemical Sciences,* vol. 26, no. 7, pp. 438-444, Jul 2001.

[43] Y. Ishii, A. Ishijima, and T. Yanagida, "Single molecule nanomanipulation of biomolecules," *Trends in Biotechnology,* vol. 19, no. 6, pp. 211-216, Jun 2001.

[44] S. Jeney, E. L. Florin, and J. K. Horber, "Use of photonic force microscopy to study single-motor-molecule mechanics," *Methods in molecular biology (Clifton, N.J.),* vol. 164, pp. 91-108, 2001 2001.

[45] C. Bustamante, S. B. Smith, J. Liphardt, and D. Smith, "Single-molecule studies of DNA mechanics," *Current Opinion in Structural Biology,* vol. 10, no. 3, pp. 279-285, Jun 2000.

[46] C. Bustamante, Z. Bryant, and S. B. Smith, "Ten years of tension: Single-molecule DNA mechanics," *Nature,* vol. 421, no. 6921, pp. 423-427, Jan 23 2003.

[47] T. T. Perkins, S. R. Quake, D. E. Smith, and S. Chu, "Relaxation of a single DNA molecule observed by optical microscopy," *Science,* vol. 264, no. 5160, pp. 822-826, May 6 1994.

[48] M. D. Wang, H. Yin, R. Landick, J. Gelles, and S. M. Block, "Stretching DNA with optical tweezers," *Biophysical Journal,* vol. 72, no. 3, pp. 1335-1346, Mar 1997.

[49] J. Liphardt, B. Onoa, S. B. Smith, I. Tinoco, and C. Bustamante, "Reversible unfolding of single rna molecules by mechanical force," *Science,* vol. 292, no. 5517, pp. 733-737, Apr 27 2001.

[50] A. Janshoff, M. Neitzert, Y. Oberdorfer, and H. Fuchs, "Force spectroscopy of molecular systems - single molecule spectroscopy of polymers and biomolecules," *Angewandte Chemie-International Edition,* vol. 39, no. 18, pp. 3213-3237, 2000 2000.

[51] J. C. Crocker and D. G. Grier, "When like charges attract: The effects of geometrical confinement on long-range colloidal interactions," *Physical Review Letters,* vol. 77, no. 9, pp. 1897-1900, Aug 26 1996.

[52] L. A. Hough and H. D. Ou-Yang, "Correlated motions of two hydrodynamically coupled particles confined in separate quadratic potential wells," *Physical Review E,* vol. 65, no. 2, Feb 2002, Art. no. 021906.

[53] P. T. Korda, M. B. Taylor, and D. G. Grier, "Kinetically locked-in colloidal transport in an array of optical tweezers," *Physical Review Letters,* vol. 89, no. 12, Sep 16 2002, Art. no. 128301.

[54] H. Lowen, "Colloidal soft matter under external control," *Journal of Physics-Condensed Matter,* vol. 13, no. 24, pp. R415-R432, Jun 18 2001.

[55] H. J. Buchner, H. Stiebig, V. Mandryka, E. Bunte, and G. Jager, "An optical standing-wave interferometer for displacement measurements," (in English), *Measurement Science and Technology,* Article vol. 14, no. 3, pp. 311-316, Mar 2003, Art. no. Pii s0957-0233(03)54197-2.

[56] L. Y. Chen, J. Y. Lee, H. S. Chang, and Y. Yang, "Development of an angular displacement measurement by birefringence heterodyne interferometry," (in English), *Smart Science,* Article vol. 3, no. 4, pp. 188-192, Dec 2015.

[57] C. C. Hsu, H. Chen, H. Y. Tseng, S. C. Lan, and J. Lin, "High displacement resolution encoder by using triple grating combination interferometer," (in English), *Optics and Laser Technology,* Article vol. 105, pp. 221-228, Sep 2018.

[58] L. P. Yan, B. Y. Chen, Z. Q. Chen, J. D. Xie, E. Z. Zhang, and S. H. Zhang, "Phase-modulated dual-homodyne interferometer without periodic nonlinearity," (in English), *Measurement Science and Technology,* Article vol. 28, no. 11, p. 7, Nov 2017, Art. no. 115006.

[59] L. P. Yan *et al.*, "Precision pgc demodulation for homodyne interferometer modulated with a combined sinusoidal and triangular signal," (in English), *Optics Express,* Article vol. 26, no. 4, pp. 4818-4831, Feb 2018.

[60] L. P. Yan, B. Y. Chen, and B. Wang, "A differential michelson interferometer with orthogonal single frequency laser for nanometer displacement measurement," (in English), *Measurement Science and Technology,* Article vol. 28, no. 4, p. 7, Apr 2017, Art. no. 045001.

[61] L. Lipiainen, K. Kokkonen, and M. Kaivola, "Homodyne full-field interferometer for measuring dynamic surface phenomena in microstructures," (in English), *Optics and Lasers in Engineering,* Article vol. 88, pp. 178-183, Jan 2017.

[62] Q. Lv *et al.*, "Simple and compact grating-based heterodyne interferometer with the littrow configuration for high-accuracy and long-range measurement of two-dimensional displacement," (in English), *Applied Optics,* Article vol. 57, no. 31, pp. 9455-9463, Nov 2018.

[63] H. J. Fu, R. D. Ji, P. C. Hu, Y. Wang, G. L. Wu, and J. B. Tan, "Measurement method for nonlinearity in heterodyne laser interferometers based on double-channel quadrature demodulation," (in English), *Sensors,* Article vol. 18, no. 9, p. 9, Sep 2018, Art. no. 2768.

[64] J. Perea, B. Libbey, and G. Nehmetallah, "Multiaxis heterodyne vibrometer for simultaneous observation of 5 degrees of dynamic freedom from a single beam," (in English), *Optics Letters,* Article vol. 43, no. 13, pp. 3120-3123, Jul 2018.

[65] J. G. Chen, T. M. Adams, H. Sun, E. S. Bell, and O. Buyukozturk, "Camera-based vibration measurement of the world war i memorial bridge in portsmouth, new hampshire," (in English), *Journal of Structural Engineering,* Article vol. 144, no. 11, p. 19, Nov 2018, Art. no. 04018207.

[66] Y. P. Zhao, J. Y. Liu, S. J. Guo, and T. J. Li, "Measuring frequency of one-dimensional vibration with video camera using electronic rolling shutter," (in English), *Optical Engineering,* Article vol. 57, no. 4, p. 8, Apr 2018, Art. no. 043104.

[67]   I. Weerasekera, G. Balyasin, W. H. Zhu, and G. Liu, "Lens-less psd measurement of flexible link deflection," (in English), *Measurement Science and Technology,* Article vol. 30, no. 1, p. 11, Jan 2019, Art. no. 015003.

[68]   S. B. Pal, A. Helder, B. Roy, and A. Banerjee, "Measurement of probe displacement to the thermal resolution limit in photonic force microscopy using a miniature quadrant photodetector," (in English), *Review of Scientific Instruments,* Article vol. 83, no. 2, p. 12, Feb 2012, Art. no. 023108.

[69]   R. E. Thompson, D. R. Larson, and W. W. Webb, "Precise nanometer localization analysis for individual fluorescent probes," *Biophysical Journal,* vol. 82, no. 5, pp. 2775-2783, May 2002.

[70]   M. K. Cheezum, W. F. Walker, and W. H. Guilford, "Quantitative comparison of algorithms for tracking single fluorescent particles," *Biophysical Journal,* vol. 81, no. 4, pp. 2378-2388, Oct 2001.

[71]   J. C. Crocker and D. G. Grier, "Methods of digital video microscopy for colloidal studies," *Journal of Colloid and Interface Science,* vol. 179, no. 1, pp. 298-310, Apr 15 1996.

[72]   M. Keller, J. Schilling, and E. Sackmann, "Oscillatory magnetic bead rheometer for complex fluid microrheometry," *Review of Scientific Instruments,* vol. 72, no. 9, pp. 3626-3634, Sep 2001.

[73]   C. Gosse and V. Croquette, "Magnetic tweezers: Micromanipulation and force measurement at the molecular level," *Biophysical Journal,* vol. 82, no. 6, pp. 3314-3329, Jun 2002.

[74]   H. Andersson, "Position sensitive detectors - device technology and applications in

spectroscopy

", 2008.

[75]   A. Labuda *et al.*, "Static and dynamic calibration of torsional spring constants of
cantilevers," *Review of Scientific Instruments,* vol. 89, no. 9, Sep 2018, Art. no.
093701.

[76]   M. J. Lang, P. M. Fordyce, and S. M. Block, "Combined optical trapping and
single-molecule fluorescence," *Journal of biology,* vol. 2, no. 1, pp. 6-6, 2003 2003.

[77]   A. Rohrbach, H. Kress, and E. H. K. Stelzer, "Three-dimensional tracking of small
spheres in focused laser beams: Influence of the detection angular aperture," *Optics
Letters,* vol. 28, no. 6, pp. 411-413, Mar 15 2003.

[78]   H. He, N. R. Heckenberg, and H. Rubinszteindunlop, "Optical-particle trapping
with higher-order doughnut beams produced using high-efficiency computer-
generated holograms," *Journal of Modern Optics,* vol. 42, no. 1, pp. 217-223, Jan
1995.

[79]   A. Makynen, J. Kostamovaara, and R. Myllyla, "Laser-radar-based 3-dimensional
sensor for teaching robot paths," *Optical Engineering,* vol. 34, no. 9, pp. 2596-
2602, Sep 1995.

[80]   J. Y. Zhang, M. Ming, Y. Z. Jiang, H. Z. Duan, and H. C. Yeh, "Inter-satellite laser
link acquisition with dual-way scanning for space advanced gravity measurements
mission," *Review of Scientific Instruments,* vol. 89, no. 6, Jun 2018, Art. no.
064501.

[81]   G. Marola, D. Santerini, and G. Prati, "Stability analysis of direct-detection cooperative optical beam tracking," *Ieee Transactions on Aerospace and Electronic Systems,* vol. 25, no. 3, pp. 325-334, May 1989.

[82]   A. Vera-Marquina, A. Diaz-sanchez, J. Rocha-Pérez, D. Berman-Mendoza, and I. Padilla, *Quadrant photodiode for electronic processing*. 2009.

[83]   L. M. Manojlovic, "Resolution limit of the quadrant photodetector," *Optik,* vol. 127, no. 19, pp. 7631-7634, 2016.

[84]   L. M. Manojlović, "Quadrant photodiode circuitry for high precision displacement measurement," ed.

[85]   P. Grivet, N. Bloembergen, and United States. Office of Naval Research., *Quantum electronics; proceedings of the third international congress.* 1964.

[86]   S. F. Jacobs, "Optical heterodyne (coherent) detection," vol. 56, no. 3, pp. 235-245, 1988.

[87]   A. B. Rogalski, Z., "Detection of optical radiation," *Bulletin of the Polish Acameny of Science,* vol. 52, no. 1, pp. 43-66, 2004.

[88]   K. Visscher and S. M. Block, "Versatile optical traps with feedback control," *Molecular Motors and the Cytoskeleton, Pt B,* vol. 298, pp. 460-489, 1998 1998.

[89]   K. Visscher, S. P. Gross, and S. M. Block, "Construction of multiple-beam optical traps with nanometer-resolution position sensing," *Ieee Journal of Selected Topics in Quantum Electronics,* vol. 2, no. 4, pp. 1066-1076, Dec 1996.

[90]   W. Denk and W. W. Webb, "Optical measurement of picometer displacements of transparent microscopic objects," *Applied Optics,* vol. 29, no. 16, pp. 2382-2391, Jun 1 1990.

[91] K. Svoboda, C. F. Schmidt, B. J. Schnapp, and S. M. Block, "Direct observation of kinesin stepping by optical trapping interferometry," *Nature,* vol. 365, no. 6448, pp. 721-727, Oct 21 1993.

[92] A. Rohrbach and E. H. K. Stelzer, "Three-dimensional position detection of optically trapped dielectric particles," *Journal of Applied Physics,* vol. 91, no. 8, pp. 5474-5488, Apr 15 2002.

[93] M. W. Allersma, F. Gittes, M. J. deCastro, R. J. Stewart, and C. F. Schmidt, "Two-dimensional tracking of ncd motility by back focal plane interferometry," *Biophysical Journal,* vol. 74, no. 2, pp. 1074-1085, Feb 1998.

[94] F. Gittes and C. F. Schmidt, "Interference model for back-focal-plane displacement detection in optical tweezers," *Optics Letters,* vol. 23, no. 1, pp. 7-9, Jan 1 1998.

[95] F. Gittes and C. F. Schmidt, "Back-focal-plane detection of force and motion in optical traps," *Biophysical Journal,* vol. 74, no. 2, pp. A183-A183, Feb 1998.

[96] J. E. Sader and L. White, "Theoretical-analysis of the static deflection of plates for atomic-force microscope applications," *Journal of Applied Physics,* vol. 74, no. 1, pp. 1-9, Jul 1 1993.

[97] T. Thundat, R. J. Warmack, G. Y. Chen, and D. P. Allison, "Thermal and ambient-induced deflections of scanning force microscope cantilevers," *Applied Physics Letters,* vol. 64, no. 21, pp. 2894-2896, May 23 1994.

[98] R. J. Warmack, X. Y. Zheng, T. Thundat, and D. P. Allison, "Friction effects in the deflection of atomic-force microscope cantilevers," *Review of Scientific Instruments,* vol. 65, no. 2, pp. 394-399, Feb 1994.

[99]   M. V. Salapaka, H. S. Bergh, J. Lai, A. Majumdar, and E. McFarland, "Multi-mode noise analysis of cantilevers for scanning probe microscopy," *Journal of Applied Physics,* vol. 81, no. 6, pp. 2480-2487, Mar 15 1997.

[100]   J. E. Sader, "Frequency response of cantilever beams immersed in viscous fluids with applications to the atomic force microscope," *Journal of Applied Physics,* vol. 84, no. 1, pp. 64-76, Jul 1 1998.

[101]   M. B. Viani, T. E. Schaffer, A. Chand, M. Rief, H. E. Gaub, and P. K. Hansma, "Small cantilevers for force spectroscopy of single molecules," *Journal of Applied Physics,* vol. 86, no. 4, pp. 2258-2262, Aug 15 1999.

[102]   M. B. Viani *et al.*, "Fast imaging and fast force spectroscopy of single biopolymers with a new atomic force microscope designed for small cantilevers," *Review of Scientific Instruments,* vol. 70, no. 11, pp. 4300-4303, Nov 1999.

[103]   A. Chand, M. B. Viani, T. E. Schaffer, and P. K. Hansma, "Microfabricated small metal cantilevers with silicon tip for atomic force microscopy," *Journal of Microelectromechanical Systems,* vol. 9, no. 1, pp. 112-116, Mar 2000.

[104]   A. Rohrbach and E. H. K. Stelzer, "Trapping forces, force constants, and potential depths for dielectric spheres in the presence of spherical aberrations," *Applied Optics,* vol. 41, no. 13, pp. 2494-2507, May 1 2002.

[105]   E. Fallman and O. Axner, "Influence of a glass-water interface on the on-axis trapping of micrometer-sized spherical objects by optical tweezers," *Applied Optics,* vol. 42, no. 19, pp. 3915-3926, Jul 1 2003.

[106] A. van der Horst and N. R. Forde, "Power spectral analysis for optical trap stiffness calibration from high-speed camera position detection with limited bandwidth," *Optics Express,* vol. 18, no. 8, pp. 7670-7677, 2010/04/12 2010.

[107] A. Yoshida and T. Asakura, "A simple technique for quickly measuring the spot size of gaussian laser beams," *Optics & Laser Technology,* vol. 8, no. 6, pp. 273-274, 12// 1976.

[108] P. K. Gupta and S. Bhargava, "An experiment with gaussian laser-beams," (in English), *American Journal of Physics,* vol. 56, no. 6, pp. 563-564, Jun 1988.

[109] N. A. Riza and D. Jorgesen, "Minimally invasive optical beam profiler," (in English), *Optics Express,* vol. 12, no. 9, pp. 1892-1901, May 3 2004.

[110] A. B. O. M. L. A. C. J. A. D. P. M. M. M. O. M. D. I. Castillo, "New method to characterize gaussian beams," *Proc. SPIE* vol. 8011, 2011.

[111] A. H. Firester, M. E. Heller, and P. Sheng, "Knife-edge scanning measurements of subwavelength focused light-beams," (in English), *Applied Optics,* vol. 16, no. 7, pp. 1971-1974, 1977.

[112] J. M. Rathfon, M. Yan, J. F. Berret, and R. W. Cohn, "Self-assembled nems for pn force detection," in *2011 11th IEEE International Conference on Nanotechnology*, 2011, pp. 172-175.

[113] H. K. Huh, S. Jung, K. W. Seo, and S. J. Lee, "Role of polymer concentration and molecular weight on the rebounding behaviors of polymer solution droplet impacting on hydrophobic surfaces," *Microfluidics and Nanofluidics,* vol. 18, no. 5-6, pp. 1221-1232, May 2015.

[114] X. J. Yan, W. W. Carr, and H. M. Dong, "Drop-on-demand drop formation of polyethylene oxide solutions," *Physics of Fluids,* vol. 23, no. 10, Oct 2011, Art. no. 107101.

[115] D. Willmer, K. A. Baldwin, C. Kwartnik, and D. J. Fairhurst, "Growth of solid conical structures during multistage drying of sessile poly(ethylene oxide) droplets," *Physical Chemistry Chemical Physics,* vol. 12, no. 16, pp. 3998-4004, 2010 2010.

[116] L. Q. Chen, Y. G. Wang, X. Y. Peng, Q. Zhu, and K. Zhang, "Impact dynamics of aqueous polymer droplets on superhydrophobic surfaces," *Macromolecules,* vol. 51, no. 19, pp. 7817-7827, Oct 2018.

[117] W. Du, T. T. Fu, Q. D. Zhang, C. Y. Zhu, Y. G. Ma, and H. Z. Li, "Breakup dynamics for droplet formation in a flow-focusing device: Rupture position of viscoelastic thread from matrix," *Chemical Engineering Science,* vol. 153, pp. 255-269, Oct 2016.

[118] Y. S. Cai and M. Gevelber, "Analysis of bending region physics in determining electrospun fiber diameter: Effect of relative humidity on evaporation and force balance," (in English), *Journal of Materials Science,* Article vol. 52, no. 5, pp. 2605-2627, Mar 2017.

[119] Y. Cai and M. Gevelber, "The effect of relative humidity and evaporation rate on electrospinning: Fiber diameter and measurement for control implications," *Journal of Materials Science,* vol. 48, no. 22, pp. 7812-7826, Nov 2013.

[120] K. A. Baldwin, M. Granjard, D. I. Willmer, K. Sefiane, and D. J. Fairhurst, "Drying and deposition of poly(ethylene oxide) droplets determined by peclet number," *Soft Matter,* vol. 7, no. 17, pp. 7819-7826, 2011 2011.

[121] M. J. de Ruijter, T. D. Blake, and J. De Coninck, "Dynamic wetting studied by molecular modeling simulations of droplet spreading," *Langmuir,* vol. 15, no. 22, pp. 7836-7847, Oct 26 1999.

[122] A. V. Oppenheim and R. W. Schafer, *Discrete-time signal processing* (Prentice-hall signal processing series). Englewood Cliffs, N.J.: Prentice Hall, 1989.

[123] A. Farina, *Simultaneous measurement of impulse response and distortion with a swept-sine technique. Audio engineering society convention 108, audio engineering society*. 2000.

[124] H.-H. Kuo, *White noise distribution theory* (Probability and stochastics series). Boca Raton: CRC Press, 1996, p. 378 p.

[125] D. Royer and E. Dieulesaint, "Optical measurements of displacements of amplitude 10-4 to 10-2 anfstrom - application to elastic-waves," *Revue De Physique Appliquee,* vol. 24, no. 8, pp. 833-846, Aug 1989.

[126] M. Celik, R. Hamid, U. Kuetgens, and A. Yacoot, "Picometre displacement measurements using a differential fabry-perot optical interferometer and an x-ray interferometer," *Measurement Science and Technology,* vol. 23, no. 8, Aug 2012, Art. no. 085901.

[127] R. Barrett, "New system for optical displacement measurement," *Journal of Physics E-Scientific Instruments,* vol. 3, no. 11, pp. 895-&, 1970.

[128] M. Tanaka and K. Nakayama, "A new optical interferometer for absolute measurement of linear displacement in the subnanometer range," *Japanese Journal of Applied Physics Part 2-Letters,* vol. 22, no. 4, pp. L233-L235, 1983.

[129] S. Kamimura, "Direct measurement of nanometric displacement under an optical microscope," *Applied Optics,* vol. 26, no. 16, pp. 3425-3427, Aug 1987.

[130] M. Imai and K. Kawakita, "Optical-heterodyne displacement measurement using a frequency-ramped laser diode," *Optics Communications,* vol. 78, no. 2, pp. 113-117, Aug 1990.

[131] T. Fujii, M. Suzuki, M. Yamaguchi, R. Kawaguchi, H. Yamada, and K. Nakayama, "Three-dimensional displacement measurement of a tube scanner for a scanning tunneling microscope by optical interferometer," *Nanotechnology,* vol. 6, no. 4, pp. 121-126, Oct 1995.

[132] N. Takahashi, S. Kakuma, and R. Ohba, "Active heterodyne interferometric displacement measurement using optical feedback effects of laser diodes," *Optical Engineering,* vol. 35, no. 3, pp. 802-807, Mar 1996.

[133] R. M. Simmons, J. T. Finer, S. Chu, and J. A. Spudich, "Quantitative measurements of force and displacement using an optical trap," *Biophysical Journal,* vol. 70, no. 4, pp. 1813-1822, Apr 1996.

[134] H. M. Wang, "A simple optical displacement sensor utilizing dual-channel angle-limited integrated scattering measurements," *Journal of Modern Optics,* vol. 43, no. 11, pp. 2279-2288, Nov 1996.

[135] I. Liu, L. S. Yang, G. Y. Wang, and Z. Z. Xu, "Micro displacement measurement with the axial response curve of fiber-optical confocal scanning microscope," *Optik,* vol. 111, no. 7, pp. 315-317, 2000.

[136] S. Nakadate, T. Tokudome, and M. Shibuya, "Displacement measurement of a grating using moire modulation of an optical spectrum," *Measurement Science and Technology,* vol. 15, no. 8, pp. 1462-1466, Aug 2004, Art. no. Pii s0957-0233(04)74182-x.

[137] W. Wang *et al.*, "Optical vortex metrology for nanometric speckle displacement measurement," *Optics Express,* vol. 14, no. 1, pp. 120-127, Jan 2006.

[138] F. Chen *et al.*, "Nanoscale displacement measurement in a variable-air-gap optical waveguide," *Applied Physics Letters,* vol. 88, no. 16, Apr 2006, Art. no. 161111.

[139] M. H. De la Torre-Ibarra, P. D. Ruiz, and J. M. Huntley, "Double-shot depth-resolved displacement field measurement using phase-contrast spectral optical coherence tomography," *Optics Express,* vol. 14, no. 21, pp. 9643-9656, Oct 2006.

[140] J. Y. Lee, H. Y. Chen, C. C. Hsu, and C. C. Wu, "Optical heterodyne grating interferometry for displacement measurement with subnanometric resolution," *Sensors and Actuators a-Physical,* vol. 137, no. 1, pp. 185-191, Jun 2007.

[141] F. Xie, J. Y. Ren, Z. M. Chen, and Q. B. Feng, "Vibration-displacement measurements with a highly stabilised optical fiber michelson interferometer system," *Optics and Laser Technology,* vol. 42, no. 1, pp. 208-213, Feb 2010.

[142] A. Ya'akobovitz, D. Copic, J. D. Beroz, and A. J. Hart, "Nanoscale displacement measurement of microdevices via interpolation-based edge tracking of optical

images," *Journal of Micromechanics and Microengineering,* vol. 23, no. 4, Apr 2013, Art. no. 045004.

[143] H. X. Sun, Z. L. Liu, K. Liu, R. G. Yang, J. X. Zhang, and J. R. Gao, "Experimental demonstration of a displacement measurement of an optical beam beyond the quantum noise limit," *Chinese Physics Letters,* vol. 31, no. 8, Aug 2014, Art. no. 084202.

[144] C. A. J. Putman, B. G. Degrooth, N. F. Vanhulst, and J. Greve, "A theoretical comparison between interferometric and optical beam deflection technique for the measurement of cantilever displacement in afm," *Ultramicroscopy,* vol. 42, pp. 1509-1513, Jul 1992.

[145] P. J. Cumpson, P. Zhdan, and J. Hedley, "Calibration of afm cantilever stiffness: A microfabricated array of reflective springs," *Ultramicroscopy,* vol. 100, no. 3-4, pp. 241-251, Aug 2004.

[146] S. Chu, J. E. Bjorkholm, A. Ashkin, and A. Cable, "Experimental-observation of optically trapped atoms," *Physical Review Letters,* vol. 57, no. 3, pp. 314-317, Jul 21 1986.

[147] A. Ashkin, J. M. Dziedzic, J. E. Bjorkholm, and S. Chu, "Observation of a single-beam gradient force optical trap for dielectric particles," *Optics Letters,* vol. 11, no. 5, pp. 288-290, May 1986.

[148] J. E. Bruce *et al.*, "Trapping, detection, and mass measurement of individual ions in a fourier-transform ion-cyclotron resonance mass-spectrometer," *Journal of the American Chemical Society,* vol. 116, no. 17, pp. 7839-7847, Aug 24 1994.

[149] F. Liu and M. Hossein-Zadeh, "Mass sensing with optomechanical oscillation," *Ieee Sensors Journal,* vol. 13, no. 1, pp. 146-147, Jan 2013.

[150] B. Ilic, S. Krylov, and H. G. Craighead, "Young's modulus and density measurements of thin atomic layer deposited films using resonant nanomechanics," *Journal of Applied Physics,* vol. 108, no. 4, Aug 2010, Art. no. 044317.

[151] S. Xu, O. Rezvanian, and M. A. Zikry, "Electrothermomechanical modeling and analyses of carbon nanotube polymer composites," *Journal of Engineering Materials and Technology-Transactions of the Asme,* vol. 135, no. 2, Apr 2013, Art. no. 021014.

[152] M. R. Maschmann, G. J. Ehlert, S. Tawfick, A. J. Hart, and J. W. Baur, "Continuum analysis of carbon nanotube array buckling enabled by anisotropic elastic measurements and modeling," *Carbon,* vol. 66, pp. 377-386, Jan 2014.

[153] E. Ruiz and F. Trochu, "Thermomechanical properties during cure of glass-polyester rtm composites: Elastic and viscoelastic modeling," *Journal of Composite Materials,* vol. 39, no. 10, pp. 881-916, 2005.

[154] C. Sun, Z. F. Zhou, W. H. Li, and Q. A. Huang, "A simple method for extracting material parameters of multilayered mems structures using resonance frequency measurements," *Journal of Micromechanics and Microengineering,* vol. 24, no. 7, Jul 2014, Art. no. 075014.

[155] X. G. Guo, Z. F. Zhou, C. Sun, W. H. Li, and Q. A. Huang, "A simple extraction method of young's modulus for multilayer films in mems applications," *Micromachines,* vol. 8, no. 7, Jul 2017, Art. no. 201.

[156] M. Dao, N. Chollacoop, K. J. Van Vliet, T. A. Venkatesh, and S. Suresh, "Computational modeling of the forward and reverse problems in instrumented sharp indentation," *Acta Materialia,* vol. 49, no. 19, pp. 3899-3918, Nov 14 2001.

[157] J. F. Rabolt and B. Fanconi, "Longitudinal acoustic modes of polytetrafluoroethylene copolymers and oligomers," *Polymer,* vol. 18, no. 12, pp. 1258-1264, 1977 1977.

[158] J. F. Rabolt and B. Fanconi, "Longitudinal acoustic mode in helical polymers - poly(oxymethylene) and isotactic polypropylene," *Journal of Polymer Science Part C-Polymer Letters,* vol. 15, no. 3, pp. 121-127, 1977 1977.

[159] M. R. Anderson, M. B. M. Harryman, D. K. Steinman, J. W. White, and R. Currat, "Phonon-dispersion curves and elastic properties of polyoxymethylene single-crystals," *Polymer,* vol. 23, no. 4, pp. 569-577, 1982 1982.

[160] T. L. Sun, R. Q. Song, N. Balar, P. Sen, R. J. Kline, and B. T. O'Connor, "Impact of substrate characteristics on stretchable polymer semiconductor behavior," (in English), *Acs Applied Materials & Interfaces,* Article vol. 11, no. 3, pp. 3280-3289, Jan 2019.

[161] Z. Wang, Y. P. Liu, C. T. Liu, J. S. Yang, and L. B. Li, "Understanding structure-mechanics relationship of high density polyethylene based on stress induced lattice distortion," (in English), *Polymer,* Article vol. 160, pp. 170-180, Jan 2019.

[162] R. Castillo-Perez, M. L. Hernandez-Vargas, O. Flores-Cedillo, and B. F. Campillo-Illanes, "Effect on thermo-mechanical properties by in-situ emulsion polymerization of polymer/clay nanocomposites," (in English), *Polymer Composites,* Article vol. 40, no. 1, pp. 263-276, Jan 2019.

[163] D. S. Reig *et al.*, "Well-defined metal-polymer nanocomposites: The interplay of structure, thermoplasmonics, and elastic mechanical properties," (in English), *Physical Review Materials,* Article vol. 2, no. 12, p. 10, Dec 2018, Art. no. 123605.

[164] P. M. Geethu, I. Yadav, E. Mani, V. K. Aswal, and D. K. Satapathy, "Saddle-splay modulus of reverse microemulsions: Experimental determination using small-angle neutron scattering and dielectric relaxation spectroscopy," (in English), *Physical Review E,* Article vol. 98, no. 5, p. 9, Nov 2018, Art. no. 052604.

[165] J. Frueh, A. Ruhm, Q. He, H. Mohwald, R. Krastev, and R. Kohler, "Elastic to plastic deformation in uniaxially stressed polylelectrolyte multilayer films," (in English), *Langmuir,* Article vol. 34, no. 40, pp. 11933-11942, Oct 2018.

[166] A. C. Ferreira *et al.*, "Elastic softness of hybrid lead halide perovskites," (in English), *Physical Review Letters,* Article vol. 121, no. 8, p. 6, Aug 2018, Art. no. 085502.

[167] E. P. S. Tan, S. Y. Ng, and C. T. Lim, "Tensile testing of a single ultrafine polymeric fiber," *Biomaterials,* vol. 26, no. 13, pp. 1453-1456, May 2005.

[168] S.-C. Wong, A. Baji, and S. Leng, "Effect of fiber diameter on tensile properties of electrospun poly(epsilon-caprolactone)," *Polymer,* vol. 49, no. 21, pp. 4713-4722, Oct 6 2008.

[169] Z. Zhang, Y. Yang, and H. Hamada, "The effects of open holes on the fracture behaviors and mechanical properties of glass fiber mat composites," *Science and Engineering of Composite Materials,* vol. 22, no. 5, pp. 555-564, Sep 2015.

[170] D. Maji and S. Das, "Atomic force microscopy and nanoindentation investigation of polydimethylsiloxane elastomeric substrate compliancy for various sputtered

thin film morphologies," *Journal of Biomedical Materials Research Part A,* vol. 106, no. 3, pp. 725-737, Mar 2018.

[171] J. A. Catalan, R. Martinez, Y. R. Lin, and A. B. Kaul, "Electrical characterization and nanoindentation of opto-electro-mechanical percolative composites from 2d layered materials," *Mrs Advances,* vol. 2, no. 60, pp. 3741-3747, 2017.

[172] A. Molazemhosseini, H. Tourani, M. R. Naimi-Jamal, and A. Khavandi, "Nanoindentation and nanoscratching responses of peek based hybrid composites reinforced with short carbon fibers and nano-silica," (in English), *Polymer Testing,* Article vol. 32, no. 3, pp. 525-534, May 2013.

[173] X. D. Li, H. S. Gao, C. J. Murphy, and K. K. Caswell, "Nanoindentation of silver nanowires," *Nano Letters,* vol. 3, no. 11, pp. 1495-1498, Nov 2003.

[174] S. A. S. Asif and J. B. Pethica, "Nanoindentation creep of single-crystal tungsten and gallium arsenide," *Philosophical Magazine a-Physics of Condensed Matter Structure Defects and Mechanical Properties,* vol. 76, no. 6, pp. 1105-1118, Dec 1997.

[175] D. F. Bahr, D. E. Kramer, and W. W. Gerberich, "Non-linear deformation mechanisms during nanoindentation," *Acta Materialia,* vol. 46, no. 10, pp. 3605-3617, Jun 12 1998.

[176] J. C. Hay, A. Bolshakov, and G. M. Pharr, "A critical examination of the fundamental relations used in the analysis of nanoindentation data," *Journal of Materials Research,* vol. 14, no. 6, pp. 2296-2305, Jun 1999.

[177] M. Martin and M. Troyon, "Fundamental relations used in nanoindentation: Critical examination based on experimental measurements," *Journal of Materials Research,* vol. 17, no. 9, pp. 2227-2234, Sep 2002.

[178] E. P. S. Tan and C. T. Lim, "Nanoindentation study of nanofibers," *Applied Physics Letters,* vol. 87, no. 12, Sep 19 2005, Art. no. 123106.

[179] K. K. H. Wong, J. L. Hutter, M. Zinke-Allmang, and W. Wan, "Physical properties of ion beam treated electrospun poly(vinyl alcohol) nanofibers," *European Polymer Journal,* vol. 45, no. 5, pp. 1349-1358, May 2009.

[180] C. R. Carlisle, C. Coulais, and M. Guthold, "The mechanical stress-strain properties of single electrospun collagen type i nanofibers," *Acta Biomaterialia,* vol. 6, no. 8, pp. 2997-3003, Aug 2010.

[181] M. Wang, H. J. Jin, D. L. Kaplan, and G. C. Rutledge, "Mechanical properties of electrospun silk fibers," *Macromolecules,* vol. 37, no. 18, pp. 6856-6864, Sep 7 2004.

[182] M. R. VanLandingham, J. S. Villarrubia, W. F. Guthrie, and G. F. Meyers, "Nanoindentation of polymers: An overview," *Macromolecular Symposia,* vol. 167, pp. 15-43, Mar 2001.

[183] J. J. Mack *et al.*, "Graphite nanoplatelet reinforcement of electrospun polyacrylonitrile nanofibers," *Advanced Materials,* vol. 17, no. 1, pp. 77-+, Jan 18 2005.

[184] F. S. Russell-Pavier, L. Picco, J. C. C. Day, N. R. Shatil, A. Yacoot, and O. D. Payton, "'Hi-fi afm': High-speed contact mode atomic force microscopy with

optical pickups," *Measurement Science and Technology,* vol. 29, no. 10, Oct 2018, Art. no. 105902.

[185] M. Hatami, "Production and morphological characterization of low resistance polyimide/silver nanowire nanocomposites: Potential application in nanoconductive adhesives," *Journal of Materials Science-Materials in Electronics,* vol. 28, no. 4, pp. 3897-3908, Feb 2017.

[186] J. Z. Kou, Y. Zhang, Y. D. Liu, K. Zhang, W. Liu, and J. Y. Zhai, "Nano-force sensor based on a single tellurium microwire," *Semiconductor Science and Technology,* vol. 32, no. 7, Jul 2017, Art. no. 074001.

[187] A. Gestos, P. G. Whitten, G. M. Spinks, and G. G. Wallace, "Tensile testing of individual glassy, rubbery and hydrogel electrospun polymer nanofibres to high strain using the atomic force microscope," *Polymer Testing,* vol. 32, no. 4, pp. 655-664, Jun 2013.

[188] S. Guriyanova, D. S. Golovko, and E. Bonaccurso, "Cantilever contribution to the total electrostatic force measured with the atomic force microscope," *Measurement Science and Technology,* vol. 21, no. 2, p. 025502, 2009/12/22 2009.

[189] J. L. Duvail *et al.*, "Physical properties of conducting polymer nanofibers," *Synthetic Metals,* vol. 135, no. 1-3, pp. 329-330, Apr 4 2003.

[190] L. M. Bellan, J. Kameoka, and H. G. Craighead, "Measurement of the young's moduli of individual polyethylene oxide and glass nanofibres," *Nanotechnology,* vol. 16, no. 8, pp. 1095-1099, Aug 2005.

[191] S. H. Lee, C. Tekmen, and W. M. Sigmund, "Three-point bending of electrospun tio2 nanofibers," *Materials Science and Engineering a-Structural Materials*

Properties Microstructure and Processing, vol. 398, no. 1-2, pp. 77-81, May 25 2005.

[192]   F. Croisier *et al.*, "Mechanical testing of electrospun pcl fibers," *Acta Biomaterialia,* vol. 8, no. 1, pp. 218-224, Jan 2012.

[193]   D. Perrin, M. Alteirac, S. Corn, and M. E. R. Shanahan, "A novel method for the measurement of elastic moduli of fibres," *Composites Part a-Applied Science and Manufacturing,* vol. 38, no. 1, pp. 71-79, 2007 2007.

[194]   S. Cuenot, C. Fretigny, S. Demoustier-Champagne, and B. Nysten, "Measurement of elastic modulus of nanotubes by resonant contact atomic force microscopy," *Journal of Applied Physics,* vol. 93, no. 9, pp. 5650-5655, May 1 2003.

[195]   S. Boussaad and N. J. Tao, "Polymer wire chemical sensor using a microfabricated tuning fork," *Nano Letters,* vol. 3, no. 8, pp. 1173-1176, Aug 2003.

[196]   S. Cuenot, C. Fretigny, S. Demoustier-Champagne, and B. Nysten, "Surface tension effect on the mechanical properties of nanomaterials measured by atomic force microscopy," *Physical Review B,* vol. 69, no. 16, Apr 2004, Art. no. 165410.

[197]   M. M. J. Treacy, T. W. Ebbesen, and J. M. Gibson, "Exceptionally high young's modulus observed for individual carbon nanotubes," *Nature,* vol. 381, no. 6584, pp. 678-680, 1996/06/01 1996.

[198]   H. J. Butt and M. Jaschke, "Calculation of thermal noise in atomic force microscopy," *Nanotechnology,* vol. 6, no. 1, pp. 1-7, 1995/01/01 1995.

[199]   R. D. Wildman, J. M. Huntley, J. P. Hansen, D. J. Parker, and D. A. Allen, "Single-particle motion in three-dimensional vibrofluidized granular beds," (in English), *Physical Review E,* Article vol. 62, no. 3, pp. 3826-3835, Sep 2000.

[200] C. Steffens, A. N. Brezolin, and J. Steffens, "Conducting polymer-based cantilever sensors for detection humidity," (in English), *Scanning,* Article p. 6, 2018, Art. no. 4782685.

[201] N. J. R. Muniraj, "Mems based humidity sensor using si cantilever beam for harsh environmental conditions," (in English), *Microsystem Technologies-Micro-and Nanosystems-Information Storage and Processing Systems,* Article vol. 17, no. 1, pp. 27-29, Jan 2011.

[202] S. Chatzandroulis, A. Tserepi, D. Goustouridis, P. Normand, and D. Tsoukalas, "Fabrication of single crystal si cantilevers using a dry release process and application in a capacitive-type humidity sensor," (in English), *Microelectronic Engineering,* Article; Proceedings Paper vol. 61-2, pp. 955-961, Jul 2002, Art. no. Pii s0167-9317(02)00448-3.

[203] M. Toda, N. Inomata, T. Ono, and I. Voiculescu, "Cantilever beam temperature sensors for biological applications," (in English), *Ieej Transactions on Electrical and Electronic Engineering,* Review vol. 12, no. 2, pp. 153-160, Mar 2017.

[204] P. G. Datskos, S. Rajic, and I. Datskou, "Photoinduced and thermal stress in silicon microcantilevers," (in English), *Applied Physics Letters,* Article vol. 73, no. 16, pp. 2319-2321, Oct 1998.

[205] M. Godin *et al.*, "Cantilever-based sensing: The origin of surface stress and optimization strategies," *Nanotechnology,* vol. 21, no. 7, Feb 19 2010, Art. no. 075501.

[206] H. Ibach, "Adsorbate-induced surface stress," *Journal of Vacuum Science & Technology a-Vacuum Surfaces and Films,* vol. 12, no. 4, pp. 2240-2243, Jul-Aug 1994.

[207] W. Haiss, "Surface stress of clean and adsorbate-covered solids," *Reports on Progress in Physics,* vol. 64, no. 5, pp. 591-648, May 2001.

[208] A. Boisen and T. Thundat, "Design & fabrication of cantilever array biosensors," *Materials Today,* vol. 12, no. 9, pp. 32-38, Sep 2009.

[209] S. Schmid, S. Dohn, and A. Boisen, "Real-time particle mass spectrometry based on resonant micro strings," *Sensors,* vol. 10, no. 9, pp. 8092-8100, Sep 2010.

[210] T. Braun *et al.*, "Micromechanical mass sensors for biomolecular detection in a physiological environment," *Physical Review E,* vol. 72, no. 3, Sep 2005, Art. no. 031907.

[211] D. Twerenbold, J. L. Vuilleumier, D. Gerber, A. Tadsen, B. vandenBrandt, and P. M. Gillevet, "Detection of single macromolecules using a cryogenic particle detector coupled to a biopolymer mass spectrometer," *Applied Physics Letters,* vol. 68, no. 24, pp. 3503-3505, Jun 10 1996.

[212] D. Twerenbold, "Biopolymer mass spectrometer with cryogenic particle detectors," *Nuclear Instruments & Methods in Physics Research Section a-Accelerators Spectrometers Detectors and Associated Equipment,* vol. 370, no. 1, pp. 253-255, Feb 11 1996.

[213] G. C. Hilton *et al.*, "Impact energy measurement in time-of-flight mass spectrometry with cryogenic microcalorimeters," *Nature,* vol. 391, no. 6668, pp. 672-675, Feb 12 1998.

[214] R. D. Chen *et al.*, "Trapping, detection, and mass determination of coliphage t4 DNA ions of 10(8) da by electrospray-ionization fourier-transform ion-cyclotron resonance mass-spectrometry," *Analytical Chemistry,* vol. 67, no. 7, pp. 1159-1163, Apr 1 1995.

[215] R. D. Smith, X. Cheng, J. E. Bruce, S. A. Hofstadler, and G. A. Anderson, "Trapping, detection and reaction of very large single molecular-ions by mass-spectrometry," *Nature,* vol. 369, no. 6476, pp. 137-139, May 12 1994.

[216] A. G. Marshall, C. L. Hendrickson, and G. S. Jackson, "Fourier transform ion cyclotron resonance mass spectrometry: A primer," *Mass Spectrometry Reviews,* vol. 17, no. 1, pp. 1-35, Jan-Feb 1998.

[217] J. C. Schultz, C. A. Hack, and W. H. Benner, "Polymerase chain reaction products analyzed by charge detection mass spectrometry," *Rapid Communications in Mass Spectrometry,* vol. 13, no. 1, pp. 15-20, 1999 1999.

[218] M. Gamero-Castano, "Induction charge detector with multiple sensing stages," *Review of Scientific Instruments,* vol. 78, no. 4, Apr 2007, Art. no. 043301.

[219] E. E. Pierson, D. Z. Keifer, A. A. Kukreja, J. C. Y. Wang, A. Zlotnick, and M. F. Jarrold, "Charge detection mass spectrometry identifies preferred non-icosahedral polymorphs in the self-assembly of woodchuck hepatitis virus capsids," *Journal of Molecular Biology,* vol. 428, no. 2, pp. 292-300, Jan 29 2016.

[220] S. Schlemmer, J. Illemann, S. Wellert, and D. Gerlich, "Nondestructive high-resolution and absolute mass determination of single charged particles in a three-dimensional quadrupole trap," *Journal of Applied Physics,* vol. 90, no. 10, pp. 5410-5418, Nov 15 2001.

[221] W. P. Peng, Y. T. Lee, J. W. Ting, and H. C. Chang, "Averaging peak-to-peak voltage detector for absolute mass determination of single particles with quadrupole ion traps," *Review of Scientific Instruments,* vol. 76, no. 2, Feb 2005, Art. no. 023108.

[222] R. Kyselica, E. T. Enikov, and Asme, *Dynamic focusing of electrospinning process with quadrupole traps* (Proceedings of the asme international mechanical engineering congress and exposition, 2016, vol. 4a). 2017.

[223] K. L. Ekinci, Y. T. Yang, and M. L. Roukes, "Ultimate limits to inertial mass sensing based upon nanoelectromechanical systems," *Journal of Applied Physics,* vol. 95, no. 5, pp. 2682-2689, Mar 1 2004.

[224] K. Jensen, K. Kim, and A. Zettl, "An atomic-resolution nanomechanical mass sensor," *Nature Nanotechnology,* vol. 3, no. 9, pp. 533-537, Sep 2008.

[225] C. Jiang, B. Chen, J.-J. Li, and K.-D. Zhu, "Mass spectrometry based on a coupled cooper-pair box and nanomechanical resonator system," *Nanoscale Research Letters,* vol. 6, Oct 31 2011, Art. no. 570.

[226] H. Zhang *et al.*, "Femtogram scale nanomechanical resonators embedded in a double-slot photonic crystal nanobeam cavity," *Applied Physics Letters,* vol. 108, no. 5, Feb 2016, Art. no. 051106.

[227] C. Jiang, Y. S. Cui, and K. D. Zhu, "Ultrasensitive nanomechanical mass sensor using hybrid opto-electromechanical systems," *Optics Express,* vol. 22, no. 11, pp. 13773-13783, Jun 2014.

[228] D. Z. Keifer and M. F. Jarrold, "Single-molecule mass spectrometry," *Mass Spectrometry Reviews,* vol. 36, no. 6, pp. 715-733, Nov-Dec 2017.

[229] J. Chaste, A. Eichler, J. Moser, G. Ceballos, R. Rurali, and A. Bachtold, "A nanomechanical mass sensor with yoctogram resolution," *Nature Nanotechnology,* vol. 7, no. 5, pp. 300-303, May 2012.

[230] D. H. Reneker and I. Chun, "Nanometre diameter fibres of polymer, produced by electrospinning," *Nanotechnology,* vol. 7, no. 3, pp. 216-223, Sep 1996.

[231] J. A. Matthews, G. E. Wnek, D. G. Simpson, and G. L. Bowlin, "Electrospinning of collagen nanofibers," *Biomacromolecules,* vol. 3, no. 2, pp. 232-238, Mar-Apr 2002.

[232] N. Bhardwaj and S. C. Kundu, "Electrospinning: A fascinating fiber fabrication technique," *Biotechnology Advances,* vol. 28, no. 3, pp. 325-347, May-Jun 2010.

[233] G. Reiter and R. Khanna, "Kinetics of autophobic dewetting of polymer films," *Langmuir,* vol. 16, no. 15, pp. 6351-6357, Jul 25 2000.

[234] J. Verdu, "Polymeric materials: From molecule to processing," *Revue De Metallurgie-Cahiers D Informations Techniques,* vol. 96, no. 12, pp. 1467-1475, Dec 1999.

[235] D. H. Reneker and A. L. Yarin, "Electrospinning jets and polymer nanofibers," *Polymer,* vol. 49, no. 10, pp. 2387-2425, May 13 2008.

[236] D. H. Reneker, A. L. Yarin, E. Zussman, and H. Xu, "Electrospinning of nanofibers from polymer solutions and melts," in *Advances in applied mechanics, vol 41*, vol. 41, H. Aref and E. VanDerGiessen, Eds. (Advances in applied mechanics, 2007, pp. 43-195.

[237] A. L. Yarin, S. Koombhongse, and D. H. Reneker, "Bending instability in electrospinning of nanofibers," *Journal of Applied Physics,* vol. 89, no. 5, pp. 3018-3026, Mar 1 2001.

[238] T. K. Das, P. Ghosh, and N. C. Das, "Preparation, development, outcomes, and application versatility of carbon fiber-based polymer composites: A review," *Advanced Composites and Hybrid Materials,* vol. 2, no. 2, pp. 214-233, 2019/06/01 2019.

[239] A. M. Ardekani, V. Sharma, and G. H. McKinley, "Dynamics of bead formation, filament thinning and breakup in weakly viscoelastic jets," *Journal of Fluid Mechanics,* vol. 665, pp. 46-56, Dec 2010.

[240] C. Clasen, J. Eggers, M. A. Fontelos, J. Li, and G. H. McKinley, "The beads-on-string structure of viscoelastic threads," *Journal of Fluid Mechanics,* vol. 556, pp. 283-308, Jun 10 2006.

[241] C. Wagner, Y. Amarouchene, D. Bonn, and J. Eggers, "Droplet detachment and satellite bead formation in viscoelastic fluids," *Physical Review Letters,* vol. 95, no. 16, Oct 14 2005, Art. no. 164504.

[242] J. Li and M. A. Fontelos, "Drop dynamics on the beads-on-string structure for viscoelastic jets: A numerical study," *Physics of Fluids,* vol. 15, no. 4, pp. 922-937, Apr 2003.

[243] A. Y. Malkin, A. Arinstein, and V. G. Kulichikhin, "Polymer extension flows and instabilities," *Progress in Polymer Science,* vol. 39, no. 5, pp. 959-978, May 2014.

[244] A. Y. Malkin and C. J. S. Petrie, "Some conditions for rupture of polymer liquids in extension," *Journal of Rheology,* vol. 41, no. 1, pp. 1-25, Jan-Feb 1997.

[245] M. K. Kurbanaliev, G. V. Vinogradov, and A. Y. Malkin, "Fracture of linear-polymers in liquid-media above the glass-transition temperature," *Vysokomolekulyarnye Soedineniya Seriya A,* vol. 23, no. 9, pp. 2032-2038, 1981 1981.

[246] A. Y. Malkin and G. V. Vinogradov, "Fracture of polymers in the viscous-fluid state under stretching," *Vysokomolekulyarnye Soedineniya Seriya A,* vol. 27, no. 2, pp. 227-237, 1985 1985.

[247] M. Sentmanat, B. N. Wang, and G. H. McKinley, "Measuring the transient extensional rheology of polyethylene melts using the ser universal testing platform," *Journal of Rheology,* vol. 49, no. 3, pp. 585-606, May-Jun 2005.

[248] A. Y. Malkin, A. V. Semakov, and V. G. Kulichikhin, "Entanglement junctions in melts and concentrated solutions of flexible-chain polymers: Macromodeling," *Polymer Science Series A,* vol. 53, no. 12, pp. 1198-1206, Dec 2011.

[249] A. Y. Malkin, A. V. Semakov, and V. G. Kulichikhin, "Modeling macromolecular movement in polymer melts and its relation to nonlinear rheology," *Rheologica Acta,* vol. 50, no. 5-6, pp. 485-489, Jun 2011.

[250] S.-Q. Wang, S. Ravindranath, Y. Wang, and P. Boukany, "New theoretical considerations in polymer rheology: Elastic breakdown of chain entanglement network," *Journal of Chemical Physics,* vol. 127, no. 6, Aug 14 2007, Art. no. 064903.

[251] A. Peterlin, "Crystallization from a strained melt or solution," *Polymer Engineering and Science,* vol. 16, no. 3, pp. 126-137, 1976 1976.

[252] M. Stadlbauer, H. Janeschitz-Kriegl, G. Eder, and E. Ratajski, "New extensional rheometer for creep flow at high tensile stress. Part ii. Flow induced nucleation for the crystallization of ipp," *Journal of Rheology,* vol. 48, no. 3, pp. 631-639, May-Jun 2004.

[253] E. E. B. White, H. H. Winter, and J. P. Rothstein, "Extensional-flow-induced crystallization of isotactic polypropylene," *Rheologica Acta,* vol. 51, no. 4, pp. 303-314, Apr 2012.

[254] M. Derakhshandeh and S. G. Hatzikiriakos, "Flow-induced crystallization of high-density polyethylene: The effects of shear and uniaxial extension," *Rheologica Acta,* vol. 51, no. 4, pp. 315-327, Apr 2012.

[255] J. A. Forrest and K. Dalnoki-Veress, "The glass transition in thin polymer films," *Advances in Colloid and Interface Science,* vol. 94, no. 1-3, pp. 167-196, Nov 15 2001.

[256] J. A. Forrest, K. Dalnoki-Veress, and J. R. Dutcher, "Brillouin light scattering studies of the mechanical properties of thin freely standing polystyrene films," *Physical Review E,* vol. 58, no. 5, pp. 6109-6114, Nov 1998.

[257] J. A. Forrest, K. DalnokiVeress, J. R. Stevens, and J. R. Dutcher, "Effect of free surfaces on the glass transition temperature of thin polymer films," *Physical Review Letters,* vol. 77, no. 10, pp. 2002-2005, Sep 2 1996.

[258] M. S. N. Oliveira and G. H. McKinley, "Iterated stretching and multiple beads-on-a-string phenomena in dilute solutions of highly extensible flexible polymers," *Physics of Fluids,* vol. 17, no. 7, Jul 2005, Art. no. 071704.

[259] C. M. Harris, T. L. Paez, and A. G. Piersol, *Harris' shock and vibration handbook*, 6th ed. (Mcgraw-hill handbooks). New York: McGraw-Hill, 2010.

APPENDIX A
COMPARISONS OF THE FIRST SENSOR TO THE THORLABS QPD
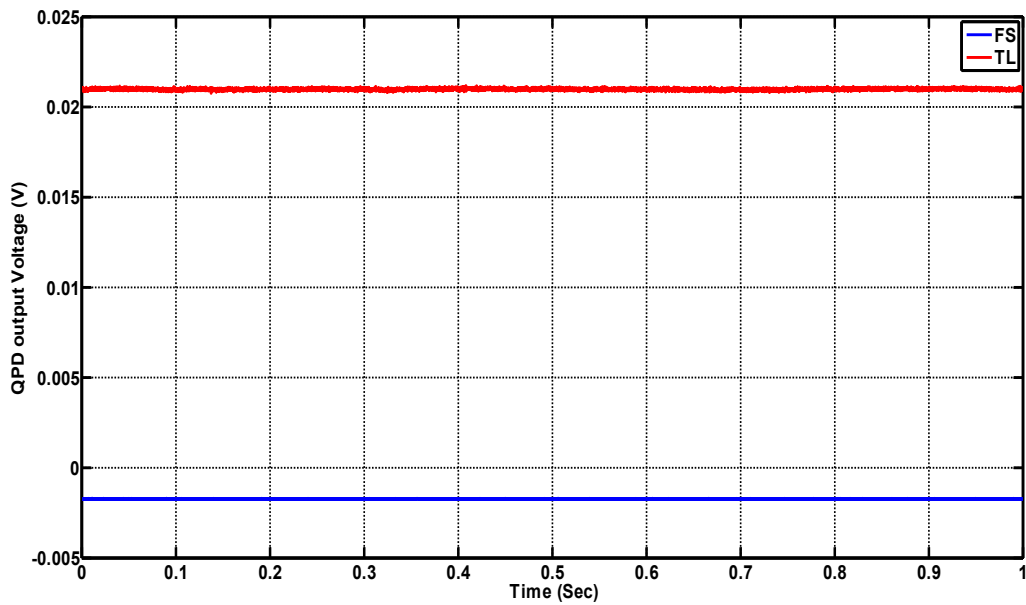
Dark voltage measurements

Figure A1. X$_{diff}$ dark voltage comparison

Dark voltages are recorded with sensor placed in an unlit enclosure. Fig. A1 shows

that the X$_{diff}$ signal for the Thorlabs QPD is 21 mV compared to 2 mV for the First sensor

QPD. Fig. A2 shows the noise that accompanies the dark voltages. The noise is from the

curves of Fig. A1 with the DC level subtracted out. The rms noise levels are 21, 72 µV for

the First, Thorlabs sensor respectively. The spectra of the noise from Fig. A2 as calculated

by FTT is shown in Fig. A3. The noise spectra for the SUM signals are shown
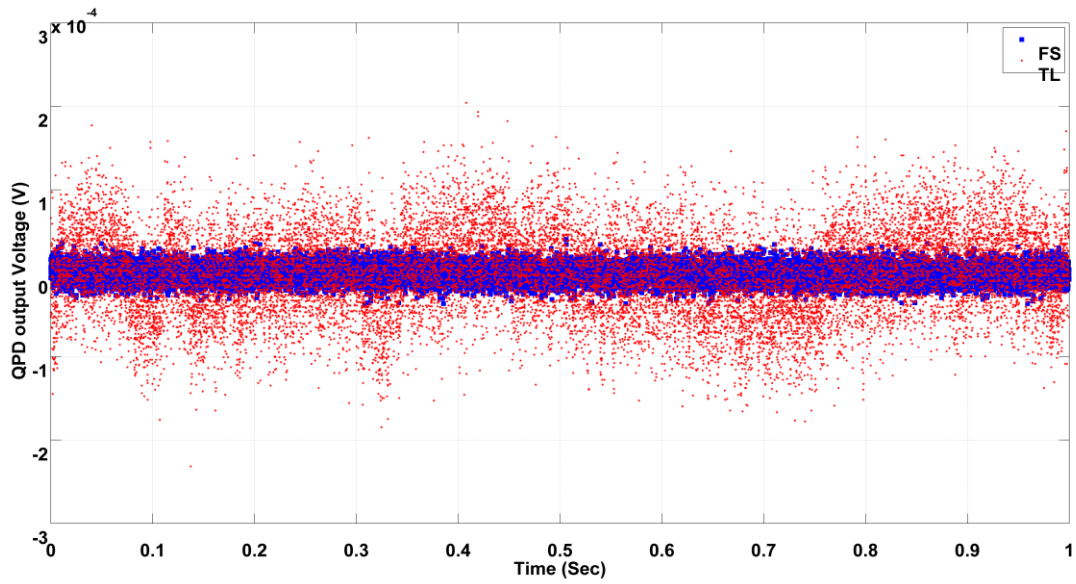
Figure A2. X_{diff} dark signal comparison of noise levels

in Fig. A4. The noise floor for the First sensor QPD is 13.1 dB lower that the Thorlabs QPD.
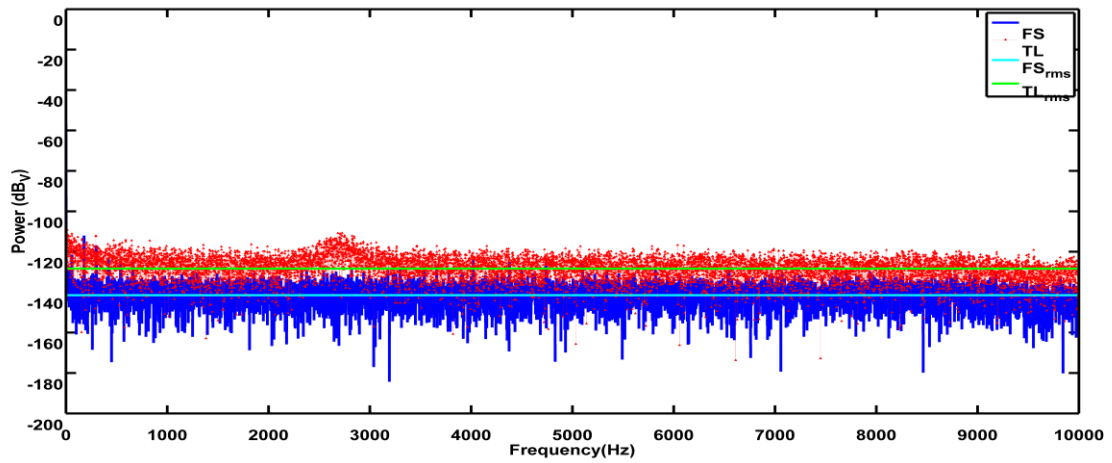
Figure A3. Comparison of the spectral behavior for X_{diff} signals

169

The Thorlabs spectra show a broad peak around 2800 Hz which is not present in the First Sensor spectrum. The SUM signal is only 9.3 dB lower for the First Sensor. The First Sensor also shows numerous large spikes. The spikes are 60 Hz and its harmonics. First Sensor's lower overall noise of X_{diff} than SUM and the missing 60 Hz signal in X_{diff} indicates that the First Sensor QPD has good common mode rejection.

Voltage measurements when the QPDs are illuminated
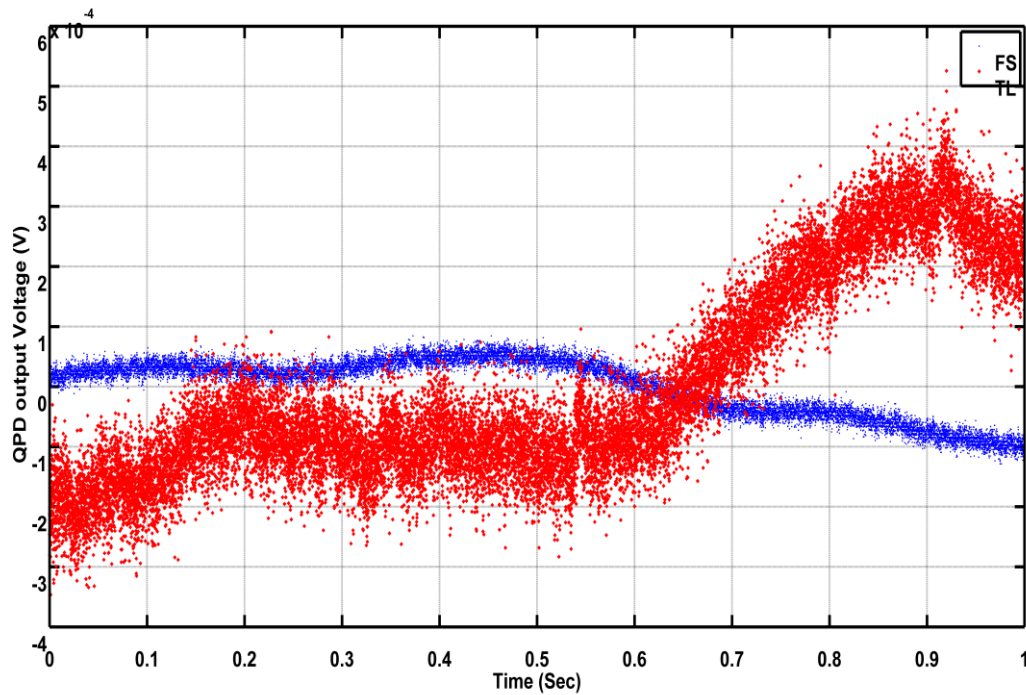
Figure A4. X_{diff} voltages with laser on

The QPDs are illuminated with the laser regulated at 3.6 mW output, 847.6 nm and 25.7° C. Each QPD is illuminated with the same optical power. The next two figures show the raw SUM and X_{diff} voltages produced by
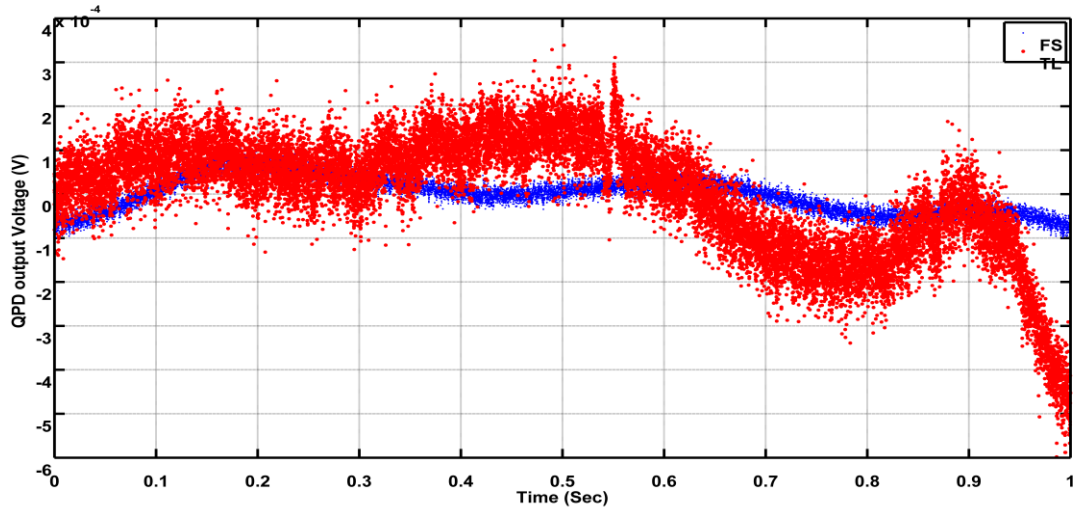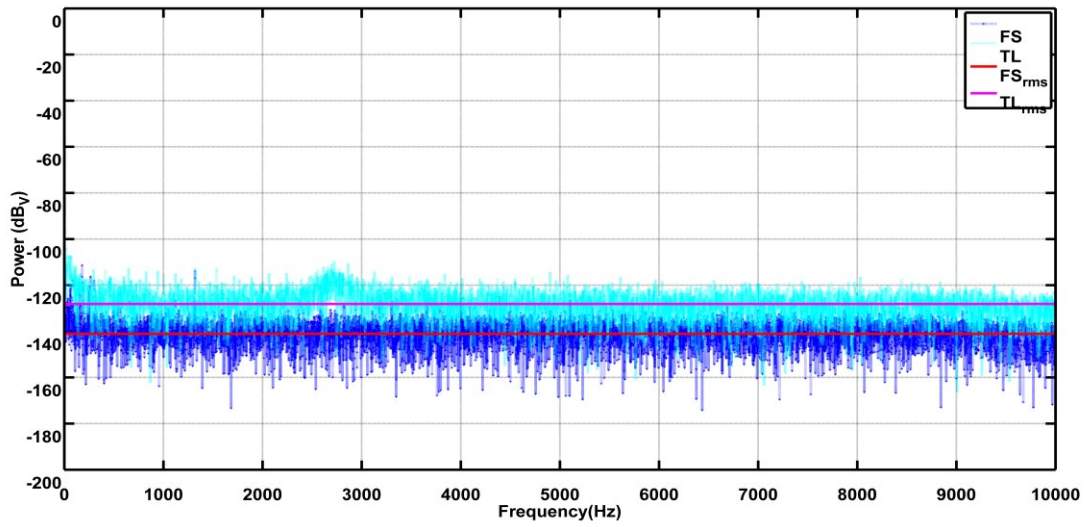
Figure A5. SUM voltages with laser on

Figure A6. Comparison of the spectral behavior for SUM signals (with laser on)

the QPDs while the laser beam illuminates the active sensor areas.   The Thorlabs QPD
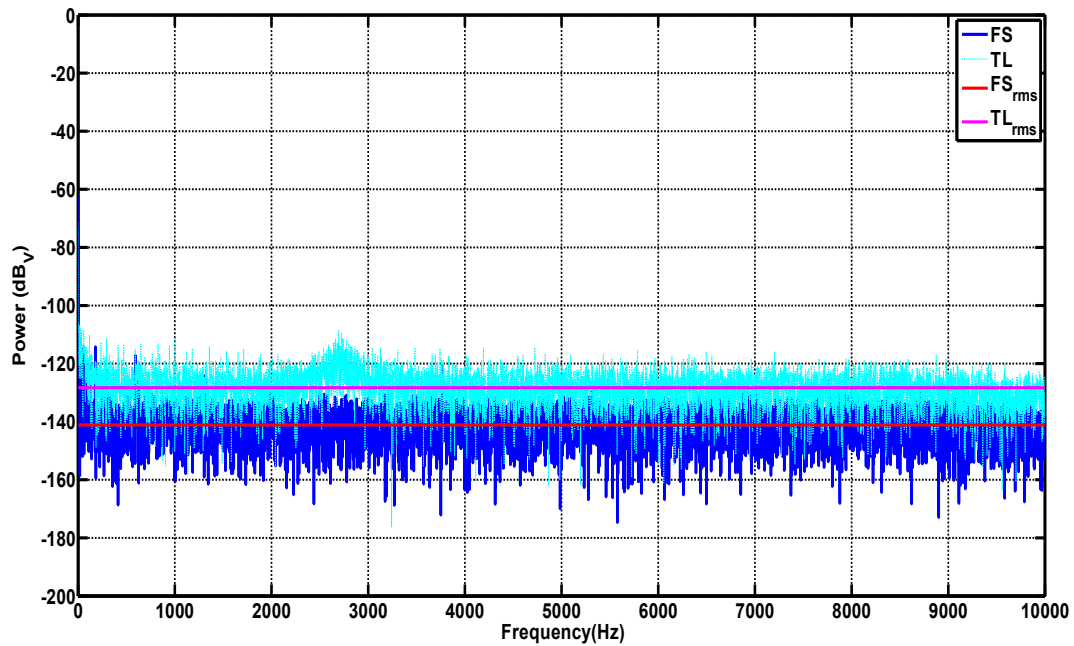
signal drifts more than the First sensor QPD.

Figure A7. Comparison of the spectral behavior for Y_{diff} signals (with laser on)

The above two Figs. A6-A7 show the white noise level of the First Sensor QPD is lower than the Thorlabs detector by about the same amount (12.95 dB) as when there is no illumination. These difference in noise levels for X_{diff}, Y_{diff}, and SUM signals are all about 13 dB lower for the First Sensor QPD.

QPD responses when a glass microfiber is translated across the beam

The following figure is the comparison between Y_{diff} signal produced by two sensors while a 30 μm diameter optical fiber is translated across the laser beam along Y-axis. The peak-peak amplitude of Y_{diff} for the First Sensor QPD is 150.21 mV compared to 130.77 mV for the Thorlabs QPD.

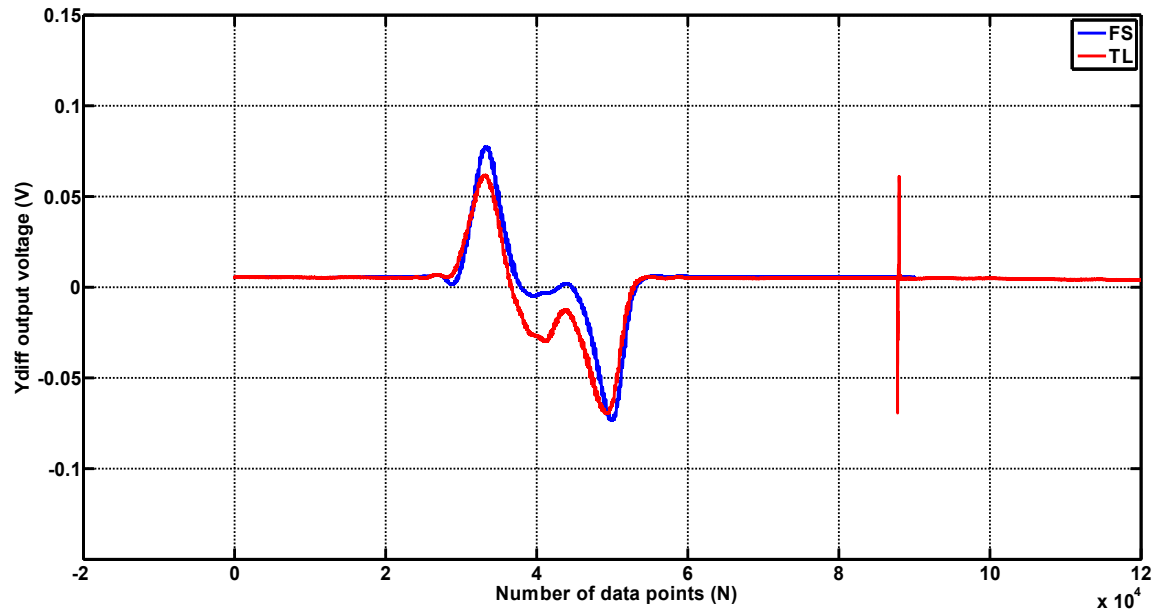Figure A8. Translation data comparison (Y$_{diff}$ signal)

Note these curves are different than the one shown in chapter 4 (Fig. 4.10) because the

laser spot was probably not perfectly aligned while conducting this measurement.

APPENDIX B
PARAMETER CALCULATION & SPECTRAL FITTING

Parameter Calculation

The amplitude, resonance frequency and stiffness of the fiber cantilevers reported in chapter 5 are modeled using the following equations

$$f_0 = \frac{3.52}{2\pi L^2}\sqrt{\frac{EI}{\rho}} \qquad\qquad (2.9\ Modified)$$

$$k = \frac{3EI}{L^3} \qquad\qquad (B1)$$

$$\bar{x} = \sqrt{\frac{k_b T}{k}} \qquad\qquad (2.71)$$

The values for elastic modulus E=71 GPa and the density ρ=2650 Kg/m^3 are taken from the specification sheet provided by the manufacturer.

The model is compared with estimates of the same parameters from the measured spectra of thermal vibration. The Q is calculated using the following equation

$$Q = \frac{f_c}{\Delta f} = \frac{f_c}{|f_1 - f_2|} \qquad\qquad (2.10a)$$

Fig. B1. shows how Q is determined in practice when the vibration spectrum is close to the noise floor. The red solid line is the average of the spectra (moving average filter with 500 data points that corresponds to 50 Hz). The peak of the resonance is at 224.4 Hz and f_1 *and*

f_2 are at 221.53 Hz and 227.27 Hz respectively. This half-power bandwidth of (f_2-f_1) gives the Q of 39 according to eq. 2.10a.
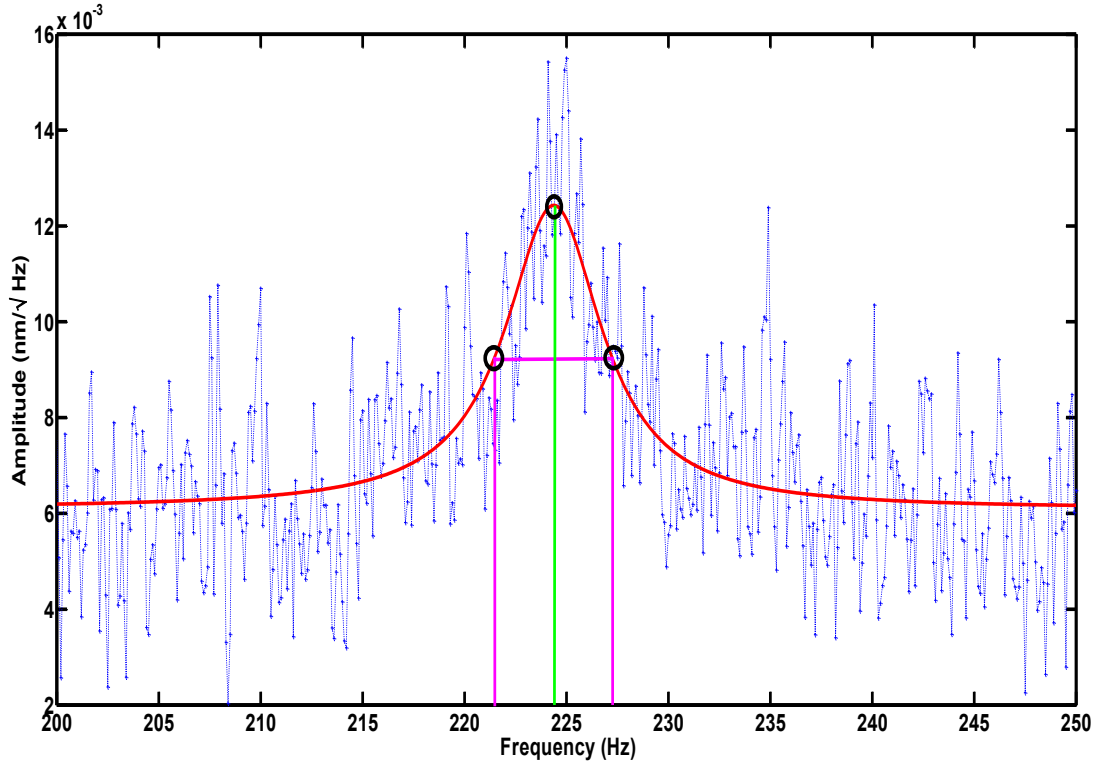

Figure B1. Q estimate from a noisy thermal spectrum of a 20.05 mm x 125 μm cantilevered glass fiber.

Spectral fitting

The vibration spectra measured with the QPD is fit to

$$S_x(f) = \frac{\bar{x}^2/(\pi Q f_0)}{\left(1-\left(\frac{f}{f_0}\right)^2\right)^2 + \left(\frac{f}{Q f_0}\right)^2}$$ (2.8)

Procedure

1. Input the modeled $\bar{x}$ and f_0 into the eq. 2.8 and initiate a fit to the measured spectra using Matlab curve fitting toolbox. Trust-region algorithm of the toolbox is chosen for the fit.

175

2. Matlab establish a fit and return a Q (for example 2.5) with an upper and lower bound (for example 1.5-3.5) value along with a goodness of fit (R-square value, adjusted R-square, SSE and RMSE).

3. An array of values of Q is created with increment of 0.1 between values. The first value of the array is slightly below the lower bound suggested by the Matlab and the last value is slightly above the upper bound.

4. All Q values in the array are fitted to eq. 2.8 and corresponding goodness parameters are recorded.

5. The fit with the lowest adjusted R-square and RMSE for Q is chosen as the best fit. Once the best Q is found, the $\bar{x}$ is varied by ±25 % with 1 % increment to find the best the $\bar{x}$ value.
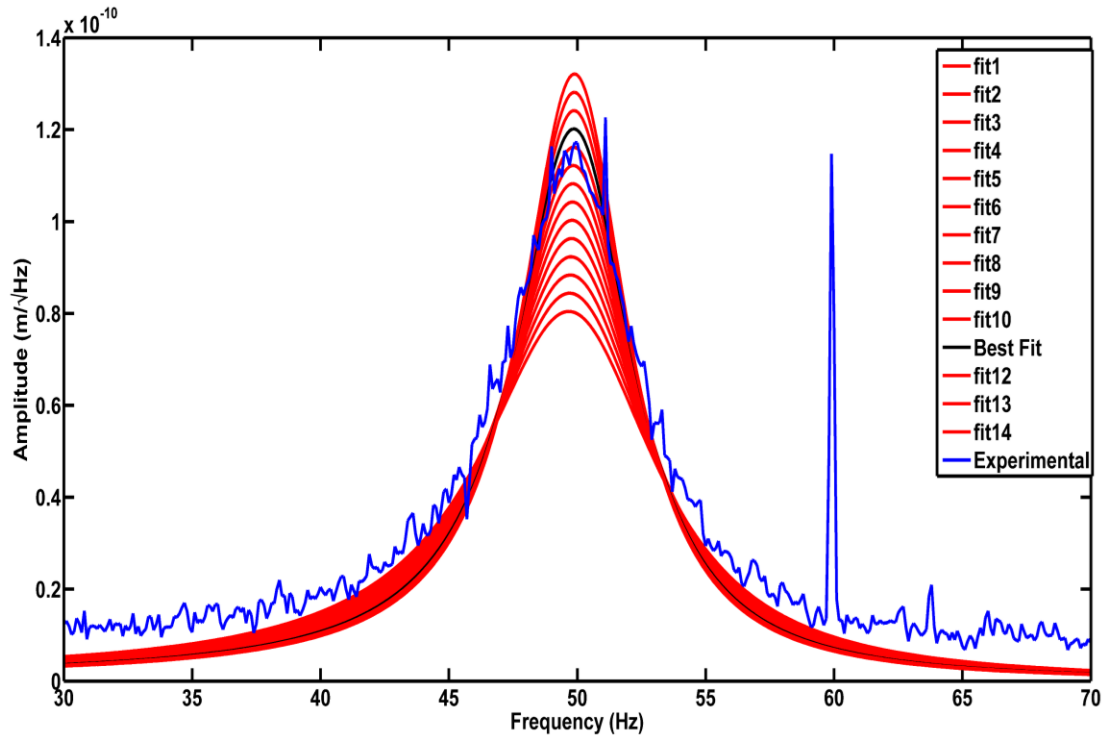
Figure B2. Thermal vibration spectra of a 20.9 mm long glass fiber and its Lorentzian fits to find best fit. Black curve represents the best fit with an RMSE error of 3.45 Å (18%) for $\bar{x}$ (fit value) and 0.3 (3.61%) for Q (fit value) at a resonance frequency of 49.4 Hz (fixed value).

In some cases, a single fit with both adjusted R-square and RMSE is not found. In those cases, adjusted R-square for linear fit and RMSE for Lorentzian fit are chosen as the goodness of fit. It is noted that the peak of the spectrum is lower than the reported value of

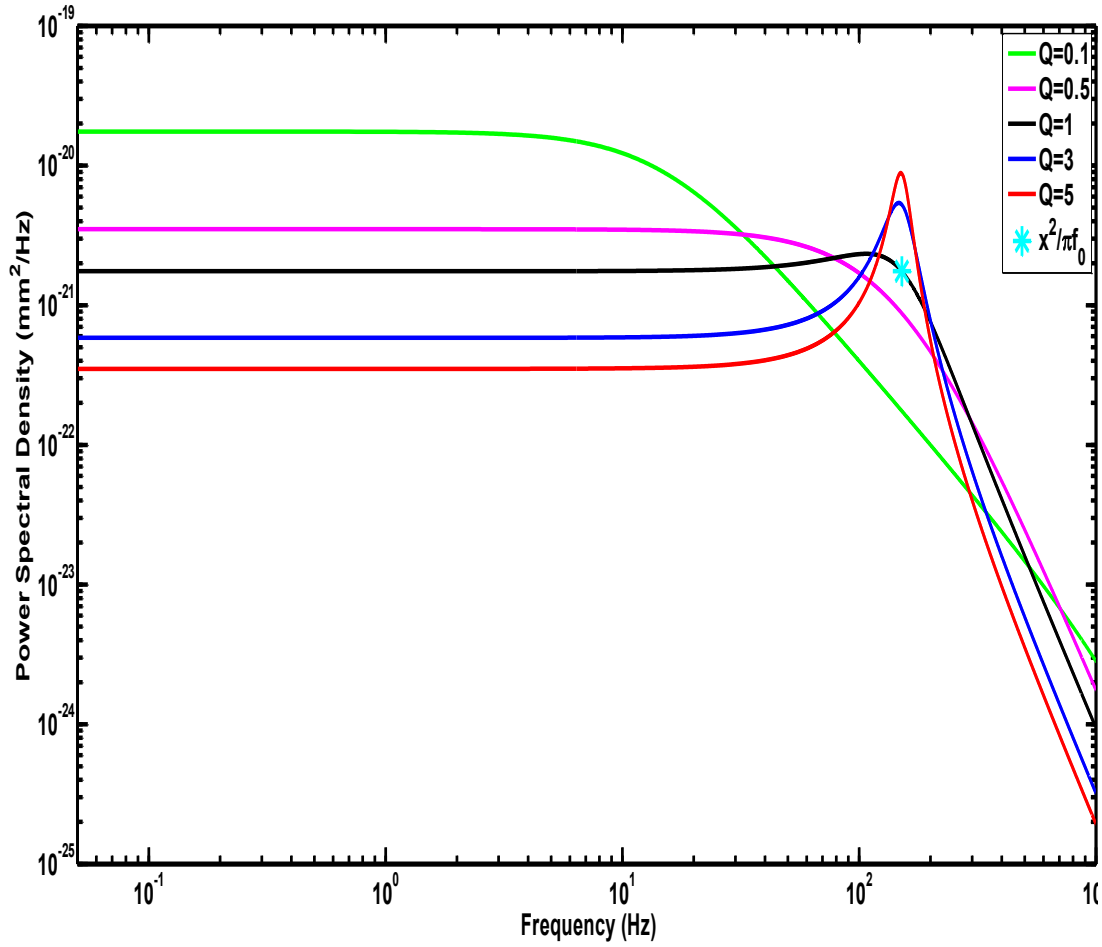$\bar{x} = 19.2$ Å. To clarify the difference between the peak of the Lorentzian and $\bar{x}$

Figure B3. Theoretical Lorentzian spectra (eq. 2.8) with $\bar{x} = 1\ nm$ and Q varies as 5.0>3.0>1.0>0.5>0.1. * represents the constant $\frac{S_x(f_0)}{Q} = \frac{\bar{x}^2}{\pi f_0}$

a theoretical spectrum is shown in Fig. B3.

MODEL OF BOS VIBRATION

Estimates of BOS mechanical properties in Table 3.5 were calculated using the equations

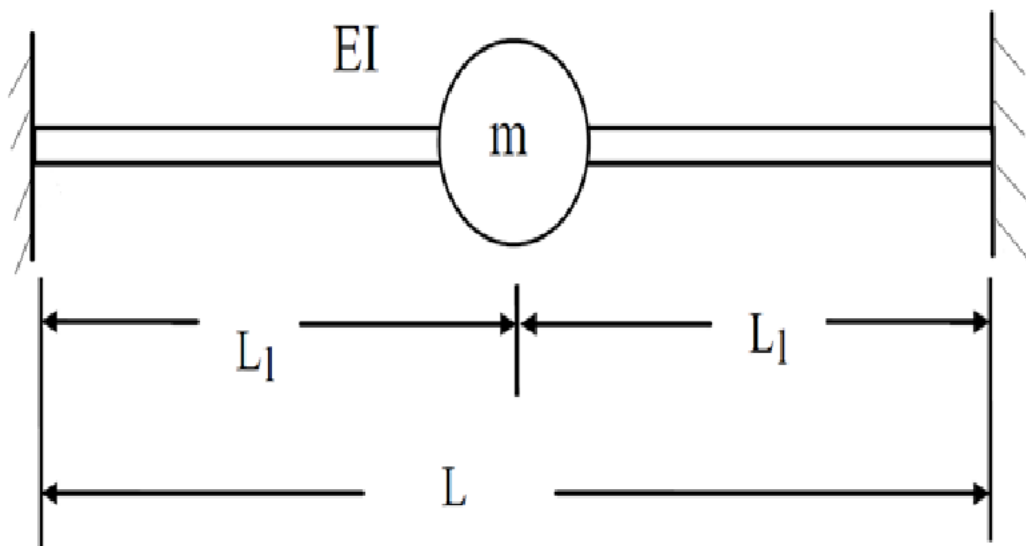presented in Sec. 2.2-2.4 specialized for a structure of the form in Fig. C1.

Figure C1. Bead on a string structure

This is a repeat from earlier in this or another chapter. Reference that. Only call out the

previous equation and how you specialized it for this BOS. L1=L2=L/2 The bead on a

string structures can be modeled as a discrete mass located at the center of string attached

securely on two end supports. In case of this study, the supports are micro pillars. The mass

of the string is negligible compared to the mass of the bead. The stiffness of the string at center (where the bead is attached to the string) is from eq. 6.13 for I for a cylinder gives

$$k = \frac{48EI}{L^3} \qquad (1C)$$

The moment of inertia for a thin rod with a uniform cross section is

$$I = \frac{\pi}{4}r^4$$

$$= \frac{\pi}{64}d^4 \qquad (2C)$$

And the fundamental natural frequency of the BOS can be expressed using eq. 2.9?

$$f_0 = \frac{1}{2\pi}\sqrt{\frac{k}{m}} = \frac{1}{2\pi}\sqrt{\frac{48EI}{mL^3}} = 0.244\sqrt{\frac{E}{L^3}}d^2 \qquad (3C)$$

Due to the nature of the BOS, the vibrational amplitude, frequency, quality factor of the spectra are influenced by a large number of factors. To predict the mechanical characteristics of the BOS, numerical analysis has been conducted using Matlab. The simulation is set up for the following assumptions

1. The bead is spherical in shape.

2. Only a single bead is present along the string exactly at the center of the structure.

3. The cross-sectional area of the string is uniformly cylindrical.

4. There is no gravitational effect on the string.

5. The distance between the micro pillars is 0.8 mm in length.

6. Viscous drag is due to the presence of air only and there is no turbulence. (Sec 2.4.2)

7. Elastic modulus of the polymer fiber is 7.6 GPa
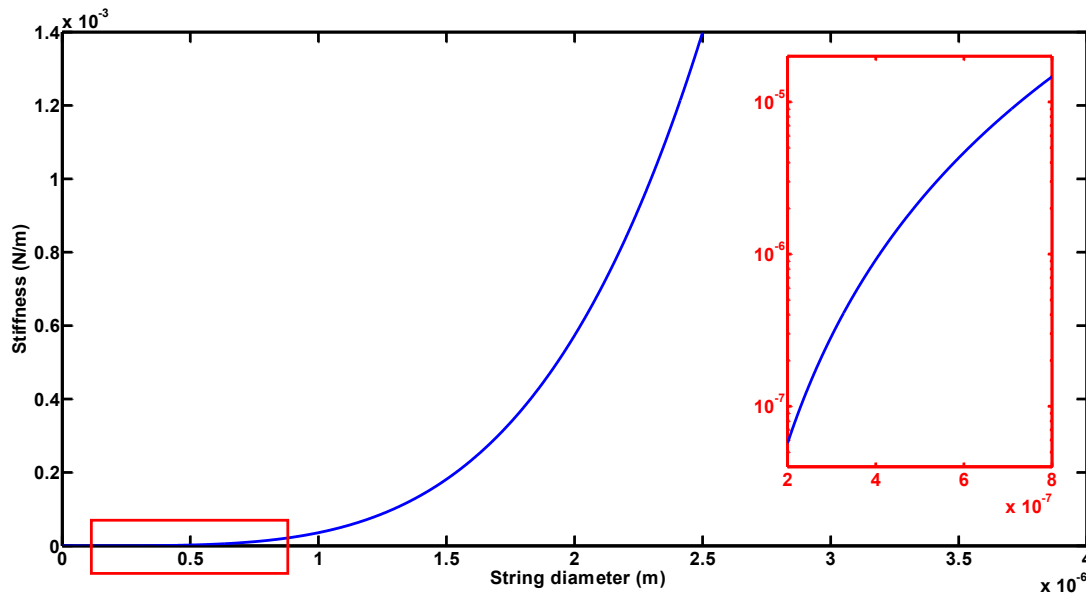
8. Density of the polymer is 1210 Kg/m^3

Figure C2. Dependence of BOS stiffness on string diameter.

Fig. C2 inset shows that stiffness ranges from 0.055 µN/m to 14.33 µN/m for string diameters from 0.2 to 0.8 µm. While the stiffness of the BOS depends only on the diameter of the string, the vibrational frequency depends both on the string diameter and the bead diameter. Fig. C3 shows natural frequency as a function of string and bead diameters. For the string diameters of 0.2 to 0.8 µm, the frequency varies between 12 to 740 Hz. Viscous

damping due to the presence of air at room temperature and pressure corresponds a quality

factor of

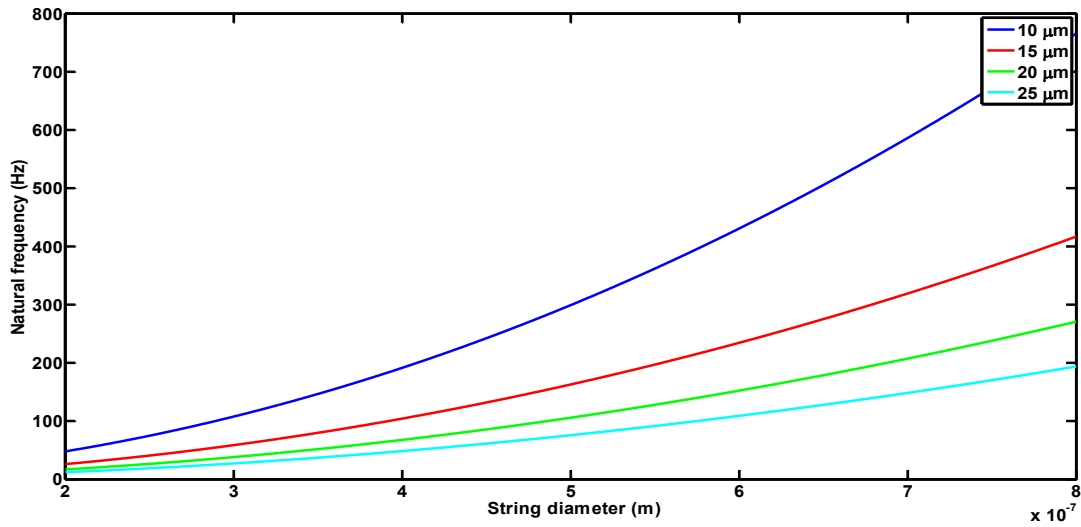$$Q = \frac{2\pi mf}{\gamma} = \frac{2\pi mf}{6\pi r\eta} \qquad\qquad (4D)$$

Figure C3. Change in vibrational frequency with string and bead diameters

Fig. C4 shows that Q varies between 0.1 and 2.7 for stiffnesses ranging from 0.055 to 14.33 µN/m.
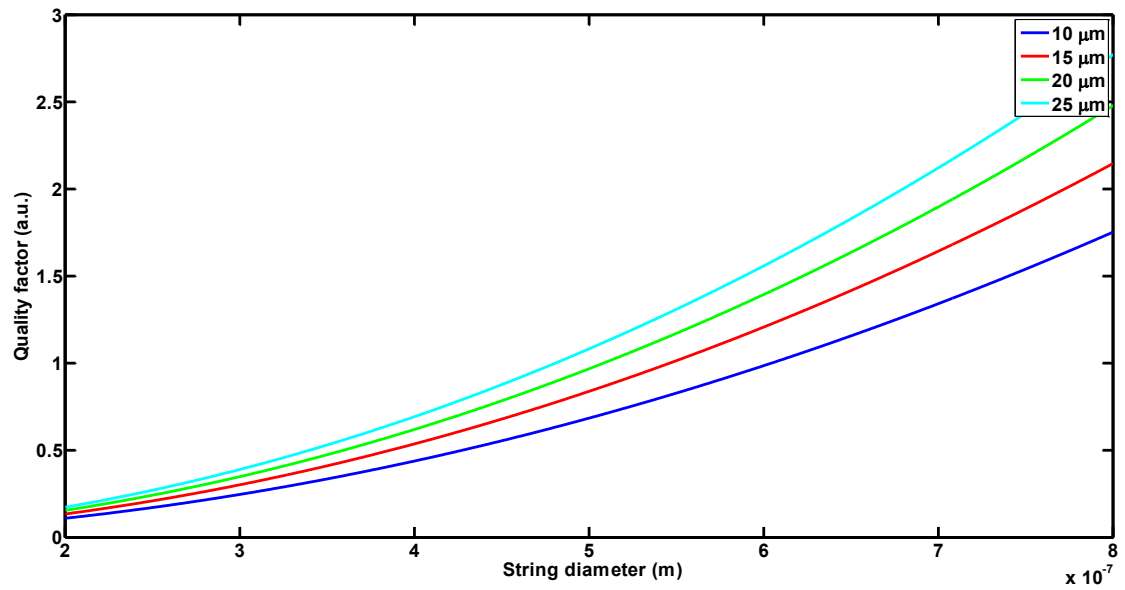

Figure C4. Change in quality factor with bead and string diameters

APPENDIX D
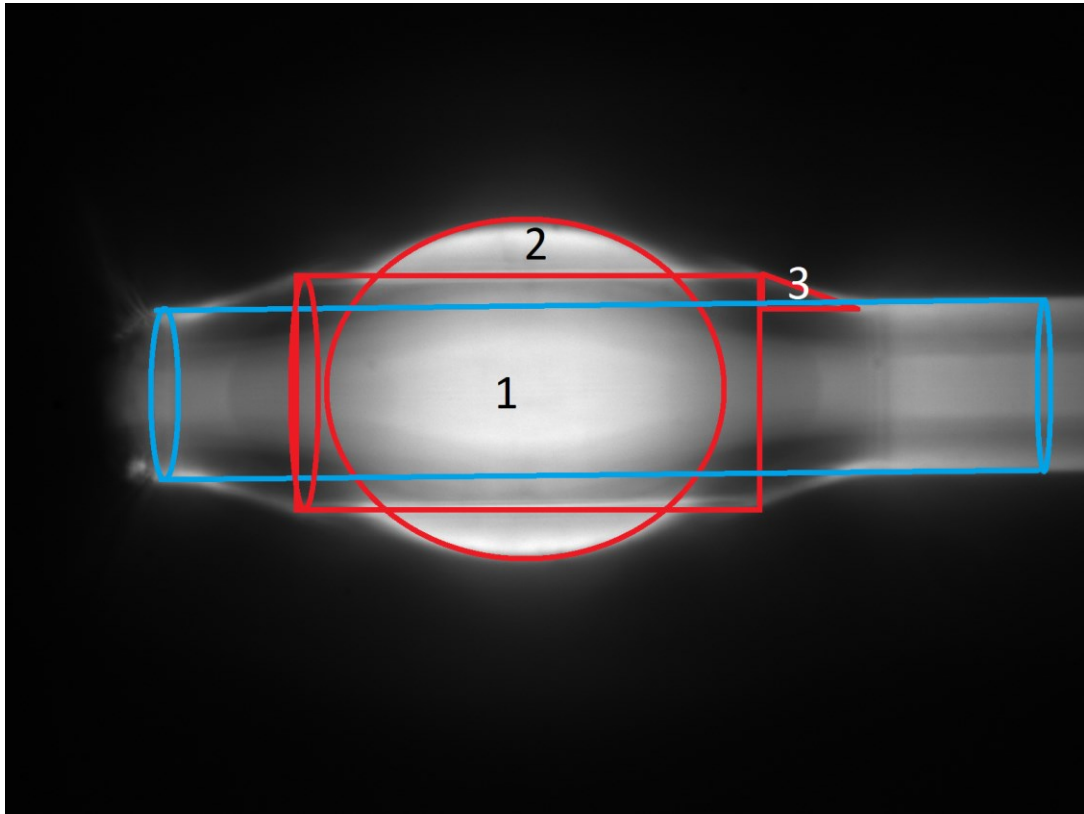## CALCULATION OF MASS OF LIQUID DROPS FROM IMAGE ANALYSIS

Figure D1. Dimension of oil drop on fiber tip

Fig. D1 shows the fiber tip along with the drop formed by using microscope immersion oil. In order to calculate the volume (and mass), the structure is divided into three different shapes, a hollow cylinder (marked by 1), a hollow sphere (marked by 2) and a hollow cone (marked by 3). Calculations of the volume of these shapes are given below.

Volume of the hollow cylinder $v_1 = \pi(r_2^2 - r_1^2)h = 6.1269 \times 10^{-14} m^3$

1.

h=83.64 micron
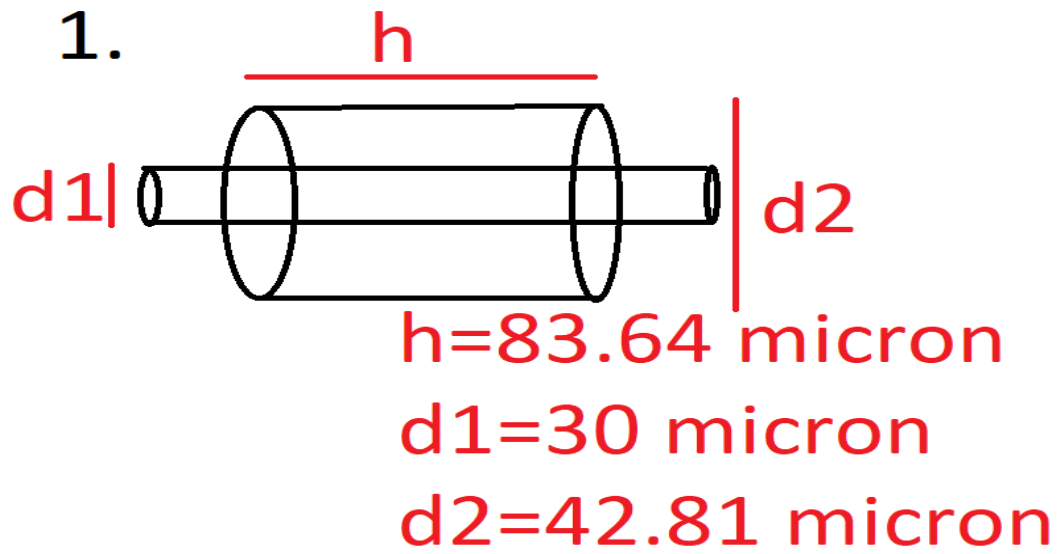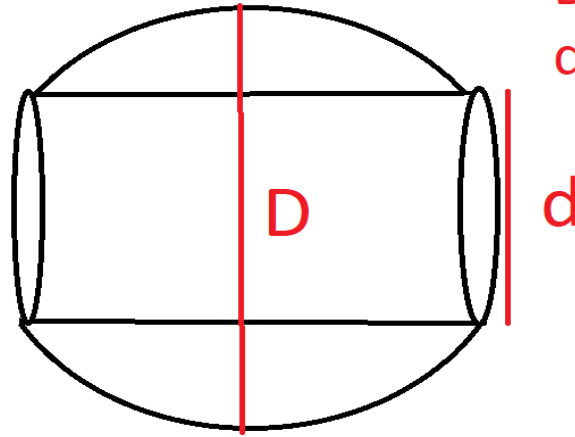d1=30 micron
d2=42.81 micron

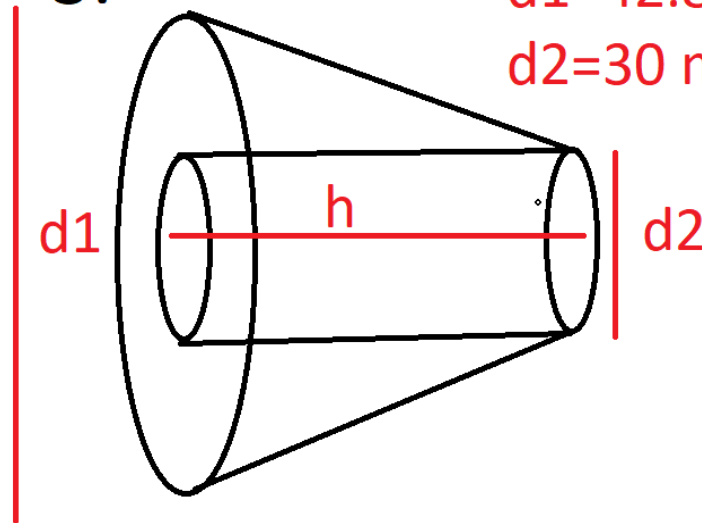Figure D2. Dimension of the cylindrical part of the structure formed by oil drop

2.

D=60.1 micron
d=42.8 micron

Figure D3. Dimension of the spherical part of the structure formed by oil drop

Volume of the hollow sphere $v_2 = \frac{4}{3}\pi(R^2 - r^2)^{3/2}$
$= 3.9299 \times 10^{-14} m^3$

3.

d1=42.8 micron
d2=30 micron

Figure D4. Dimension of the conical part of the structure formed by oil drop

Volume of the hollow conic $v_3 = \left[\frac{1}{3}(r_1^2 + r_1 r_2 + r_2^2)h - \pi r_2^2 h\right] \times 2$

$$= 1.0344 \times 10^{-14} m^3$$

Total volume of the added oil on the fiber is

$$V = v_1 + v_2 + v_3$$

$$= 1.1091 \times 10^{-13} m^3$$

Mass of the oil drop

$$mass\ m = density\ \times volume$$

$$= 920\ Kgm^{-3} \times 1.1091 \times 10^{-13} m^3$$

$$= 1.0204 \times 10^{-10} K$$
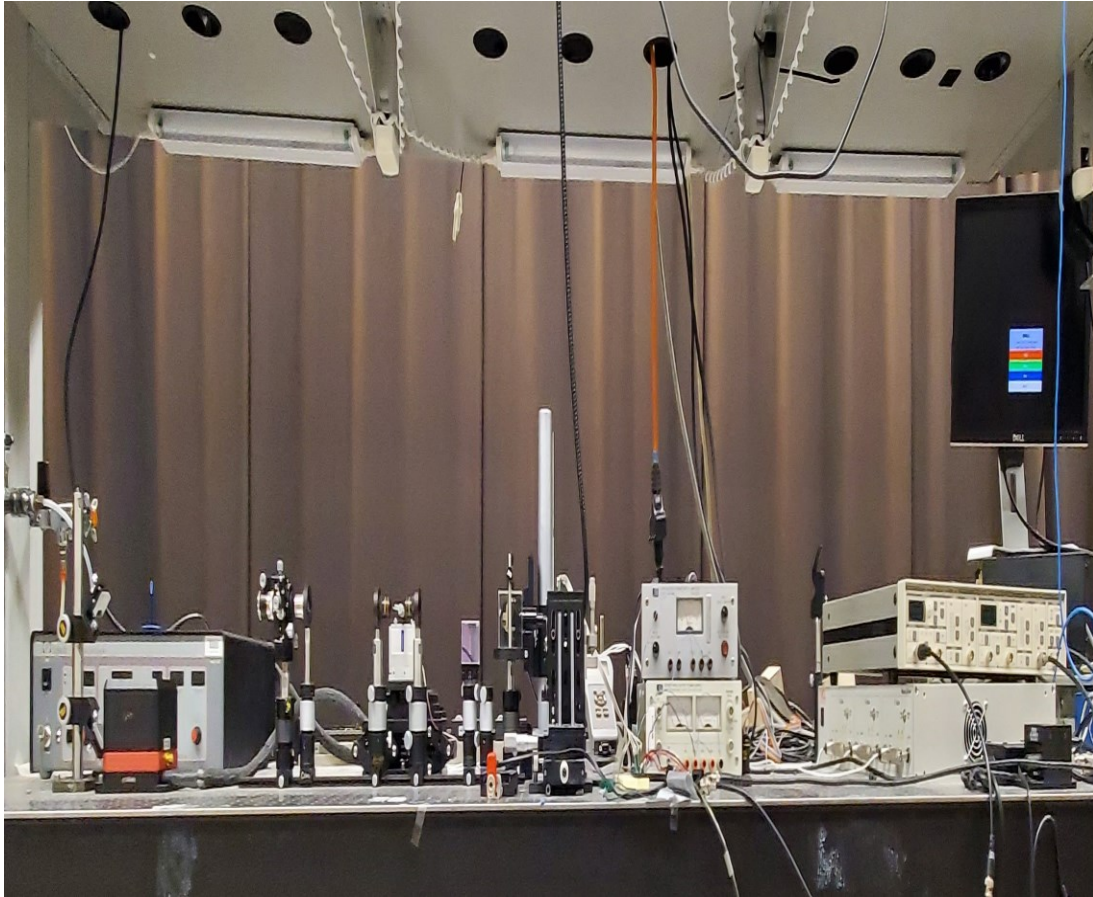
Figure E1. Panoramic view of optical set up

Images of actual experimental set up are shown in this Appendix. Fig. E1 is a panoramic view showing all the components of the set up and Figs. E2-E4 are close ups views of different sections from left-right
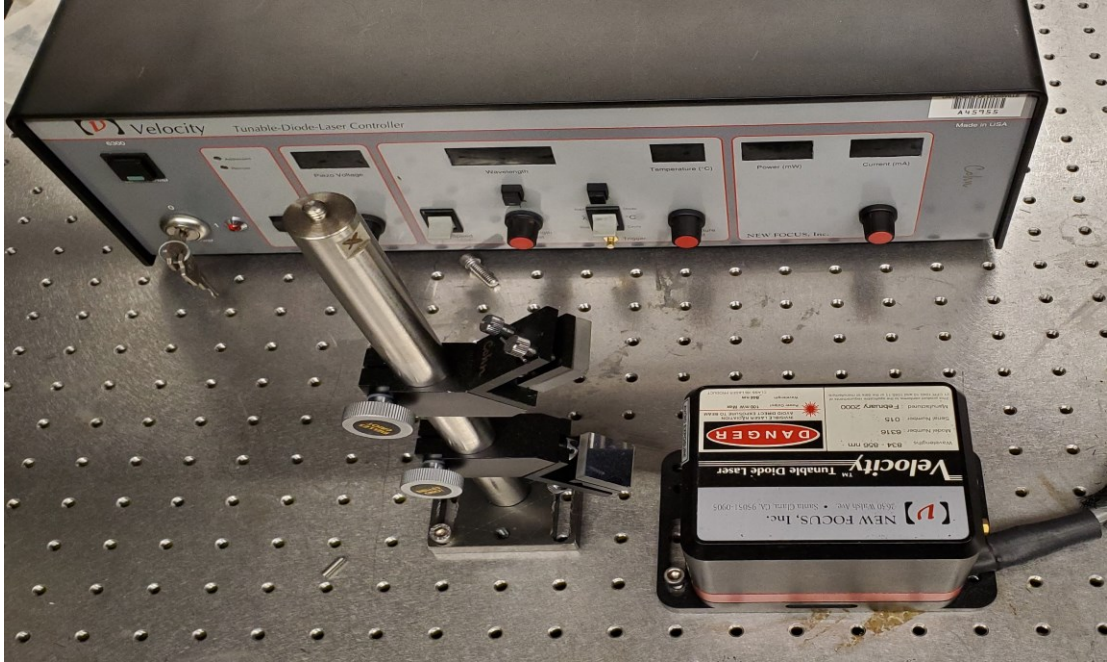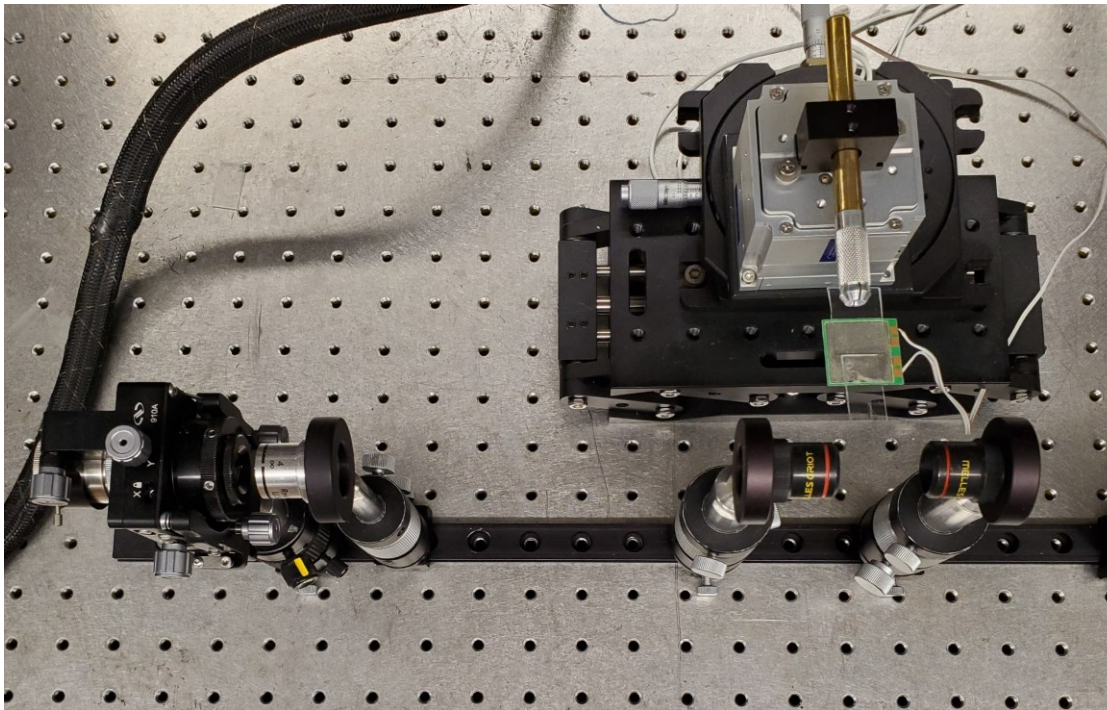
Figure E2. Laser and laser driver

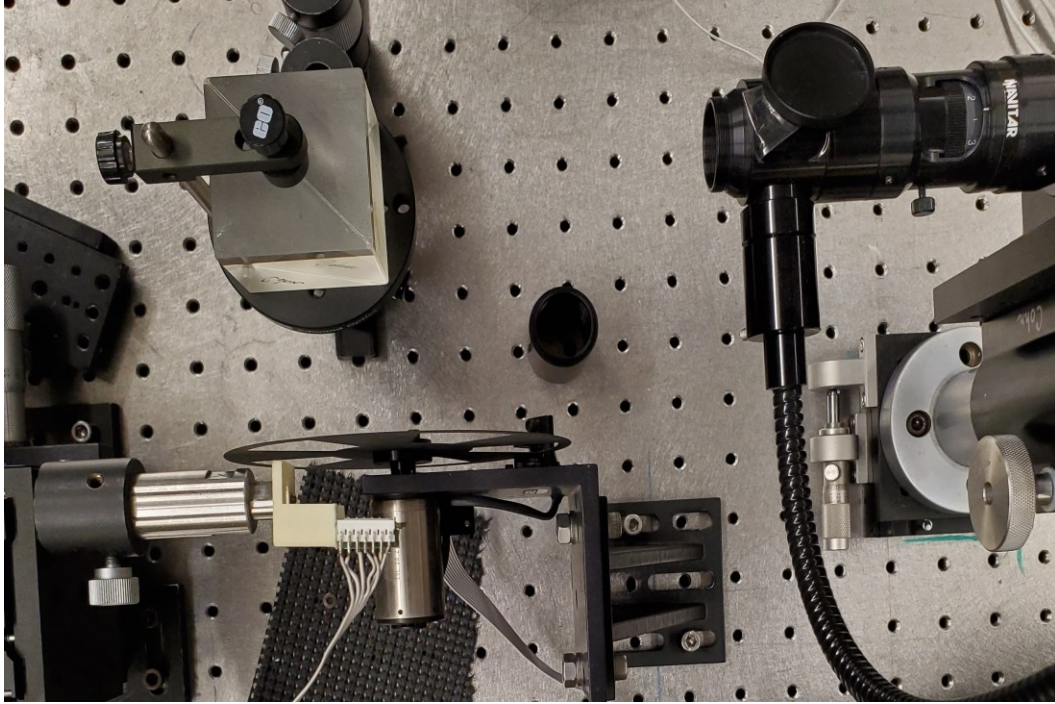Figure E3. Spatial filter, collimating/focusing lenses, sample mount, and nanopositioner

Figure E4. Beam splitter, navigating camera, optical chopper, and QPD

CURRICULUM VITAE

Sri Sukanta Chowdhury

Louisville, KY 40215

Sukanta.chy11104@gmail.com

(502) 759-8141

SUMMARY OF QUALIFICATIONS

6 years of Engineering and multidisciplinary research experience on designing complex optical and electronic instruments. A subject matter expert in optical metrology focusing on precision optics including design, modeling, layout and optimization. Hands on experience in optical system design and development by incorporating a wide range of optics including but not limited to CMOS and CCD camera, LED, laser, photodetector, lenses, prisms, beam splitter, piezo-electric stages etc. Expertise in alignment techniques containing large quantities of optical components. Experienced in Optical signal processing (using MATLAB), Optical simulations (using Zemax), developing algorithms, data acquisition and analysis (using LabVIEW), statistical analysis (Using Minitab), analog circuit design, optical microscopy, IR spectroscopy, AFM and SEM imaging. Ability and desire to learn new skills to adapt to any fast-paced environment.

○ A highly skilled physicist and optical design engineer with experience in collaborating with mechanical engineers, material scientists, neurosurgeons, other physicists and electrical engineers.

○ Demonstrated abilities in problem solving and project management with excellent interpersonal communication skills.

EDUCATION

University of Louisville	**Louisville, KY**
PhD in Electrical Engineering.	August 2019
Dissertation: ***Optical Direct detection of thermal vibrations of***	Advisor: Prof.
ultralow stiffness micro-nano structures	Robert W Cohn
University of Chittagong	**Chittagong,**
MS in Applied Physics and Electronics.	**Bangladesh**
	Dec 2010

University of Chittagong	Chittagong,
BS in Applied Physics and Electronics.	**Bangladesh**
	Jul 2009

EXPERIENCE

University of Louisville	**Louisville, KY**
Graduate Research Assistant	Aug 2012-Current
Projects:	

Direct Optical Detection of Thermally Excited Vibrational Frequency Response of Ultralow Stiffness Micro Structures.	Aug 2013-Jul 2019

- Prototyped, designed, developed and calibrated an optical instrument (vibrometer) with infrared laser, Spatial filter, beam-splitter, CMOS Camera, Quad Photodetector, 3-D Piezo-scanner, Lenses and mirrors. The instrument can detect sub-angstrom scale thermal vibration amplitude without external excitation.
- Measured Brownian motion (vibration) of cantilevered glass fibers and polymer micro-nano structures using the vibrometer.
- Developed algorithm and program using MATLAB to calculate the Modulus of Elasticity of the micro-Structures from the optical vibration measurements.
- Extended the applicability of the designed vibrometer to measure mass change below 1 picogram.

Non-Contact Pulse Oximeter to Measure the Local Blood Oxygen Saturation.	Jan 2016-Mar 2018

- Designed prototype and built a novel Pulse Oximeter that can measure heart rate and blood oxygen saturation with 3% accuracy.
- Ensured the safety and compliance of the device based on applicable regulations.
- Communicated with the part vendors to determine specifications of the right optical parts.
- Characterized and optimized the performance of the device.
- Conducted measurements on human wrist and open spinal cord of injured pigs.

Self-Assembled Arrays of Suspended MEMS Structures from Patterned Polymer Membranes.	Aug 2016-Dec 2018

- Mentored junior researchers and guide them to prepare polystyrene thin film on micropillar array. Measured optical absorption of the film using a spectrometer.
- Patterned holes on the film using a 532 nm pulsed laser and determined the threshold for hole formation. Studied the absorption, ablation, energy barrier for hole nucleation.
- Analyzed the data and established a relation between hole diameter and laser pulse energy.

Optical Intrusion Alarm for Defense of Critical Infrastructure Under Condition of Fog, Smoke or Fire.	Aug 2011-Jun 2013

192

- Created an artificial foggy condition inside a glass chamber with liquid nitrogen and measured the limit of visibility inside the chamber using Laser, Photodetector and Optical power meter.
- Developed LabVIEW program to control movement of a dummy intruder inside the chamber using a stepper motor.
- Developed MATLAB codes to calculate the speed, position and size of the intruder and provided raw data to the software development team to improve the tracking algorithm.

SKILLS

Simulation	Programming	Metrology	MIsc.
○ Matlab	○ C	○ AFM	○ Minitab
○ Zemax	○ LabVIEW	○ SEM	○ Optical alignment
○ PSpice	○ Python	○ Optical Microscope	○ Data Analysis
○ L-Edit		○ Scanning Probe Microscopy	○ Signal Processing
Electronic Equipment	Optics	Design	○ Pressure Sensors
○ Oscilloscope	○ Laser, LED, Camera, detector	○ Analog/Digital Filters	○ Polymers
○ Logic Analyzer	○ Spectrometer, optical modulator	○ Photodiode Diver	○ Biomedical Optics
○ Function Generator	○ Interferometer, photometer, Spatial filters.	○ LED Driver	○ Oximetry
○ Parameter Analyzer		○ Noise Generators	○ Statistical Analysis

PUBLICATIONS

1. S Chowdhury et al. "Optical measurement of thermal vibration spectra to determine Young's modulus of glass micro fibers," in *2018 13th IEEE International Conference on Nanotechnology*, 2018.
2. A Sherehiy et al. "Shape Transformation Photolithography: Self-assembled arrays of suspended MEMS structures from patterned polymer membranes" *ACS Omega, 2018, 3(12), pp 18489-18498.*
3. S Chowdhury et al. "Direct detection of the vibration spectra of micro-nano structures excited by thermal noise" IEEE Transactions on Nanotechnology. *In revision.*
4. S Chowdhury et al. "Design and performance analysis of an optical vibrometer" *under preparation.*
5. S Chowdhury et al. "Tunneling dominated ultrasensitive Strain Sensor based on carbon paint (CP)-PDMS" under preparation.